Modeling Heat and Mass Transfer in Bubbly Cavitating Flows and Shock Waves in Cavitating Nozzles

Thesis by

Alastair T. Preston

In Partial Fulfillment of the Requirements

for the Degree of

Doctor of Philosophy

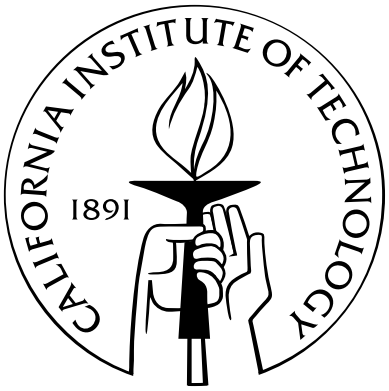

California Institute of Technology

Pasadena, California

2004

(Defended October 27, 2003)

Acknowledgements

During my eight or so years at Caltech there have been numerous people to whom I am indebted. Foremost, my advisor, Professor Tim Colonius, for his outstanding supervision, encouragement, and patience. I am privileged to have been able to work with and learn from such a dedicated and accomplished researcher. I am also grateful to my secondary advisor, Professor Christopher Brennen, whose expertise and constructive suggestions were invaluable to my research, and who introduced me to the excitement of canyoneering. Thanks also to the other members of my thesis committee, Professor Allan Acosta and Professor Jim Beck, for their thorough reviews and useful suggestions.

I thank Clancy Rowley and Jeff Eldredge for research ideas and the often thankless task of system administration. Michel Tanguay assumed that role in the later years, and also facilitated numerous helpful research discussions. I appreciate the advice on many technical issues provided by Gustavo Joseph and Patrick Hung, particularly those pertaining to the completion procedures for this thesis.

The Caltech RFC and my roommates of the first few years, James Gleeson and Roger Koumans, all provided much entertainment outside of my academic life. Thanks to the Caltech and Los Angeles squash communities for enabling me to actively pursue and develop one of my passions. I thank Mark Duttweiler, for compelling research discussions and the introduction to back-country skiing in the San Gabriels during the post candidacy *El Nino* of 1998. There have been numerous other skiers over the years to whom I am grateful. They led me to the Sierras and ensured that at least most of the time the powder did not remain untracked for very long.

I would like to thank my family for instilling within me a quest for learning and

inspired me to do my best in any situation. And, most importantly, I thank my wife, Linh, without whose support, love and understanding I doubt whether this thesis would have ever been completed.

Abstract

Two problems are considered in this thesis: the modeling of heat and mass diffusion effects on the dynamics of spherical bubbles, and the computation of unsteady, bubbly cavitating flows in nozzles. The goal of Part I is to develop a reduced-order model that is able to accurately and efficiently capture the effect of heat and mass transfer on the dynamics of bubbles. Detailed computations of forced and oscillating bubbles including heat and mass diffusion show that the assumptions of polytropic behavior, constant vapor pressure, and an effective liquid viscosity do not accurately account for diffusive damping and thus do not accurately capture bubble dynamics. While the full bubble computations are readily performed for single bubbles, they are too expensive to implement into continuum models of complex bubbly flows where the radial diffusion equations would have to be solved at each grid point. Therefore reduced-order models that accurately capture diffusive effects are needed.

We first develop a full bubble computation, where the full set of radial conservation equations are solved in the bubble interior and surrounding liquid. This provides insight as to which equations, or terms in equations, may be able to be neglected while still accurately capturing the bubble dynamics. Motivated by results of the full computations, we use constant heat and mass transfer coefficients to model the transfer at the bubble wall. In the resulting reduced-order model the heat and mass diffusion equations are each replaced by a single ordinary differential equation. The model is therefore efficient enough to implement into continuum computations. Comparisons of the reduced-order model to the full computations over a wide range of parameters indicate agreement that is superior to existing models.

In Part II we investigate the effects of unsteady bubble dynamics on cavitating flow

through a converging-diverging nozzle. A continuum model that couples the Rayleigh-Plesset equation with the continuity and momentum equations is used to formulate unsteady, quasi-one-dimensional partial differential equations. Flow regimes studied include those where steady state solutions exist, and those where steady state solutions diverge at the so-called *flashing* instability. These latter flows consist of unsteady bubbly shock waves traveling downstream in the diverging section of the nozzle. An approximate analytical expression is developed to predict the critical back pressure for choked flow. The results agree with previous barotropic models for those flows where bubble dynamics are not important, but show that in many instances the neglect of bubble dynamics cannot be justified. Finally the computations show reasonable agreement with an experiment that measures the spatial variation of pressure, velocity and void fraction for steady shock free flows, and good agreement with an experiment that measures the throat pressure and shock position for flows with bubbly shocks. In the model, damping of the bubble radial motion is restricted to a simple "effective" viscosity to account for diffusive effects. However, many features of the nozzle flow are shown to be independent of the specific damping mechanism. This is confirmed by the implementation of the more sophisticated diffusive modeling developed in Part I.

Contents

List of Figures

List of Tables

Part I

Reduced-order modeling of heat and mass diffusion

Chapter 1

Introduction

1.1 Motivation

Cavitating bubbly flows occur in a wide variety of applications. In most situations the presence of cavitation has a negative impact, such as in pumps and propellers, where cavitation can cause performance loss and damage to components by erosion. More recently, positive impacts of cavitation are being exploited, such as in lithotripsy, where cloud cavitation is utilized to promote kidney stone comminution. Whether one wishes to prevent or enhance cavitation, an understanding of the basic physics of the phenomena is essential.

Numerical simulations play an important role in the understanding of the physics of cavitation. Present computing power prohibits a full direct numerical simulation, where the positions of individual bubbles are tracked, for all but the simplest flows. To this end, the continuum bubbly flow model for dilute bubbly mixtures (van Wijngaarden 1968, van Wijngaarden 1972), where one computes an average bubble radius at each position and instance in the flow, has been widely used. The continuum model has been applied to idealized flows to obtain semi-analytical solutions for linear bubble oscillations in the study of acoustics, linear stability and linear cloud dynamics (d'Agostino, Brennen & Acosta 1988, d'Agostino & Brennen 1988, d'Agostino & Brennen 1989, d'Agostino, d'Auria & Brennen 1997). More recently, full non-linear computations have been performed for such problems as a spherical cloud of bubbles (Wang & Brennen 1999), bubbles adjacent to an oscillating plane wall (Colonius,

d'Auria & Brennen 2000), a cavitating converging-diverging nozzle (Preston, Colonius & Brennen (2002) and Part II of this thesis), and an ellipsoidal lithotripter (Tanguay 2003).

While these computations represent important advances in our cavitation knowledge, a significant limitation of the continuum model is the use of the traditional Rayleigh-Plesset equation to model the spherical bubble dynamics. In this model it is assumed that the bubble contents behave in a polytropic manner, and the diffusion of vapor within the bubble occurs so quickly as to result in constant vapor pressure. In turn, an effective liquid viscosity is used to account for the otherwise neglected diffusive damping. However, detailed computations of forced and oscillating single bubbles, including heat and mass diffusion, show that this simplistic approach does not accurately capture the bubble dynamics (Prosperetti, Crum & Commander 1988). While the full bubble computations are readily performed for single bubbles, they are generally too computationally intensive to implement into continuum models of bubbly flows, where the radial diffusion equations would have to be solved at each grid point. Although some workers have successfully implemented these radial diffusion equations into the continuum model (Watanabe & Prosperetti 1994, Matsumoto & Kameda 1996, Kameda & Matsumoto 1996, Kameda, Shimaura, Higashino & Matsumoto 1998), this has only been for simple flow geometries and liquids containing small, non-condensible gas bubbles. For more complex flow geometries, and for cavitating gas-vapor bubbles which may grow many times their original size, this approach would result in a huge computation. Therefore reduced-order models that accurately capture diffusive effects are needed to enable realistic and computationally feasible continuum computations.

Although there are some existing reduced-order models, these are generally not able to be easily and efficiently implemented and/or are not accurate enough for the desired applications. The primary focus of Part I of this thesis is to develop and validate an efficient reduced-order model that is able to accurately capture the impact of diffusive processes on bubble dynamics. Specifically, the goals are to obtain a model that is able to estimate bubble growth and rebound radii to within a few percent,

and the less critical minimum radii to within about ten percent. The model should be sufficiently simple and computationally efficient to readily enable implementation into existing and future continuum computations. Presently we do not focus on obtaining accurate estimates of peak bubble pressures, temperatures, and vapor content during collapse, since these quantities do not directly impact the dynamics of bubbly cavitating flows.

1.2 Historical perspective

The need for a better treatment of diffusive effects in the standard Rayleigh-Plesset equation was illustrated by the full thermal computations of Prosperetti et al. (1988). Since then many other full computations, including both thermal and mass diffusion, have been used in a variety of applications. Such full bubble computations are an essential step in the development of reduced-order models, since not only do they motivate possible models through gaining a better understanding of the diffusive processes, but they enable the models to be validated by comparative testing. In this section we provide a summary of previous full bubble computations, as well as existing reduced-order models.

1.2.1 Full bubble computations

The equations describing the dynamics of a spherical gas-vapor bubble are very complex, involving partial differential equations (PDEs) for conservation of mass (both of the bulk flow and individual species), momentum and energy in both the gaseous bubble interior and the liquid exterior. At the bubble wall there are additional equations which link the interior and exterior domains. Although recent advances in computational power and numerical techniques have enabled these equations to be solved in their entirety (Matsumoto & Takemura 1994), earlier workers necessarily made use of various assumptions to reduce the number (and complexity) of PDEs. These simpler sets of equations can be thought of as reduced-order models in their own right, although in most situations the computational effort in their solution is still

considerable. For the purposes of this thesis we shall delineate between full bubble computations and reduced-order models, by defining the latter to be those that only involve a few ordinary differential equations (ODEs) and no PDEs. This is a natural definition in the context of developing reduced-order models for application to continuum models, since it is the solution of the radial PDEs at every grid point in a flow that we wish to avoid. Hence, in what follows we summarize full bubble computations which, by the above definition, involve the numerical solution of at least one PDE.

In perhaps the first full bubble computation, Hickling (1963) used a finite difference method to solve the conservation equations for the interior of a gas bubble that was caused to collapse by a step increase in ambient pressure. The liquid was assumed to be incompressible which enables the continuity and momentum equations in the liquid to be integrated. This results in a Rayleigh-Plesset equation to describe the liquid motion, which is coupled to the full PDEs of the gas interior through the pressure at the bubble wall. Due to computational limitations calculations were not able to be made through a full bubble collapse, but nonetheless important conclusions regarding bubble temperature and its implications on sonoluminescence intensities were able to be made.

The equations for a gas-vapor bubble, including the variation of liquid temperature outside the bubble, were solved by Nigmatulin, Khabeev & Nagiev (1981). In addition to assuming an incompressible liquid, they assumed a spatially uniform pressure within the bubble (homobarotropic), which enabled the interior continuity and momentum equations to be integrated analytically. The only PDEs that remained to be integrated were the mass diffusion of gas and vapor within the bubble, and the thermal energy equations for both the bubble interior and exterior. These were solved using a finite difference method for relatively mild bubble collapses that were caused by a step increase in ambient pressure.

The homobarotropic assumption was also employed independently by Prosperetti et al. (1988) for a gas bubble with constant liquid temperature. A finite difference method was used to solve the remaining interior energy equation for bubbles in harmonically varying pressure fields. Frequency response curves from the full computa-

tion were compared to those from the traditional Rayleigh-Plesset equation, where the gas was assumed to behave polytropically. They demonstrated that the polytropic assumption can give gross errors in bubble response, even if an effective liquid viscosity is used to account for thermal damping. The same set of equations were solved by Kamath & Prosperetti (1989) using collocation and Galerkin spectral methods. These spectral methods were found to be considerably more efficient than the previously used finite difference methods. Hao & Prosperetti (1999*b*) implemented the spectral collocation method in homobarotropic computations that also included the energy equation in the liquid. The dynamics of pure gas vapor bubbles and their growth by rectified heat diffusion was investigated.

Based upon the homobarotropic assumption, Ichihara, Kawashima & Kameda (2000) formulated a more complete set of equations. As well as including energy equations in both the bubble and liquid, the diffusion of vapor in the bubble and of dissolved non-condensible gas in the surrounding liquid were accounted for. A finite difference method was used to solve the resulting system for relatively low amplitude oscillations, with the primary focus being on the coupling of the heat and mass transfer, and the associated impact on the bubble dynamics.

Matsumoto & Takemura (1994) used a finite difference method to solve the complete set of conservation equations for a gas-vapor bubble in a liquid that also contained some dissolved non-condensible gas. This is one of the few computations that assumes the liquid to be fully compressible, and solves the liquid momentum equation in the near field which is matched to the linear analytical solution in the far field. The computations are for relatively mild bubble collapses, so that the effect of this liquid compressibility is likely to be negligible. They demonstrated the importance of the gas Peclet numbers (relating to both heat and mass transfer [see Section 2.5.2]), in determining the type of bubble response. In a companion paper the effects of mist formation within the bubble were studied (Takemura & Matsumoto 1994).

The effect of diffusive transport on shock formation within strongly collapsing pure gas bubbles is investigated in the context of sonoluminescence by Vuong & Szeri (1996). They use the Keller equation, which has a first-order correction for liquid

compressibility, to describe the motion of the liquid. The energy equation in the liquid is simplified to the linear diffusion equation by assuming the thermal penetration length to be far smaller than the bubble radius. This, together with the energy equation in the bubble interior, are solved with a finite difference method. The paper illustrates how diffusive processes prevent steepening of wave fronts and therefore formation of shocks in monatomic gases, which had previously been proposed as a mechanism for sonoluminescence production.

Storey & Szeri (1999) extended the computations of Vuong & Szeri (1996) to include diffusion of two monatomic gases in the bubble interior, using a more efficient spectral collocation method. Results show that significant species segregation occurs during collapse, due to the high temperature gradients within the bubble. The computations were further extended to include mass diffusion and chemical reactions of water vapor (Storey & Szeri 2000). It was demonstrated that the finite rate of mass diffusion resulted in water vapor being trapped in the center of the bubble during strong collapses. This had the effect of reducing the internal bubble temperature, due to the ratio of specific heats for the vapor being lower than for the non-condensible gases. While the species segregation and vapor trapping do not have any effect on bubble dynamics, they do have important implications on the possible mechanisms for sonoluminescence production and intensities.

1.2.2 Reduced-order models

Perhaps the first treatment of thermal effects on bubbles was that of Plesset & Zwick (1952), who obtained approximate solutions of the heat diffusion equation in the liquid surrounding the bubble. The solution for the bubble wall temperature was found in the form of a convolution integral, and is valid in situations where the thermal penetration length in the liquid is far smaller than the bubble radius. Other authors have applied similar techniques for the solution of the mass diffusion equation in the liquid, in order to analyze bubble growth by rectified mass diffusion (Fyrillas & Szeri 1994, Lofstedt, Weninger, Putterman & Barber 1995, Vuong, Fyrillas &

Szeri 1998). The models do not address the important processes in the bubble interior, and the numerical evaluation of the convolution integral becomes very time-consuming for long simulations.

Flynn (1975) developed a series of ODEs to estimate the average bubble temperature, based upon numerous physical and mathematical approximations of the energy equation. The volume averaged perfect gas relation is then used to estimate the bubble internal pressure, which closes the Keller equation for the motion of the liquid. The complicated nature of the series of ODEs, and the lack of justification for many of the approximations, has resulted in the model remaining largely unused. The model was extended by Fujikawa & Akamatsu (1980) to include second-order liquid compressibility effects and non-equilibrium phase change at the interface. However the treatment of the internal energy problem remains to be validated.

Models for heat transfer in the nearly isothermal and nearly adiabatic limits were developed by Prosperetti (1991), who used a perturbation analysis in the limits of low (isothermal) and high (adiabatic) Peclet number. The model in the nearly isothermal limit resulted in a very simple ODE for the bubble internal pressure, that is readily able to be implemented into any continuum computation. However, the model only gives accurate results in the limited regime of very low Peclet numbers. In the nearly adiabatic limit the model results in a convolution integral. As in the related case of the liquid temperature (Plesset & Zwick 1952), the evaluation of the integral becomes computationally prohibitive for long simulations. In addition the model does not conserve the mass of gas within the bubble, which causes the model solution to diverge from the full solution for long computations.

The similar models of Toegel, Gompf, Pecha & Lohse (2000) and Matula, Hilmo, Storey & Szeri (2002) assume a homobarotropic bubble and use estimates of the heat and mass fluxes at the bubble boundary to close the ODE for the internal bubble pressure. The flux estimates are based upon a diffusive penetration length, which is a reasonable approach for large bubbles, but leads to poor results when the penetration length approaches or exceeds the bubble radius. In addition there is an error in the mass transfer model, which results in the incorrect situation of bubble growth being

limited by finite rate mass diffusion, even when the vapor concentration in the bubble approaches unity.

Storey & Szeri (2001) and Storey, Lin & Szeri (2001) propose a transfer model based upon relative timescales. When bubble motions are fast compared to diffusive processes the bubble is assumed to behave adiabatically with no mass transfer, while during slow bubble motions the bubble is assumed to behave isothermally with infinitely fast mass transfer. The model also accounts for non-equilibrium phase change at the bubble wall, and uses a correction for the slightly non-uniform internal pressure (Lin, Storey & Szeri 2002). Although the model is able to replicate trends in bubble temperatures and associated sonochemical yields, it is not able to capture the diffusive damping of bubble motions, since neither of the limits that the model switches between have any damping.

1.3 Overview of contributions of this work

The main contributions of Part I of this thesis are as follows:

- Numerical validation of several assumptions that are often made to simplify full bubble computations and develop reduced-order models.
- Reduction of data from full bubble computations through application of proper orthogonal decomposition to temperature and concentration fields.
- Assessment of existing reduced-order models by comparison to full bubble computations.
- Development and assessment of an efficient and more accurate reduced-order model.

In Chapter 2 we present the full set of governing equations for a spherical bubble including heat and mass transfer, and the numerical method that was used to solve them. Results from some typical computations are presented to illustrate the basic features of the diffusive processes. Sequential assumptions that each simplify the

governing equations are implemented, with the impact of each simplification on the bubble dynamics being evaluated by comparison to more complete computations. A considerably simpler set of equations is shown to be valid over a wide parameter space. The proper orthogonal decomposition is then applied to the temperature and concentration fields as a means of distilling essential information from the large data set of computations.

Chapter 3 presents a reduced-order model that was motivated by the results of the previous chapter. Analysis of the model equations for linear oscillations and in the low Peclet number limit are presented. Comparisons of the present model, and other reduced-order models, are made to full computations for a wide range of bubble sizes and forcings.

Chapter 2

Spherical bubble dynamics

The goal of this chapter is to familiarize the reader with the complex diffusive processes that occur in and around a pulsating spherical bubble. Initially the equations describing the dynamics of a spherical bubble in an infinite liquid including the effects of energy and mass transfer are derived. The numerical method that is used to solve these equations is presented. A few typical computations are presented to illustrate some key aspects of the diffusive processes with particular regard given to their impact on bubble dynamics. These computations indicate possible simplifications that may be made to the full computations, and analyses are presented to determine under what situations such simplifications are valid. Finally, results of many computations over a large parameter space are presented in a concise manner by employing data reduction techniques, which enable important features to be distilled from the large data sets.

2.1 Governing equations

In this section the equations describing the motion of a spherical bubble consisting of a non-condensible gas and vapor in an incompressible liquid are derived. The diffusion equations describing energy transfer in and around the bubble, as well as the binary mass diffusion of the vapor in the gas phase and the dissolved gas in the liquid phase, are included in the derivation. The gas-vapor mixture is assumed to behave as a perfect gas, and the rate of phase change at the interface is assumed to be limited in

accordance to results from kinetic theory. Other assumptions are introduced as they are needed in the derivation.

2.1.1 Equations for liquid phase

The liquid phase consists of water with a small concentration of dissolved air. For the relatively low velocities considered here it is possible to assume that the density of the water is constant, and as a consequence of the very small mass concentration of dissolved air ($C_a = \mathcal{O}(10^{-5})$ at atmospheric pressure and 25°C) the density of the entire liquid phase is also approximately constant. This enables the mixture continuity equation to be integrated exactly to obtain an expression for the liquid velocity,

$$u_l = V \left(\frac{R}{r} \right)^2 , \tag{2.1}$$

where R is the bubble radius and

$$V \equiv \dot{R}. \tag{2.2}$$

In equation (2.1) the boundary condition $u_l|_{r=R} = V$ has been used. This comes from considering conservation of mass across the bubble wall and assuming the mass flux velocity through the bubble wall is far less than the bubble wall velocity ($\dot{m}_g''/\rho_l' \ll V'$). This assumption has been widely used in previous studies and also verified by analysis (Hao & Prosperetti 1999*a*) and full computations (Storey & Szeri 2000, Preston, Colonius & Brennen 2001).

Under the same assumptions, and also assuming constant liquid viscosity, the momentum equation for the liquid phase can be integrated to yield

$$\tilde{p}|_{r=R} - \tilde{p}_\infty(t) \;=\; R\dot{V} + \frac{3}{2}V^2 + \frac{4}{Re}\frac{V}{R} + \frac{2}{WeR} + \frac{4}{3}\frac{\mu}{Re}\left[\frac{\partial u}{\partial r} - \frac{u}{r}\right]_{r=R}, \quad (2.3)$$

where $\tilde{p}_\infty(t)$ is the specified far-field pressure in the liquid and Re and We will be defined shortly. Equation (2.3) is the well-known Rayleigh-Plesset equation, except the usual assumption of polytropic behavior for the bubble internal pressure has not been employed: the pressure in the gas phase at the bubble wall, $\tilde{p}|_{r=R}$, is instead determined by solving the full set of conservation equations in the gas phase. In addition the last term involving the gas viscosity, μ, and the gas velocity, u, is retained in the equation. This term is the viscous term resulting from applying conservation of momentum across the bubble wall and is negligible in most circumstances (Prosperetti et al. 1988). It should be noted that other forms of this equation that account for first-order corrections to the liquid compressibility (Prosperetti & Lezzi 1986) could be used in place of this equation.

In addition the equations for conservation of mass of air and energy in the liquid are

$$\frac{\partial C_a}{\partial t} + u_l\frac{\partial C_a}{\partial r} = \frac{1}{ScRe}\frac{1}{r^2}\frac{\partial}{\partial r}\left(r^2\frac{\partial C_a}{\partial r}\right), \quad (2.4)$$

$$\frac{\partial \tilde{T}_l}{\partial t} + u_l\frac{\partial \tilde{T}_l}{\partial r} = \frac{1}{PrRe}\frac{1}{r^2}\frac{\partial}{\partial r}\left(r^2\frac{\partial \tilde{T}_l}{\partial r}\right) + \frac{12}{Re}\left(\frac{u_l}{r}\right)^2, \quad (2.5)$$

where $C_a \equiv \rho_a/\rho_l$ is the mass concentration of dissolved gas in the liquid, and $\tilde{T}_l$ is the liquid temperature. The parameters Pr, Sc and Re are defined shortly. In equation (2.5) the energy flux due to mass diffusion of dissolved air in the water has been neglected because of the very small concentrations. This results in equations (2.4) and (2.5) not being directly coupled, enabling differently scaled solution grids to be easily used for each equation. This enables a more efficient numerical solution (Section 2.2). The far field boundary conditions for these two equations respectively are

$$\tilde{T}_{l_\infty} = const., \quad C_{a_\infty} = const., \tag{2.6}$$

while at the bubble wall the concentration and temperature are coupled to the bubble interior (Section 2.1.3).

In the above equations the dependent and independent variables have been non-dimensionalized in the following manner,

$$r = r'/R'_0 \quad t = \omega'_0 t' \quad R = R'/R'_0 \quad V = V'/R'_0\omega'_0$$
$$u_l = u'_l/R'_0\omega'_0 \quad \tilde{p} = p'/\rho'_l(R'_0\omega'_0)^2 \quad \tilde{T}_l = c'_{pl}T'_l/(R'_0\omega'_0)^2 \ ,$$

where R'_0 is the equilibrium bubble radius and ω'_0 is the undamped isothermal bubble natural frequency given by

$$\omega'_0 = \left\{ \frac{3(p'_{\infty_0} - p'_v) + 4S'/R'_0}{\rho'_l R'^2_0} \right\}^{1/2} . \tag{2.7}$$

In the above equation p'_{∞_0} is the ambient pressure, p'_v is the vapor pressure in the bubble at the ambient temperature and S' is the surface tension between the liquid and gas phases. The non-dimensionalization results in the following definitions of Reynolds, Weber, Schmidt and Prandtl numbers,

$$Re = \rho'_l R'^2_0 \omega'_0/\mu'_l \quad We = \rho'_l R'^3_0 \omega'^2_0/S'$$
$$Sc = \mu'_l/\rho'_l D'_l \qquad Pr = \mu'_l c'_{pl}/k'_l.$$

Finally, it is useful to define the pressure coefficient and cavitation number,

$$C_p(t) \equiv \tilde{p}_\infty(t) - \tilde{p}_{\infty_0}, \tag{2.8}$$
$$\sigma \equiv \tilde{p}_{\infty_0} - \tilde{p}_{v_0}, \tag{2.9}$$

where $\tilde{p}_{v_0} \equiv p'_v(T'_\infty)/\rho'_l(R'_0\omega'_0)^2$ is the non-dimensional vapor pressure evaluated at the

ambient temperature, T'_∞. Under the present non-dimensionalization σ is related to the Weber number by the non-dimensionalization of equation (2.7),

$$3\sigma + \frac{4}{We} = 1. \tag{2.10}$$

In the present computations the liquid properties, including the surface tension, have been assumed to be constant, and the effect of the small concentration of dissolved gas in the liquid on the liquid properties has been neglected. These are approximations, and in particular it is known that during violent collapse the liquid temperature at the bubble interface may briefly exceed the critical temperature resulting in a condition where there is no longer a clearly defined gas-liquid interface and the surface tension is effectively zero (Storey & Szeri 1999). However we make these and subsequent approximations on the premise that we are using the full bubble computation for developing and evaluating reduced-order models. These low-order models generally only account for first-order effects due to the mass and thermal diffusion, so it is reasonable to neglect the higher-order effects in the full computation.

2.1.2 Equations for gas phase

The gas phase consists of a mixture of air and water vapor. The conservation of mass for the mixture is written as

$$\frac{\partial \rho}{\partial t} + \frac{1}{r^2}\frac{\partial}{\partial r}\left(r^2 \rho u\right) = 0, \tag{2.11}$$

where ρ and u are the mixture density and velocity, respectively. Neglecting pressure, forced and thermal diffusion, and assuming Fick's Law holds for ordinary diffusion, conservation of mass of vapor in the mixture is written as

$$\frac{\partial \rho C}{\partial t} + \frac{1}{r^2}\frac{\partial}{\partial r}\left(r^2 \rho C u\right) = \frac{1}{ScRe}\frac{1}{r^2}\frac{\partial}{\partial r}\left(r^2 \rho D \frac{\partial C}{\partial r}\right), \tag{2.12}$$

where $C \equiv \rho_v/\rho$ is the mass concentration of vapor. Neglecting gravity and bulk viscosity the conservation of momentum for the mixture becomes

$$\frac{\partial \rho u}{\partial t} + \frac{1}{r^2}\frac{\partial}{\partial r}\left(r^2 \rho u^2\right) = -\frac{\partial \tilde{p}}{\partial r} + \frac{1}{Re}\frac{4}{3}\left\{\frac{1}{r^2}\frac{\partial}{\partial r}\left(r^2 \mu\left[\frac{\partial u}{\partial r} - \frac{u}{r}\right]\right) + \frac{\mu}{r}\left[\frac{\partial u}{\partial r} - \frac{u}{r}\right]\right\} \tag{2.13}$$

where the pressure is given by the perfect gas law,

$$\tilde{p} \;=\; \rho \mathcal{R} \tilde{T}. \tag{2.14}$$

Here $\tilde{T}$ is the gas temperature and the effective gas constant is given by a mass weighted average of each of the components,

$$\mathcal{R} = C\mathcal{R}_v + (1 - C)\,\mathcal{R}_a. \tag{2.15}$$

The perfect gas constant of each component is computed as

$$\mathcal{R}_a = \mathfrak{R}_u / M_a, \tag{2.16}$$

$$\mathcal{R}_v = \mathfrak{R}_u / M_v. \tag{2.17}$$

where M_a and M_v are the molecular weights of the air and vapor, and $\mathfrak{R}_u$ is the universal gas constant. Assuming Fourier's Law for heat conduction, and using the perfect gas law to substitute $\tilde{T}$ in place of the specific internal energy, the conservation of energy for the mixture becomes

$$c_v \left\{ \frac{\partial \rho \tilde{T}}{\partial t} + \frac{1}{r^2}\frac{\partial}{\partial r}\left(r^2 \rho u \tilde{T} \right) \right\} = \frac{1}{RePr}\frac{1}{r^2}\frac{\partial}{\partial r}\left(r^2 k \frac{\partial \tilde{T}}{\partial r} \right) - \tilde{p}\frac{1}{r^2}\frac{\partial}{\partial r}\left(r^2 u \right) + \frac{4}{3}\frac{\mu}{Re}\left[\frac{\partial u}{\partial r} - \frac{u}{r} \right]^2 + \frac{1}{ReSc}\Theta, \quad (2.18)$$

where, c_v is the specific heat at constant volume for the gas mixture. This is assumed to be given by a simple mass fraction weighted average of the individual components,

$$c_v = C c_{vv} + (1 - C)\, c_{va}. \quad (2.19)$$

The specific heats for each of the components are assumed to be constant and are computed from

$$c_{va} = \frac{\mathfrak{R}_u}{M_a\left(\gamma_a - 1\right)}, \quad (2.20)$$

$$c_{vv} = \frac{\mathfrak{R}_u}{M_v\left(\gamma_v - 1\right)}, \quad (2.21)$$

where γ_a and γ_v are the constant ratio of specific heats of the air and vapor, respectively. The last term in equation (2.18) represents the transfer of energy due to inter-diffusion of the air and vapor is given by

$$\Theta = \left[\left(\gamma_v - 1\right) c_{vv} - \left(\gamma_a - 1\right) c_{va} \right] \tilde{T}\frac{1}{r^2}\frac{\partial}{\partial r}\left(r^2 \rho D \frac{\partial C}{\partial r} \right) + \left[\gamma_v c_{vv} - \gamma_a c_{va} \right] \rho D \frac{\partial \tilde{T}}{\partial r}\frac{\partial C}{\partial r}. \quad (2.22)$$

The contribution of this last term is a higher-order effect and is neglected for the same reasons as discussed in Section 2.1.1. In addition a few computations including the last term were performed and found to give results that were virtually indistinguishable

from computations where it was neglected.

The equations in the gas phase are furnished with five symmetry conditions at the bubble center, $r = 0$,

$$\frac{\partial \rho}{\partial r} = 0, \quad \frac{\partial C}{\partial r} = 0, \quad u = 0, \quad \frac{\partial \tilde{p}}{\partial r} = 0, \quad \frac{\partial \tilde{T}}{\partial r} = 0. \tag{2.23}$$

To complete the full set of bubble equations and to connect the gas domain to the liquid domain we apply conservation laws across the interface in Section 2.1.3.

In the above equations the gas mixture density is non-dimensionalized by the constant liquid density, while the other variables are non-dimensionlized in an identical manner to their counterparts in the liquid domain, viz,

$$\begin{array}{ccc} r = r'/R'_0 & t = \omega'_0 t' & \rho = \rho'/\rho'_l \\ u = u'/R'_0\omega'_0 & \tilde{p} = p'/\rho'_l(R'_0\omega'_0)^2 & \tilde{T} = c'_{pl}T'/(R'_0\omega'_0)^2. \end{array}$$

We also make frequent use of the alternative non-dimensional pressures and temperatures,

$$p = \tilde{p}/\tilde{p}_0 \quad T = \tilde{T}/\tilde{T}_0,$$

where $\tilde{p}_0 = \tilde{p}_{\infty_0} + 2/We$ is the initial pressure in the bubble, and $\tilde{T}_0 = \tilde{T}_{l_\infty}$ is the initial bubble temperature. In particular, we use these variables in all plots and in the development of the reduced-order model in Chapter 3.

The mass diffusivity of the gas mixture and the transport properties of the individual gas components are assumed constant and are non-dimensionalized by their respective liquid values, while the gas constants are non-dimensionalized by the specific heat of the liquid. That is,

$$D \equiv D'/D'_l \quad \mu \equiv \mu'/\mu'_l \quad k \equiv k'/k'_l \quad c_v \equiv c'_v/c'_{vl} \quad \mathcal{R} \equiv \frac{\mathcal{R}'}{c'_{pl}} \quad \mathfrak{R}_u \equiv \frac{\mathfrak{R}'_u}{c'_{pl}}.$$

Previous studies have shown relatively small differences due to using transport properties that are dependent upon temperature (Vuong & Szeri 1996), and for reasons

stated in Section 2.1.1 we neglect these higher-order effects and assume constant values.

Note that under the present non-dimensionalization, Re, Sc and Pr appearing in equations (2.12), (2.13) and (2.18) are the same as those defined in Section 2.1.1 using the liquid properties, rather than the perhaps more conventional method of defining them by the initial gas properties. This approach has the advantage of obtaining much cleaner forms for the conservation equations over the bubble interface in Section 2.1.3 as well as resulting in the more familiar form of the Rayleigh-Plesset equation (2.3) in Section 2.1.1.

The viscosity and conductivity for the gas mixture are given by the semi-empirical formulae for n components (Bird, Stewart & Lightfoot 1960),

$$\mu = \sum_{i=1}^{n} \frac{x_i \mu_i}{\sum_{j=1}^{n} x_j \phi_{ij}}, \tag{2.24}$$

$$k = \sum_{i=1}^{n} \frac{x_i k_i}{\sum_{j=1}^{n} x_j \phi_{ij}}, \tag{2.25}$$

where

$$\phi_{ij} \equiv \frac{1}{\sqrt{8}} \left[1 + \frac{M_i}{M_j}\right]^{-1/2} \left[1 + \left(\frac{\mu_i}{\mu_j}\right)^{1/2} \left(\frac{M_j}{M_i}\right)^{1/4}\right]^2 . \tag{2.26}$$

Here, x_i and M_i are the mole fraction and molecular weight of component i. Equations (2.24) and (2.25) are strictly only valid for low density non-polar gases, but we use them here on the premise that we are only using the full computations to develop and test reduced order models of heat and mass transfer that do not include these higher-order effects. It is of interest to note that for the air-vapor mixture considered here, the molecular masses of the components are not too dissimilar and equations (2.24) and (2.25) can be approximated by relations that depend linearly on the mixture composition. A few such computations were performed with negligible

impact on the results. Nonetheless, all results presented herein use equations (2.24) and (2.25).

2.1.3 Interface conditions

To link the equations in the gas and liquid domains together we require conservation of mass (both mixture and individual species), momentum and energy across the moving bubble interface. Conservation of the mass of mixture and momentum have already been used in deriving equations (2.1) and (2.3), respectively. Conservation of mass of one of the individual species (in this case air) requires

$$\dot{m}''_a = \frac{-1}{ScRe}\rho D\frac{\partial C}{\partial r} - \rho\left(1-C\right)\left(u-V\right) = \frac{1}{ScRe}\frac{\partial C_{al}}{\partial r}, \tag{2.27}$$

where $\dot{m}''_a = \dot{m}'''_a/\rho'_l R'_0\omega'_0$ is the non-dimensional mass flux of air per unit area across the interface (positive for flow into bubble). Conservation of energy can be written as

$$\begin{aligned} L\dot{m}''_v &= \frac{1}{PrRe}\left[\frac{\partial \tilde{T}_l}{\partial r} - k\frac{\partial \tilde{T}}{\partial r}\right] \\ &+ \left(u-V\right)\left[\rho\left(c_v\tilde{T}+\frac{1}{2}u^2\right) + \tilde{p} - \frac{4}{3}\frac{\mu}{Re}\left(\frac{\partial u}{\partial r} - \frac{u}{r}\right)\right], \end{aligned} \tag{2.28}$$

where $L = L'/(R'_0\omega'_0)^2$ is the non-dimensional latent heat associated with phase change at the interface, and $\dot{m}''_v = \dot{m}'''_v/\rho'_l R'_0\omega'_0$ is the non-dimensional mass flux of vapor per unit area across the interface [positive for flow into bubble (evaporation)]. In deriving equation (2.28), simplifications have been made by subtracting the product of the interface velocity and conservation of momentum at the interface and then neglecting terms consistent with those neglected in deriving equation (2.1). In addition those terms associated with energy transport due to inter-diffusion of species have been neglected which is consistent with neglecting the last term in equation (2.18).

Two more conditions are obtained by assuming that the interface is in thermal equilibrium, and that Henry's Law is satisfied,

$$\begin{aligned} \tilde{T} &= \tilde{T}_l \equiv \tilde{T}_w, && (2.29) \\ C_a &= H\tilde{p}_a \\ &= H\rho\,(1-C)\,\mathcal{R}_a\tilde{T}, && (2.30) \end{aligned}$$

where $H = H'\rho_l'(R_0'\omega_0')^2$ is the non-dimensionalized Henry's constant. Equations (2.27) through (2.30) link the gas and liquid domains through the temperatures and concentrations, and their first spatial derivatives, at the interface. The final condition comes from considering phase equilibrium between the vapor and the water. Based on molecular dynamics we can determine an expression for the mass flux of vapor out of the bubble,

$$\dot{m}_v'' = \alpha\frac{\tilde{p}_{v_{sat}}(\tilde{T}) - \tilde{p}_v}{\sqrt{2\pi\mathcal{R}_v\tilde{T}}}, \tag{2.31}$$

which is then equated to the mass flux of vapor due to bulk motion and reciprocal diffusion on the gas side of the interface,

$$\dot{m}_v'' = \frac{1}{ScRe}\rho D\frac{\partial C}{\partial r} - \rho C\,(u-V)\,. \tag{2.32}$$

Recall that $\dot{m}_v''$ is positive for flow into the bubble (evaporation). In equation (2.31) $\tilde{p}_{v_{sat}}$ is the temperature-dependent saturation pressure of water vapor in air, and α is the experimentally determined accommodation coefficient. There is some discord as to the appropriate value of α (Brennen 1995) and unless stated otherwise we use $\alpha = 0.4$, which is consistent with Matsumoto & Takemura (1994) and Storey & Szeri (2000). The effect of using other values of accommodation coefficient is examined in

Section 2.4.3. Using the perfect gas law we can also re-write the vapor pressure at the bubble wall as

$$\tilde{p}_v = \rho C \mathcal{R}_v \tilde{T}. \tag{2.33}$$

The functional dependence of the saturation vapor pressure on temperature, $\tilde{p}_{v_{sat}}(\tilde{T})$, is given in Appendix A.

2.2 Numerical method

Following Hao & Prosperetti (1999*a*) we transform the bubble interior and semi-infinite exterior to fixed finite domains,

$$r \in [0, R(t)] \quad \rightarrow \quad y \in [0, 1], \tag{2.34}$$

$$r \in [R(t), \infty) \quad \rightarrow \quad x \in (0, 1], \tag{2.35}$$

with the following mappings,

$$y \equiv \frac{r}{R(t)}, \tag{2.36}$$

$$x \equiv \frac{l}{l + r - R(t)}, \tag{2.37}$$

where l is an appropriate scaling factor. Since the two diffusion equations (2.4) and (2.5) in the liquid are not directly coupled (Section 2.1.1), it is possible to use different values of l for each of the equations. This is extremely beneficial since, for air and water at 25°C, the diffusion length scale for mass diffusion is about an order of magnitude less than that for thermal diffusion. We use the following scaling factors for the thermal and mass problems respectively,

$$l_T = \frac{B_T}{\sqrt{PrRe}}, \tag{2.38}$$

$$l_C = \frac{B_C}{\sqrt{ScRe}}. \tag{2.39}$$

For the computations presented we use $B_T = 29$ and $B_C = 35$, and numerical experiment indicated the halving or doubling of these values had no significant impact on the solution.

The rescaled equations are spatially discretized using a spectral collocation method based on Chebychev polynomials for both the gas and liquid domains. For computations involving only the bubble interior, Kamath & Prosperetti (1989) found that a Galerkin formulation was superior to the collocation formulation since it conserved mass within the bubble even when only a few modes were used. Here the collocation method has been chosen because it enables the interface conditions between the bubble interior and exterior to be implemented.

The computation uses an adaptable number of Chebychev modes in each of the domains. If the ratio of the amplitudes of the highest mode to the lowest mode is greater than some small parameter (ϵ_y for the bubble interior, and ϵ_x for the bubble exterior), then two more modes are added. If the ratio becomes less than $1/100^{th}$ of the small parameter, then two modes are removed. Special care is taken to ensure that the parameters are small enough to conserve mass of the bubble contents to within a few percent, which for most computations was able to be obtained with $\epsilon_y = 10^{-6}$ and $\epsilon_x = 10^{-5}$. Less accurate computations, where the error in the mass conservation is larger than a few percent, showed only negligible differences in the radial bubble dynamics. This is consistent with the results of Prosperetti et al. (1988).

The following collocation points are used for the interior and exterior domains,

$$y_j \equiv \cos\frac{\pi(j-1)}{2N_y+1}, \quad j = 1, 2, \ldots, N_y + 1 \tag{2.40}$$

$$x_j \equiv \cos\frac{\pi(j-1)}{2N_x}, \quad j = 1, 2, \ldots, N_x + 1, \tag{2.41}$$

where N_y and N_x are the number of modes used in each of the domains. Note that the choice for the y_j avoids the location of a grid point at the bubble center ($y = 0$) and hence the coordinate singularity is avoided (Mohseni & Colonius 2000), while the choice for x_j results in a grid point at $x = 0$ enabling boundary conditions to be specified as $r \to \infty$. The above choices also have the desirable feature of a higher density of grid points near the bubble interface. To avoid aliasing errors due to the non-linear terms, the highest one-third of the modes in the interior domain are filtered out at each time step (Canuto, Hussaini, Quarteroni & Zang 1988).

To automatically satisfy the symmetry conditions (2.23) at the bubble center, only even Chebychev polynomials are used for the expansions of ρ, C and $\tilde{T}$, while odd polynomials are used for u. Similarly only even polynomials are used for the expansions of C_l and $\tilde{T}_l$, which enforces the condition of zero gradient at infinity, which follows from the far field boundary conditions (2.6). The interface conditions are enforced by evaluating the discrete forms of equations (2.27) through (2.33) at the common collocation points, $y_1 = x_1 = 1$. The resulting equations are manipulated into two equations which are non-linear in the interface values of temperature, $\tilde{T}_1$, and concentration, C_1. These are then solved at each time step using Newton-Raphson iterations.

The equations are integrated in time using a fourth-order adaptive time step Runge-Kutta scheme (Press, Teukolsky, Vettering & Flannery 1994). This explicit method, combined with the clustered grid spacing and the diffusive terms in the equations, places severe stability limits on the maximum size of the time step that can be used. This limit can be expressed as

$$\Delta t < \frac{const.}{N^4}, \tag{2.42}$$

where N is the number of Chebychev modes used in either domain. This is of concern

during violent collapse when many Chebychev modes are required in both domains to obtain a fully resolved solution. For most computations it is the resolution of the solution in the liquid, and in particular the concentration field, that is most restrictive. In practice it was found that the maximum number of modes possible in each of the domains during bubble collapse was about 70, before the stability condition (2.42) resulted in the time step becoming restrictively small.

Another instability can also arise when the bubble experiences large growth. For stability, the following condition on the cell Peclet number is required to be satisfied (Ferziger & Peric 1999),

$$Pe_{cell} \equiv \frac{u\Delta r}{\tilde{D}} = \frac{uR\Delta y}{\tilde{D}} < 2, \tag{2.43}$$

where $\tilde{D} \equiv \min\{\frac{D}{ScRe}, \frac{\mu}{\rho Re}, \frac{k}{\rho c_p RePr}\}$. For most computations this condition is met by restricting the minimum number of modes used in each domain to be 12, thereby resulting in a small enough grid spacing, Δy. In situations where R becomes too large it is necessary to use additional modes during the expansion.

To validate the numerical solutions some standard convergence tests were carried out. Figure 2.1(a) tests the interior solution by focusing on a cold liquid (25°C) where the exterior field has negligible impact on the bubble dynamics (Sections 2.4.1 and 2.4.2). The relative errors in some key variables (defined in Figure 2.3) are plotted for computations with different values of N_y. For this plot each computation used a fixed (rather than adaptive) number of modes. Any errors due to time integration were removed by using a very small value of the parameter ϵ_t, which controls the adaptive time stepping. The relative errors were computed by assuming a computation with a higher number of modes (in this case $N_y = 18$) to be the exact solution. The figure shows that the error in each of the variables decreases exponentially as the number of modes is increased linearly, thus demonstrating the expected spectral convergence.

Figure 2.1(b) tests the exterior solution by focusing on a hot liquid (95°C) where the external temperature field is crucial in determining the bubble dynamics (Section

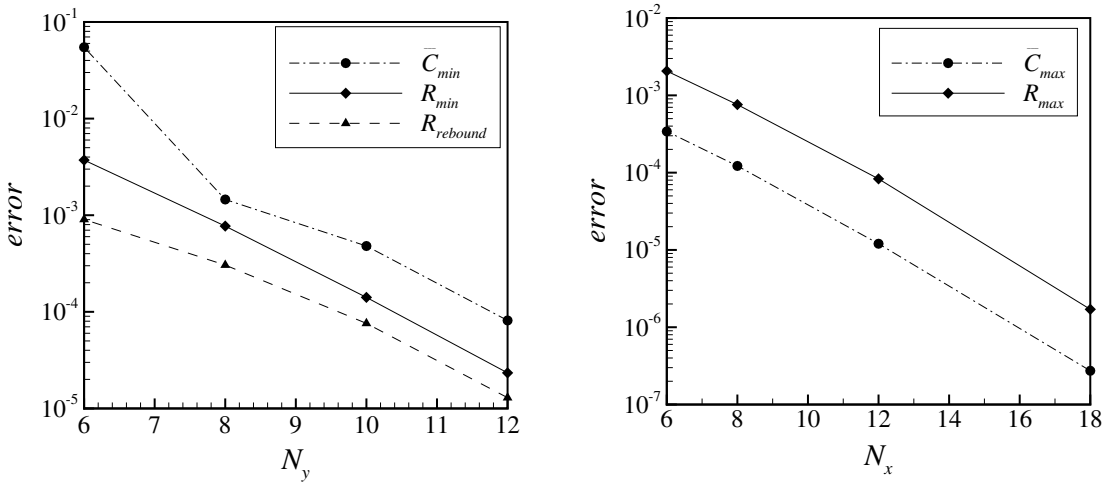

(a) Bubble interior (25°C). (b) Bubble exterior (95°C).

Figure 2.1: Errors in values of selected variables as a function of the number of modes ($\epsilon_t = 10^{-9}$). Spectral convergence is demonstrated for both the interior and exterior solutions.

2.3.2). The relative errors in some key variables (defined in Figure 2.6) are plotted for computations with different values of N_x. For the error calculations in this case a computation with $N_x = 32$ was assumed to be an exact solution. The impact of errors in the internal solution is removed by using many modes for the interior, thus ensuring any such errors are negligible compared to errors associated with the external solution. The figure again shows the expected spectral convergence. The general method for the external solution was also tested by comparing a computed solution to an analytical solution for the same test problem as used in the appendix of Hao & Prosperetti (1999*a*).

The impact of the time step parameter ϵ_t, which controls the adaptive time stepping was investigated in Figure 2.2 by plotting the errors of some key variables for different values of ϵ_t. The relative errors for this plot were calculated by assuming a computation with $\epsilon_t = 10^{-11}$ to be the exact solution. As expected, there is an order of magnitude decrease in the error as ϵ_t is reduced by an order of magnitude. Interestingly, the errors in $\bar{C}_{min}$ are about three orders of magnitude higher than the errors associated with bubble dynamics, indicating that a small value of ϵ_t must be used to accurately compute $\bar{C}_{min}$. In most of the computations presented $\epsilon_t = 10^{-8}$

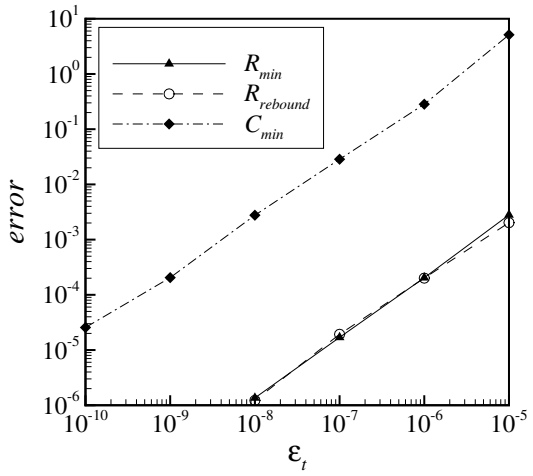

Figure 2.2: Errors in selected variables for different values of time step parameter, ϵ_t ($\epsilon_y = 10^{-6}$). The errors show the expected reduction as ϵ_t is decreased.

was found to give sufficiently accurate results.

2.3 Typical computations

In this section we present some results from typical computations for single bubbles that have been subjected to the following Gaussian decrease in the far field pressure,

$$\tilde{p}_\infty(t) = \tilde{p}_{\infty_0}\left(1 - A\exp\left[-((t-t_0)/t_w)^2\right]\right), \tag{2.44}$$

where the amplitude, A, and width, t_w, are typically chosen to mimic conditions encountered by a bubble convecting through the nozzle considered in Part II. Two computations are presented for illustrative purposes; one for a *cold* liquid and the other for a *hot* liquid. Plots of computed bubble radius, internal pressure, temperatures and concentrations as functions of time, as well as temperature and concentration distributions within and around the bubble at various times of the bubble motion are presented in order to illustrate the diffusive processes for the two different bubble motions.

2.3.1 *Cold* liquid

The precise definition of a cold liquid will become apparent in Section 2.4.2, but for now it is sufficient to note that the present computation is for an air-vapor bubble in water at 25°C. The full set of non-dimensional parameters for this typical cold computation (and all other computations) are listed in Appendix A. The run numbers in each of the figure captions refer to those listed in Tables A.2 and A.3. Figures 2.3(a) and (b) respectively plot the computed bubble radius and bubble pressure. They exhibit the typical behavior of an *inertially controlled* bubble with strong bubble collapses leading to small minimum radii and high bubble pressures. The bubble pressure, p, plotted here is the pressure at the bubble center, and it is found in practice that the pressure at the bubble wall is almost identical (except for a very short time around when the bubble minimum radius occurs). This near spatial uniformity of internal bubble pressure is exploited in Section 2.4.4.

Figures 2.3(c) and (d) respectively plot the average bubble temperature and vapor concentration together with the values at the bubble center (subscript c) and wall (subscript w). It is noticed that the changes in the bubble wall temperature are about two orders of magnitude lower than the changes in the average or center temperatures. This is a result of the liquid being *cold*, which as discussed in Section 2.4.2, can be exploited in models. The significant differences between the center, average and wall values for both the temperature and concentration illustrate the existence of substantial spatial gradients within the bubble, and indicates the importance of the diffusive processes. In particular, while C_w becomes small during collapse, $\bar{C}$ and especially C_c are well above zero indicating that the relatively slow mass diffusion is trapping the vapor in the bubble on collapse (Matsumoto & Takemura 1994, Storey & Szeri 2000). In addition the finite rate of mass diffusion during the initial growth and rebounds has the effect of limiting the extent of bubble growth as will be demonstrated in the later part of Section 3.5.1.

Also indicated in Figure 2.3 are the maximum radius obtained during the first growth, R_{max}, the second maximum radius obtained on the first rebound, $R_{rebound}$, the

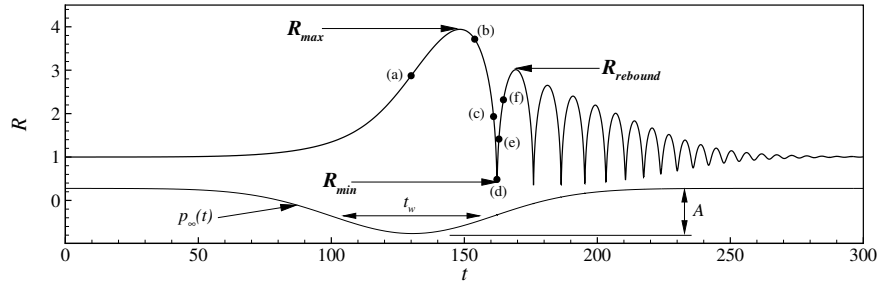

(a) Radius

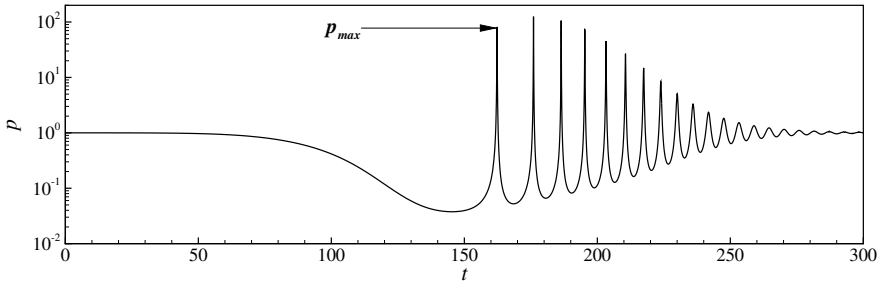

(b) Pressure

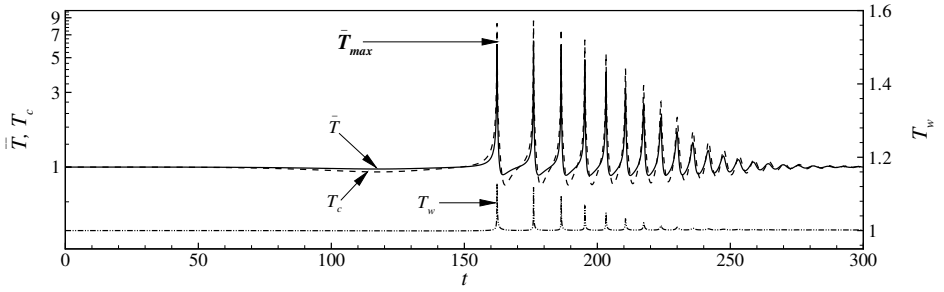

(c) Temperatures

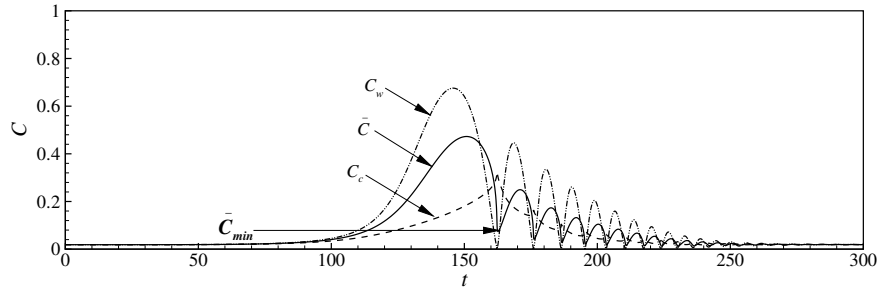

(d) Concentrations

Figure 2.3: Bubble radius, bubble pressure, temperatures and concentrations for an air-vapor bubble in *cold* water. The typical behavior of an inertially controlled bubble is exhibited, with strong bubble collapses leading to small minimum radii and high bubble pressures and temperatures. [Run 40,100(d)].

minimum radius, R_{min}, maximum bubble pressure, p_{max}, maximum average bubble temperature, $\bar{T}_{max}$, and minimum average vapor concentration, $\bar{C}_{min}$, all obtained in the first collapse. Some of these defined quantities have already been used for demonstrating numerical convergence in Section 2.2 and they will also be used to measure the accuracy of reduced-order models compared to full computations in Section 3.5.

The complex diffusive processes occurring in and around the bubble are illustrated in Figure 2.4 which plots the the temperature and concentration profiles for the six times indicated by dots in Figure 2.3(a). It is immediately apparent that the liquid temperature remains relatively undisturbed. The profiles of the gas temperature are close to quadratic in y for the slow bubble motion during initial growth in (a) and (b). During collapse, (d), there is clearly some steepening of the temperature profile near the bubble wall, which suggests a more adiabatic behavior. Shortly after collapse, (e), the profile is interesting in that it is no longer monotonic. In fact, if we define the instantaneous heat transfer coefficient,

$$\beta_T \equiv \frac{-\partial T/\partial y|_{y=1}}{\bar{T} - T_w}, \tag{2.45}$$

then we see that β_T is negative during part of the cycle. This is more clearly illustrated in Figure 2.5(a) which plots the temperature gradient at the bubble wall as a function of the difference between the average and wall temperature. Again the six instances in time, (a)-(f), are marked on the plot. We see in the inset that point (e) is in the first quadrant which implies that $\beta_T < 0$. In addition the inset indicates that there is also a short time in a collapse rebound cycle spent in the third quadrant where again β_T is negative. This perhaps counter-intuitive result can be predicted by linear theory where it is caused by a phase lag between the temperature gradient and average bubble temperature (Section 3.2). It was first identified for non-linear computations by Nigmatulin et al. (1981) who explained that on bubble collapse the heat from the compression heating is conducted to the liquid by the large thermal gradient, while during initial expansion, heat conduction is not able to compensate

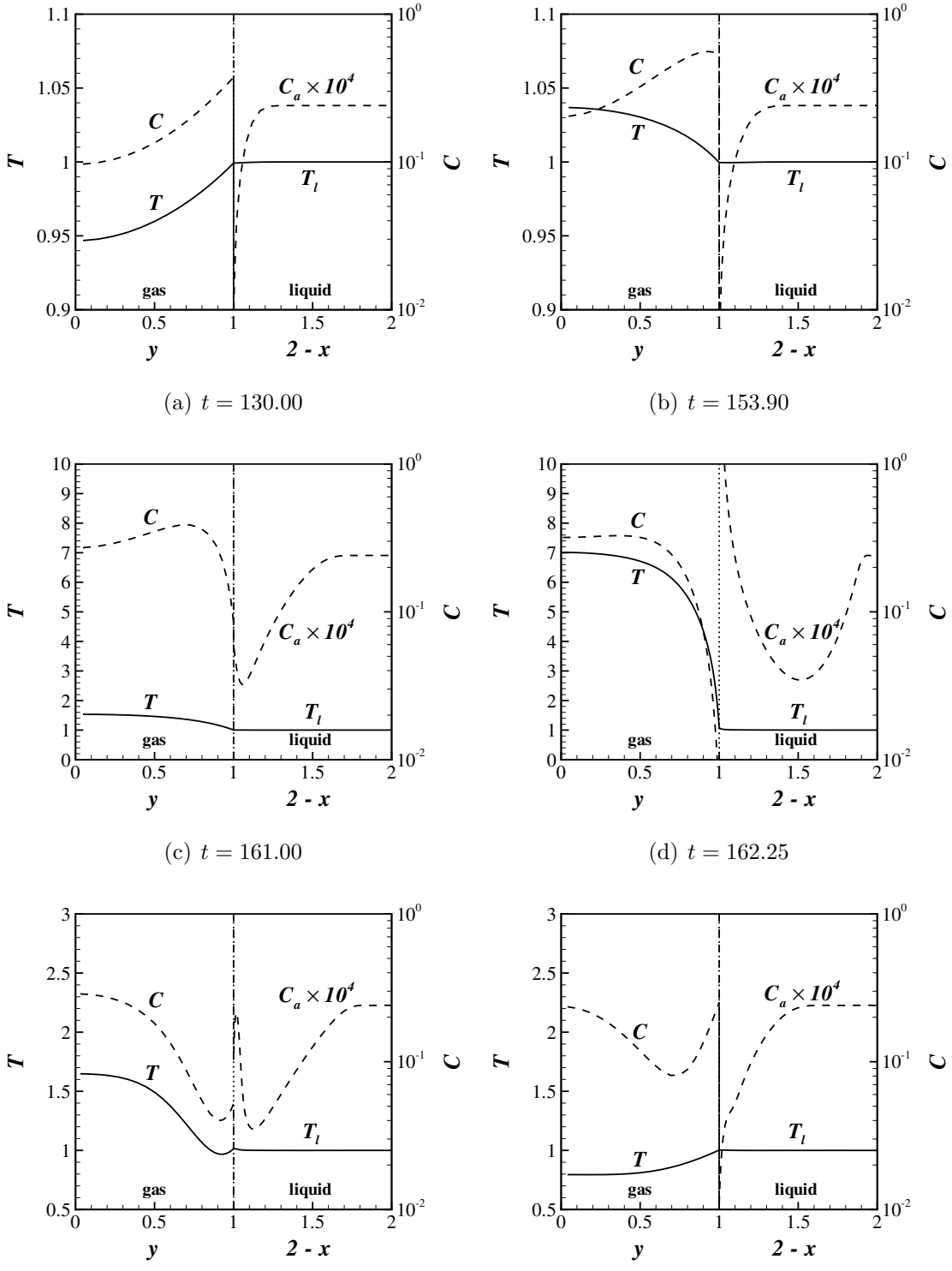

(a) $t = 130.00$

(b) $t = 153.90$

(c) $t = 161.00$

(d) $t = 162.25$

(e) $t = 163.00$

(f) $t = 164.70$

Figure 2.4: Temperature and concentration profiles at different time instances for the computation of Figure 2.3. The profiles in the bubble interior illustrate the complex diffusive behavior for the inertially controlled bubble.

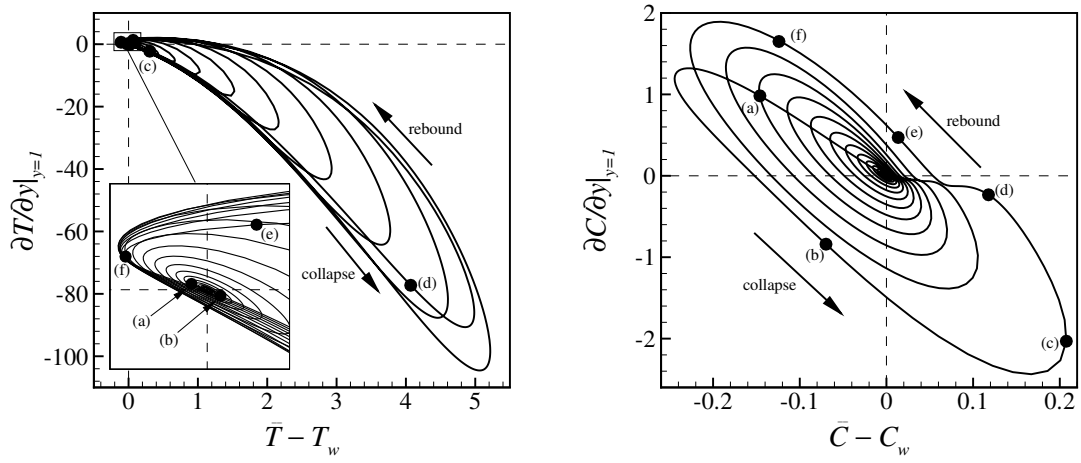

(a) Temperature (b) Concentration

Figure 2.5: Gradients at the bubble wall versus the difference between the average and wall values for temperature and concentration for a bubble in a *cold* liquid. The complicated heat and mass transfer processes, including negative instantaneous heat and mass transfer coefficients (β_T and β_C), are illustrated. The computation is for that of Figure 2.3.

for the cooling of the gas wall layers caused by expansion.

The profiles for the concentration of vapor within the bubble in Figure 2.4 are not quite as simple as the corresponding temperature counterparts. This is perhaps because the mass diffusion is forced by the time varying concentration at the bubble wall, while the thermal diffusion is forced by the compression heating term acting (relatively uniformly) over the bubble interior with the wall temperature remaining practically constant. Nonetheless, at certain times, there are close parallels with the temperature profiles, particularly at instances (a), (d) and (e). Figure 2.5(b) which plots the concentration gradient at the bubble wall versus the difference between the average and wall concentrations indicates that once again the point representing instant (e) is in the first quadrant. This implies that the instantaneous mass transfer coefficient, β_C, (which is defined analogously to β_T) is negative. In addition there is considerable time spent in the third quadrant, where β_C is also negative as indicated by time instant (b). As with the heat transfer situation the linear analysis of Section 3.2 indicates that this phenomena is caused by the phase lag between the

concentration gradient and the average concentration. In fact the shape of the loops in this plot are quite similar to that for the linear analysis in Figure 3.2, with the inward spiraling in the full computation originating from the fact that the rebound amplitudes are attenuating in contrast to the steady-state amplitude in the (forced) linear analysis.

Figure 2.4 illustrates the relatively complex behavior of the mass concentration of air in the liquid phase, C_a. During the initial expansion [(a) and (b)] the concentration decreases near the bubble wall due to the partial pressure of air in the bubble decreasing as a result of both the overall bubble expansion and the increased vapor content of the bubble. This causes air to diffuse into the bubble and results in a depleted layer of liquid around the bubble where C_a is lower than the equilibrium value. As the bubble collapses [(c) and (d)] the concentration at the wall rapidly increases as air is forced from the bubble. The collapse happens on a timescale that is fast compared to diffusion and as a result the depletion layer remains in the liquid, but at some distance from the bubble wall. On bubble rebound [(e)] the concentration at the bubble wall begins to decrease until the situation in [(f)] is reached where once again air is diffusing into the bubble. The very steep gradients near the bubble wall that occur during certain instances in the collapse and rebound cycle makes this part of the computation very difficult to resolve. In Section 2.4.1 conditions are determined for which the diffusion of the air in the liquid phase can be neglected, thereby substantially reducing the computation time.

2.3.2 *Hot* liquid

Results for a typical computation in a *hot* liquid (air-vapor bubbles in water at 95°C) are presented to emphasize the differences in bubble dynamics and diffusive processes for hot and cold liquids. The equilibrium bubble radius and forcing width are the same as in the previous section, with the forcing amplitude being reduced to result in approximately the same maximum bubble radius. Figure 2.6 plots the computed bubble radius, pressure, temperatures and concentrations as a function of

time. The curves for this *thermally controlled* growth and collapse are far smoother than the inertially controlled counterparts observed for the cold liquid computation. The reason for the different behavior between hot and cold liquids is that the slope of the vapor saturation curve is greater at higher temperatures (see Figure A.1). Hence, when the bubble wall temperature is cooled slightly during bubble expansion, there is a larger drop in vapor pressure for the hot liquid. This results in a substantially reduced bubble growth. The opposite effect also inhibits collapse of a bubble in a hot liquid.

Due to the slow timescale of bubble collapse in the thermally controlled situation, the temperatures and concentrations in Figure 2.6(c) and (d) display simple behavior with the center, average and wall values all changing in phase with each other. The simple monotonic profiles within the bubble are illustrated in Figure 2.7, which plots the temperature and concentration distributions at the six time instances represented by dots in Figure 2.6(a). Also apparent is the substantial variation of liquid temperature, due to the reasons previously discussed. For clarity the concentration of air in the liquid is not shown, but the effect of diffusion of air is very minor, because the bubble consists primarily of vapor.

Finally, plots of temperature and concentration gradients at the bubble wall versus the difference in the average and wall values are plotted in Figure 2.8. Plots for both the temperature and concentration further illustrate the relatively simple behavior as compared to the inertially controlled case, with only a small phase difference between the flux and average values.

2.4 Simplifying the equations

The set of equations and interface conditions developed in Section 2.1 are complex and, as mentioned in Chapter 1, have been simplified by many authors in order to enable more efficient computations. Often the simplifications are only justified by scaling arguments, without recourse to any direct numerical validation. Since the simplifications are also used in the development of reduced-order models, it is important

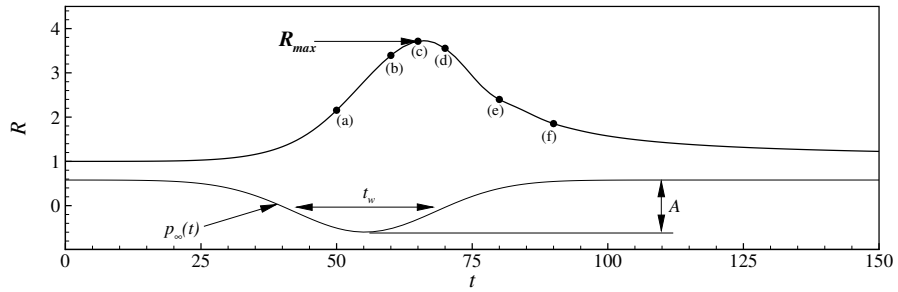

(a) Radius

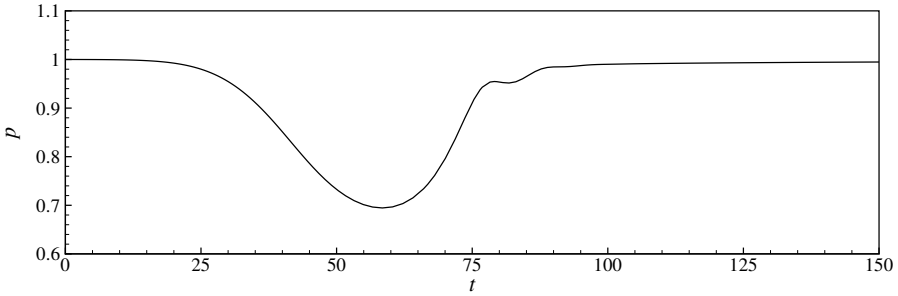

(b) Pressure

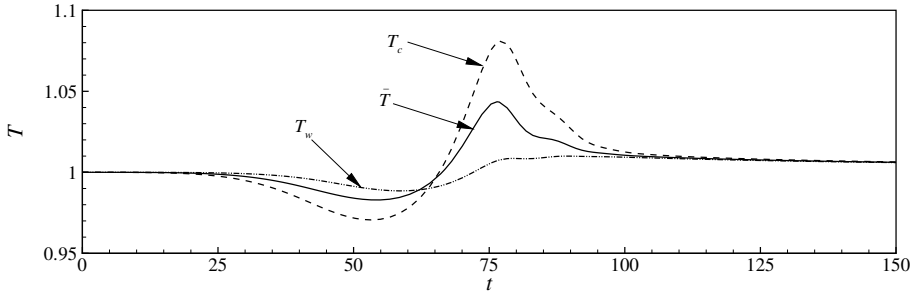

(c) Temperatures

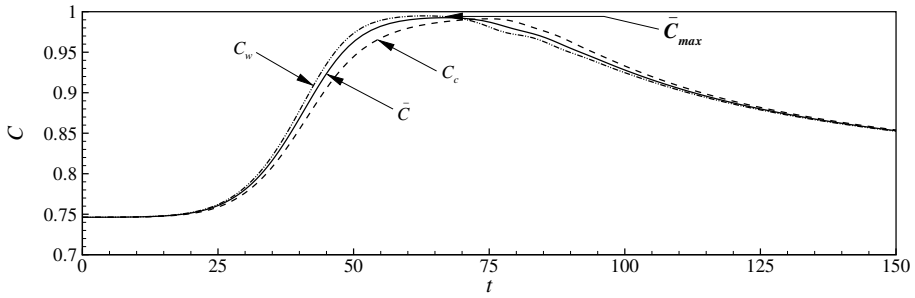

(d) Concentrations

Figure 2.6: Bubble radius, bubble pressure, temperatures and concentrations for an air-vapor bubble in *hot* water. The relatively smooth curves illustrate the typical behavior of a thermally controlled bubble. [Run 40,100(95)].

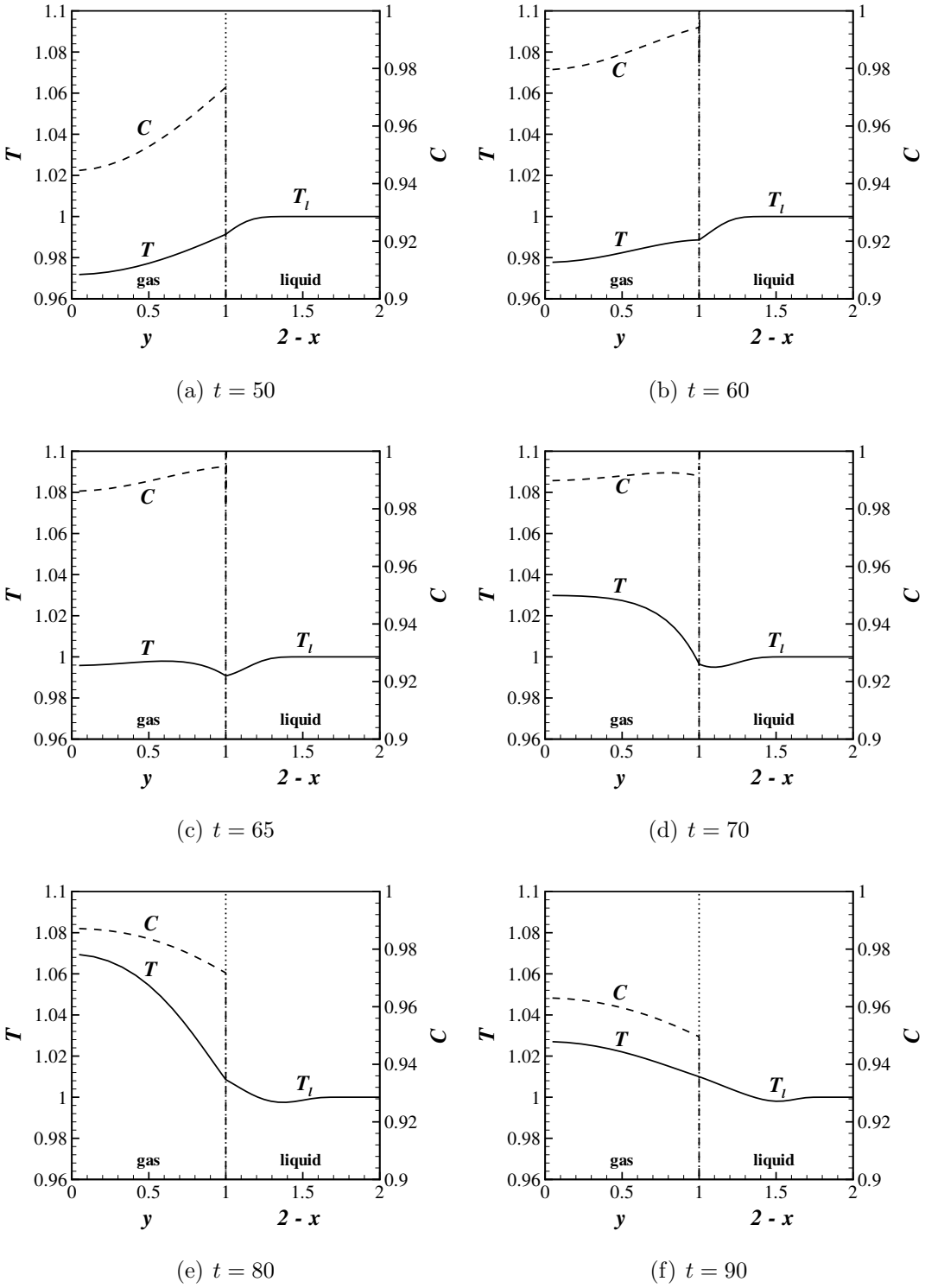

(a) $t = 50$ (b) $t = 60$

(c) $t = 65$ (d) $t = 70$

(e) $t = 80$ (f) $t = 90$

Figure 2.7: Temperature and concentration profiles at different times for the computation of Figure 2.6. The profiles in the bubble interior are generally monotonic due to the slow timescales of the thermally controlled bubble. The substantial variation of the liquid temperature field is clearly illustrated.

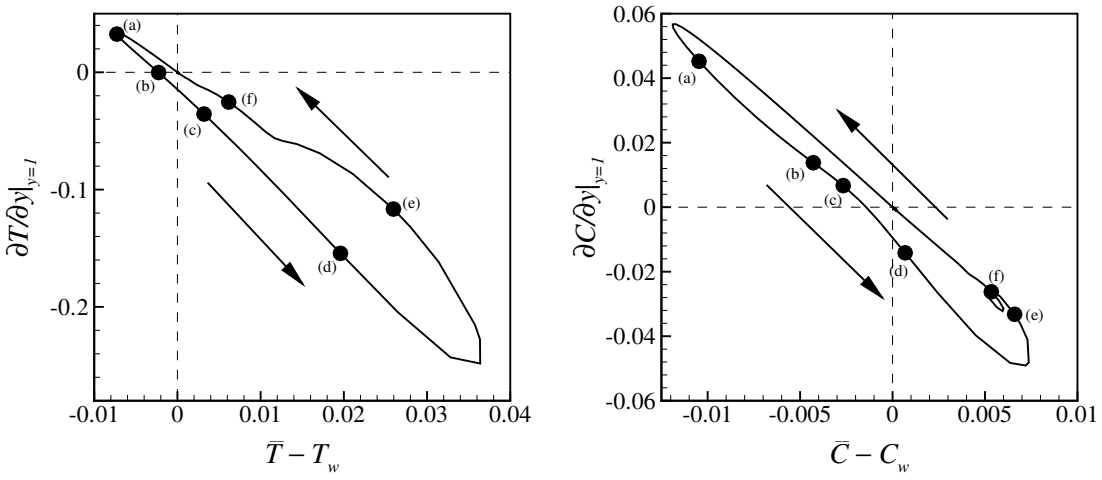

(a) Temperature (b) Concentration

Figure 2.8: Gradients at the bubble wall versus the difference between the average and wall values for temperature and concentration for a bubble in a *hot* liquid. The relatively simple internal diffusive processes for the thermally controlled bubble are illustrated. The computation is for that of Figure 2.6.

that we first provide sufficient evidence of their validity. We present comprehensive numerical validations and scaling arguments in Appendix B for four commonly used simplifications. In this section we present the simplified sets of equations in a sequential manner, and summarize the criteria for which each of the approximations are valid. It should be reiterated that the criteria presented are specifically for applications where only the bubble dynamics are required to be accurate, and we often find that the simplifications result in maximum bubble pressures, maximum average temperatures and minimum concentrations, to only be within an order of magnitude of the results from a computation without the simplification. If we were interested in applications where these particular bubble properties were of concern (for example sonoluminescence and sonochemistry) then some of the following simplifications should not be applied.

2.4.1 Insoluble gas

As explained in Section 2.3.1, when a gas-vapor bubble expands, the gas that is dissolved in the liquid phase diffuses into the bubble and increases the mass of non-

condensible gas within the bubble. On collapse the reverse process occurs. For the typical computation presented in Section 2.3.1, the relatively fast timescales of growth and collapse, combined with the low solubility of the air in the water [$C_a = \mathcal{O}(10^{-5})$], means the overall effect on the bubble dynamics may be negligible. However, over the cycle of this particular computation there is a small net increase in the mass of gas within the bubble which may become important in situations where there are many repetitions of the cycle. This growth by rectified mass diffusion is well documented [see, for example, Plesset & Prosperetti (1977) or Brennen (1995)]. A specific example of this is a bubble subjected to a lithotripter shock wave (Matula et al. 2002). Over many cycles the equilibrium radii of the bubbles increases, which has important consequences on the cloud cavitation dynamics and ultimately stone comminution (Tanguay 2003). Another instance where the diffusion of gas in the liquid phase may be important is when the gas has a higher solubility (and/or diffusivity) in the liquid than for the air-water systems primarily considered here. A common example is carbon-dioxide ($C_a = \mathcal{O}(10^{-3})$ in water at 25°C and atmospheric pressure) with important implications in volcanic and limnic eruptions (Zhang 1996, Zhang, Sturtevant & Stolper 1997).

Nonetheless when rectified diffusion is not important, then the scaling analysis and numerical validation in Appendix B suggest that, for air bubbles in water at 25°C and atmospheric pressure, diffusion of air in the liquid can be neglected if $t_w/(ScRe)$ is small enough. This enables us to remove equation (2.4) from consideration, which is of large numerical advantage since the gas concentration in the liquid is difficult to resolve (Section 2.2). In addition, we can remove the interface conditions (2.27) and (2.30), and rewrite (2.32) for the case where $\dot{m}_a'' = 0$ as,

$$\dot{m}_v'' = \frac{D}{ScRe}\frac{\rho_w}{1 - C_w}\frac{\partial C}{\partial r}\Big|_{r=R}, \tag{2.46}$$

where the subscript w denotes a variable evaluated at the bubble wall ($r = R$). The above equation is sufficient as a boundary condition for solution of the mass diffusion

equation in the bubble interior.

The removal of diffusion of gas in the liquid results in the same set of equations as if we had originally assumed that the gas was insoluble in the liquid, and hence we term the simplification as the *insoluble gas* approximation. In fact the basis for the approximation is a combination of low gas solubility and the timescale of bubble motion being too fast for any appreciable amount of gas to diffuse from the liquid to the bubble, and vice-versa.

2.4.2 Cold liquid

The arguments in Section 2.3.2 indicate that if the liquid temperature is low enough, then the temperature changes in the liquid can be neglected, due to the small slope of the vapor saturation curve. This approximation is referred to as the *cold liquid* approximation. A more detailed analysis is presented in Appendix B, where specifically, for the bubble motions under present consideration, the numerical results suggest that for water at 25°C the impact of thermal effects on bubble dynamics is negligible. We implement the approximation by removing equation (2.5) and replacing the interface condition (2.28) with

$$\tilde{T}_w = \tilde{T}_{l_\infty} = const., \tag{2.47}$$

which implies that the liquid can transfer heat infinitely fast to the gas and latent processes. Removal of equation (2.5), when combined with the insoluble gas approximation in the previous section, removes all field equations in the liquid, which is clearly of great numerical benefit.

2.4.3 Equilibrium phase change

The rate of phase change at the bubble wall is limited by equation (2.31). However in some circumstances this finite rate of phase change may not be the limiting factor:

bubble motions may be slow enough so that the rate limit is never approached, or the phase change may be limited by the finite rate of diffusion of the vapor in the non-condensible gas near the bubble wall (Storey & Szeri 2000). In these circumstances it would be possible to assume that the vapor pressure at the bubble wall is in equilibrium with the bubble wall temperature. We can then remove equation (2.31) and substitute $\tilde{p}_v = \tilde{p}_{v_{sat}}(\tilde{T})$ into equation (2.33) and rearrange to obtain the new interface condition,

$$\rho_w C_w = \frac{\tilde{p}_{v_{sat}}(\tilde{T}_w)}{\mathcal{R}_v \tilde{T}_w}. \tag{2.48}$$

The mass flux of vapor into the bubble is then determined from the solution of the mass diffusion equation (2.12) and equation (2.46).

Analysis in the absence of non-condensible gas indicates that for α of order unity then the non-equilibrium correction is of the order of the Mach number of the bubble wall (Plesset & Prosperetti 1977). The numerical results in Appendix B do not strongly bear out this expected trend, with the error remaining small even for maximum bubble wall Mach numbers approaching unity. This is presumably because of the presence of non-condensible gas in the present computations. Importantly the numerical results demonstrate that bubble dynamics are not significantly impacted by the assumption of equilibrium phase change provided the true value of accommodation coefficient is about 0.1 or greater. However the effect of assuming equilibrium phase change on the maximum bubble pressure and minimum average concentration is fairly significant, presumably due to the role that finite rate phase change plays in trapping vapor during the fast bubble collapse (Storey & Szeri 2000).

2.4.4 Homobaricity

Many authors have assumed that the pressure field within a bubble remains spatially uniform throughout its motions. This homobarotropic assumption enables the inviscid form of the momentum equation (2.13) to be integrated and combined with the

mixture continuity equation (2.11) to yield an ordinary differential equation for the internal bubble pressure (Nigmatulin et al. 1981, Prosperetti et al. 1988). This ODE can take various forms, and we choose that derived by Ichihara et al. (2000) for a gas-vapor bubble,

$$\frac{d\tilde{p}}{dt} = \frac{-3\gamma}{R}\left[\tilde{p}V - \frac{\gamma-1}{\gamma}\frac{k_w}{PrRe}\frac{\partial\tilde{T}}{\partial r}\Big|_{r=R} - \mathcal{R}_v\tilde{T}_w\dot{m}_v''\right], \tag{2.49}$$

where the additional assumption of equal ratios of specific heats of the gas and vapor has been made ($\gamma_a \approx \gamma_v \equiv \gamma$). In the above equation the temperature gradient at the bubble wall is determined from the solution of the energy equation (2.18), which following the manipulations with the continuity and momentum equations, is written as

$$\frac{\partial\tilde{T}}{\partial t} + U\frac{\partial\tilde{T}}{\partial r} = \frac{1}{PrRe\rho c_p}\frac{1}{r^2}\frac{\partial}{\partial r}\left(kr^2\frac{\partial\tilde{T}}{\partial r}\right) + \frac{\gamma-1}{\gamma}\tilde{T}\frac{\dot{\tilde{p}}}{\tilde{p}}, \tag{2.50}$$

$$U = \frac{1}{\tilde{p}}\left[\frac{\gamma-1}{\gamma}\frac{k}{PrRe}\frac{\partial\tilde{T}}{\partial r} - \frac{r}{3\gamma}\dot{\tilde{p}}\right], \tag{2.51}$$

where the Θ term in equation (2.18) has been retained, and the viscous terms have been neglected based upon the scaling arguments of Prosperetti et al. (1988). In equation (2.49), $\dot{m}_v''$ is given in terms of the concentration gradient at the bubble wall by equation (2.46). The concentration gradient is determined from the solution of the mass diffusion equation (2.12), where the velocity field is determined from the integration of the momentum equation,

$$u = U + \frac{D}{ScRe}\frac{\mathcal{R}_v - \mathcal{R}_a}{\mathcal{R}}\frac{\partial C}{\partial r}. \tag{2.52}$$

The advantage of making the homobarotropic approximation is evident in the reduction of numerical effort due to the two partial differential equations (2.11) and (2.13)

being replaced by the single ordinary differential equation (2.49). Since equation (2.11) is no longer directly integrated, the mixture density ρ is not available for computing the primitive variable C from the integrated variable ρC. Instead we combine equations (2.14) and (2.15) to obtain

$$C = \frac{1}{\mathcal{R}_v - \mathcal{R}_a}\left[\frac{\tilde{p}}{\rho\tilde{T}} - \mathcal{R}_a\right], \tag{2.53}$$

which then enables ρ to be computed from the integrated variable ρC.

Analysis of the homobarotropic approximation indicates that the relative difference in pressure at the bubble center to pressure at the bubble wall scales with the square of the Mach number of the bubble wall (Nigmatulin et al. 1981, Prosperetti et al. 1988). Numerical results in Appendix B demonstrate that the bubble dynamics are not significantly impacted by the homobarotropic assumption even for Mach numbers approaching unity. This is consistent with the recent analysis and numerical results of Lin et al. (2002), who claim that the pressure non-uniformity within the bubble scales with the bubble wall acceleration rather than the Mach number. Their computations indicate that although there are significant pressure non-uniformities in the bubble during collapse these have little impact on the bubble dynamics, even for Mach numbers exceeding unity. Presumably the duration of the non-uniformity is so short as to not effect the bubble dynamics.

2.4.5 Summary

To summarize, for the present air-vapor bubbles in water at 25°C we can simplify the full set of equations by assuming an insoluble gas, cold liquid, equilibrium phase change and homobaricity. In this case we can solve the simpler set of equations (2.3), (2.49), (2.50) and (2.12), where the last two equations are PDEs which are furnished by the appropriate symmetry conditions (2.23) at $r = 0$ and boundary conditions (2.47) and (2.48) at $r = R$. Compared to the original set of equations this represents a substantial reduction in computational effort, since the two field equations in the

liquid have been removed, and the number of field equations in the gas have been reduced from four to two. Apart from the hot liquid computations in Sections 2.5.3 and 3.7, the computations presented in the remainder of this thesis take advantage of all these assumptions.

2.5 Data set reduction

While the plots presented in Section 2.3 are useful for illustrating diffusive processes for a typical bubble motion, it is more convenient, from a modeling perspective, to obtain a reduced data set that contains the essential features of the computation. To this end, we compute the proper orthogonal decomposition (POD) of the temperature and concentration profiles within the bubble. First we present a brief summary of the objective of POD and the method that we used to compute the POD from a full spectral computation. Results obtained from the POD are then presented for numerous computations spanning a wide parameter space. These results motivate a possible approach to a reduced-order model, that is further developed in Chapter 3. Finally the POD is applied to the liquid temperature field for the hot liquid computation that was presented in Section 2.3.2.

2.5.1 Proper orthogonal decomposition

The proper orthogonal decomposition (POD) was developed in the context of probability theory by Loève (1978), and was first used in the fluids setting by Lumley (1970) for studying turbulence. Here we present a summary of the POD in the specific context of application to the temperature and concentration fields within a bubble, with the above two references providing more general and complete descriptions of the method. In the present context, the goal of POD is given a number of realizations $\{q^k(y)\}$ of a field $q(y)$, defined in the Hilbert space $L^2[0,1]$, find the basis $\{\phi_j(y)\}_{j=1}^m$, which is optimal in the sense that the m-dimensional approximation,

$$q_m(y) = \sum_{j=1}^{m} a_j \phi_j(y), \tag{2.54}$$

describes a typical member of the ensemble $\{q^k\}$ better than the use of *any* other m-dimensional basis. More precisely, we choose the POD modes ϕ to maximize the mean projection of the function q on ϕ,

$$\max_{\phi \in L^2[0,1]} E\left(\|P_\phi q\|^2\right), \tag{2.55}$$

where $E(.)$ denotes an average over k, $\|.\|$ denotes the induced norm, and $P_\phi q$ is the projection of q onto ϕ.

In this thesis, the method used to compute the POD modes, $\phi_j(y)$, is the snapshot method developed by Sirovich (1987). The snapshot method is computationally more efficient than the classical direct method for computational data, where there are typically a large number of grid points in the domain. For the present work, where only a modest number (70) modes are used, either of the methods would be feasible. In the snapshot method the POD modes can be written as linear combinations of the instantaneous realizations, or snapshots, $q^k \equiv q(y, t_k)$. That is,

$$\phi_j(y) = \sum_{k=1}^{M} c_k q(y, t_k), \tag{2.56}$$

where in the present case q represents either of the scalar fields, T or C, and M is the number of snapshots in the ensemble. The POD modes are then determined by solving the following M-dimensional eigenvalue problem for the c_k,

$$U_{ij} c_j = \lambda c_i, \tag{2.57}$$

where $U_{ij} \equiv \frac{1}{M}\langle q^j, q^i \rangle$, and the average over k has been taken to be the simple arithmetic mean. Often the inner-product that is used to compute U_{ij} is chosen such that some physical quantity (for example energy) over the domain is minimized (Rowley 2002). In this case we choose an inner-product over which the spectral functions (the *even* Chebychev modes) are orthogonal,

$$\langle u(y), v(y) \rangle \equiv \int_0^1 \frac{u(y)v(y)}{\sqrt{1-y^2}} dy. \tag{2.58}$$

This choice simplifies the computation of U_{ij} by exploiting the fact that the snapshot data are written as expansions of the spectral functions.

It is readily demonstrated that the k^{th} eigenvalue can be written as

$$\lambda_k = E\left(\|P_{\phi_k} q\|^2\right). \tag{2.59}$$

Thus the k^{th} eigenvalue represents the fraction of "energy" that is captured by the k^{th} POD mode. A well-known method for obtaining reduced-order models is to use a Galerkin projection of the computed POD modes onto the governing PDEs, which then results in a set of ODEs for the mode amplitudes [see, for example, Rowley (2002)]. The usefulness of this method hinges on most of the energy being contained within a low number of POD modes so that a low-order system results. However, this does not necessarily guarantee success of the method. In addition, the Galerkin projection is not trivial to compute and would result in a different set of ODEs for each POD computation. This approach is rather cumbersome, since, for a given set of operating parameters, a set of POD data from a full computation at similar parameters would have to be available. Therefore, a reduced-order model based on a Galerkin projection of POD modes would not be able to be readily implemented into future and existing continuum computations.

Instead of proceeding with a Galerkin projection, we compute the POD as a means

of data set reduction. In this context, the success of the POD again hinges upon a large fraction of the energy being captured in a few modes. These few modes, which contain all the essential features of the problem, can then replace the relatively large data set of M snapshots.

2.5.2 POD results

Here we compute the POD as a means of distilling essential information from the fairly complicated computations of the previous sections, and as motivation for the reduced-order model presented in the following chapter. Since the parameter that primarily determines the diffusive behavior in the bubble interior is the Peclet number (Matsumoto & Takemura 1994), we introduce the two Peclet numbers respectively relating to heat and mass transfer in the gas,

$$Pe_g \equiv PrRe\frac{\rho_0 c_{p0}}{k_0} = \frac{\rho_0' c_{p0}'}{k_0'} R_0'^2 \omega_0', \tag{2.60}$$

$$Pe_{a-v} \equiv ScRe\frac{1}{D} = \frac{R_0'^2 \omega_0'}{D'}. \tag{2.61}$$

Figure 2.9 shows the first three POD modes for the temperature fields (concentration looks similar) for four typical computations with different values of Pe_g. The number of snapshots used in the POD, as well as the time period over which the snapshots were taken, are given for each computation in Table A.3. Slightly changing the sample of snapshots was found to have negligible impact on the POD results. For the lowest two values of Pe_g the POD modes show significant variation over the entire range of y, indicating that the diffusion penetration length is of the same order as, or greater than, the bubble radius. In particular, the first POD mode is well approximated by a quadratic in y, which corresponds to the solution of the diffusion equations in the limit of $Pe_g \to 0$ (see Section 3.4). For values of Pe_g lower than this, the POD modes remain essentially unchanged. As Pe_g is increased the POD modes show less variation near the bubble center. Indeed, for $Pe_g = 3475$ in (d), most of

the variation in the POD modes is restricted to near the bubble wall, which indicates the diffusion penetration length is significantly smaller than the bubble radius. The manner in which the POD mode shapes depend upon Pe_g are consistent with the full computations of Matsumoto & Takemura (1994). Here the POD analysis provides a convenient and concise means of summarizing such full computations.

The plots of POD mode shapes on their own are of limited use without knowledge of the fraction of energy that is contained in each mode. As mentioned in the previous section, the eigenvalue, λ_k, from the POD analysis indicates the amount of energy contained in the associated POD mode, ϕ_k. Figure 2.10(a) plots the first five eigenvalues from POD analysis of the temperature field for different values of Pe_g. The eigenvalues are normalized such that they sum to unity. For $Pe_g = 5.27$ the decay in the eigenvalues with mode number, k, is extremely rapid, with the second eigenvalue being about six orders of magnitude lower than the first. As the value of Pe_g is increased, this decay becomes more gradual with the second eigenvalue being only about one order of magnitude lower than the first for $Pe_g = 349$. The trend appears to reverse with higher Pe_g, with the decay in eigenvalues for $Pe_g = 3475$ being more rapid than for $Pe_g = 349$. This is however due to the maximum bubble radius, R_{max}, being lower ($R_{max} = 1.22$ compared to 2.4) for the computation at highest Pe_g. This lower value of R_{max} is necessary due to limitations of the full computation, where, at high values of Pe_g, the resolving of the steep gradients within the bubble becomes prohibitive for larger bubble growths.

Figure 2.10(b) plots the first five eigenvalues from POD analysis of the concentration field for computations with different R_{max} and fixed Pe_{a-v}. Clearly the rate of decay of the eigenvalues decreases as R_{max} is increased. It is apparent from these plots that modeling the diffusive behavior is likely to be more difficult for high values of Pe_g, Pe_{a-v} and R_{max}, since more degrees of freedom will be needed in the model to capture the additional energy contained in the higher modes.

Nonetheless, in all cases studied, more than about 90% of the energy is contained in the first POD mode. This leads to the conclusion that a reasonable reduced-order model may be able to be based solely on the first POD mode. However, using only

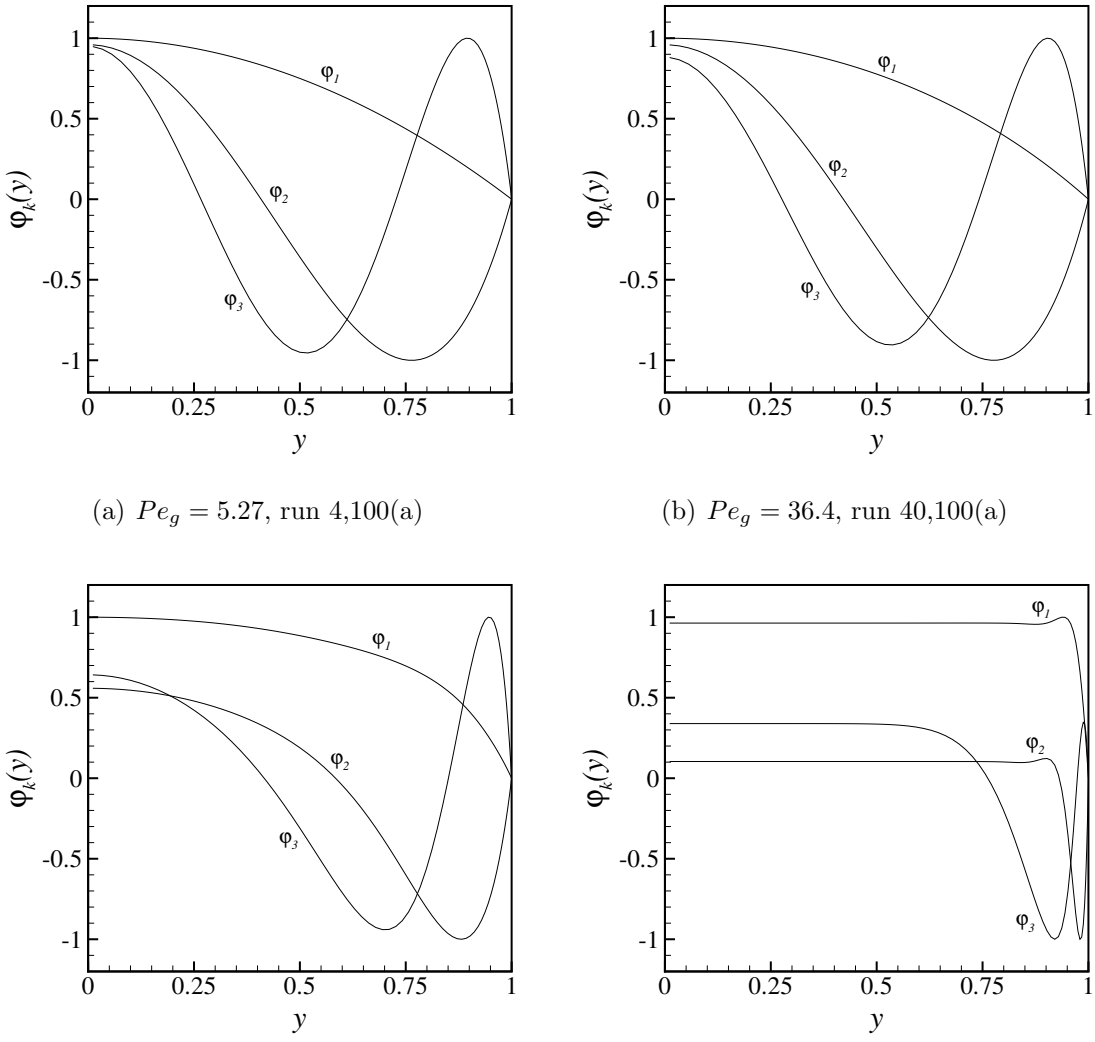

(a) $Pe_g = 5.27$, run 4,100(a)

(b) $Pe_g = 36.4$, run 40,100(a)

(c) $Pe_g = 349$, run 400,100(b)

(d) $Pe_g = 3475$, run 4000,100(a)

Figure 2.9: First three mode shapes from POD analysis of temperature field for for different values of Pe_g. The profiles show variation over the entire bubble interior for low values of Pe_g, while for high values of Pe_g the variation is limited to near the bubble wall.

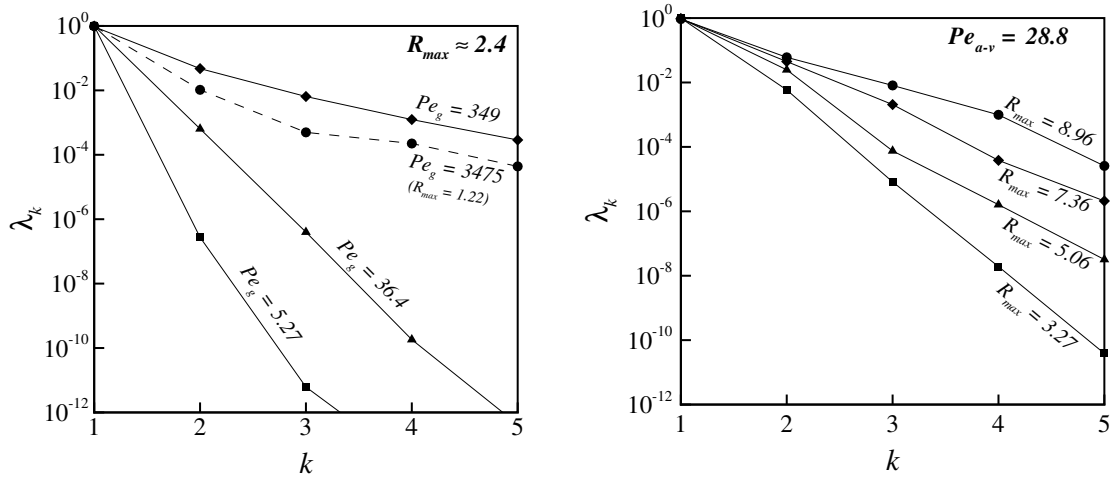

(a) Varying Pe_g (b) Varying R_{max}

Figure 2.10: First five normalized eigenvalues from POD analysis for different values of (a) Peclet number (Pe_g) and (b) maximum bubble radius (R_{max}). The eigenvalues decay rapidly with mode number, k. The decay is most rapid for low values of Pe_g and R_{max}.

one mode is equivalent to using a constant (average) transfer coefficient, which may be computed from the first POD mode directly as

$$\beta \equiv \frac{-\partial\phi_1/\partial y|_{y=1}}{\bar{\phi}_1 - \phi_{1_w}}. \tag{2.62}$$

Here, ϕ_1 denotes the first POD mode, the subscript w denotes the value at the bubble wall, and the over-bar is the volume average defined by

$$\bar{f} \equiv \frac{1}{V}\int_V f dV = 3\int_0^1 f(y)y^2 dy. \tag{2.63}$$

The heat and mass transfer coefficients (β_T and β_C), as well as the fractions of energy *not* captured by the first POD mode ($1 - \lambda_{1_T}$ and $1 - \lambda_{1_C}$), are computed from the first POD mode for many full computations covering a wide range of Peclet numbers and forcing parameters. The results of the individual computations are listed in Table A.3. Results that are statistically averaged for each value of Peclet number

are given in Tables 2.1 and 2.2. It is apparent that the value of transfer coefficient increases with increasing Peclet number, which is expected given the trends in the first POD mode shape in Figure 2.9. In addition, as previously illustrated for the single POD results in Figure 2.10(a), the fraction of energy not captured by the first POD mode increases with Peclet number. An exception is for the highest value of Peclet number, which shows a larger fraction of energy to be contained by the first mode. This is again because of these computations being restricted to low values of R_{max} as discussed previously.

Pe_g	β_T	$1-\lambda_{1_T}$	σ_{n-1}
2.87	5.05	0.647%	0.311
5.27	5.23	0.547%	0.289
36.4	6.07	2.08%	0.834
349	11.8	4.18%	2.18
3475	43.5	1.12%	0.915

Table 2.1: POD average results for temperature.

Pe_{a-v}	β_C	$1-\lambda_{1_C}$	σ_{n-1}
0.691	5.04	0.018%	0.016
3.17	5.15	0.348%	0.118
28.8	4.78	2.788%	0.684
284	14.2	4.975%	1.130
2841	44.7	0.892%	0.462

Table 2.2: POD average results for concentration.

Also presented in Tables 2.1 and 2.2 are the sample standard deviations, σ_{n-1}, from the statistical averaging of the transfer coefficients. It is interesting to note that this quantity closely follows the fraction of energy not captured by the first POD mode. This again indicates that the use of constant transfer coefficients is most accurate for low Peclet numbers, when most of the energy is captured by the first mode.

The results of the POD, summarized concisely in Tables 2.1 and 2.2, motivates the development of the reduced-order model presented in Chapter 3.

2.5.3 POD applied to *hot* liquids

The POD can also be applied to the fields that are external to the bubble. Figure 2.11 presents the first three mode shapes and the first five eigenvalues for a POD analysis of the temperature field for the computation of Figure 2.6. Since this computation is for a bubble in a hot liquid where the liquid temperature field is important, we use the most complete set of equations that includes both temperature and concentration in the liquid (although the latter has negligible effect on the bubble response). The shape of the first mode is a simple, almost monotonic, decay from the wall value ($x = 1$) to zero in the far field ($x = 0$). Again the eigenvalues decay quite rapidly with mode number, with more than 90% of the energy being captured by the first mode. Motivated by this we define a liquid heat transfer coefficient based upon the first mode as

$$\begin{aligned} \beta_{T_l} &\equiv \frac{-\partial\phi_1/\partial y|_{y=1}}{\phi_1|_{y=1} - \phi_1|_{y\to\infty}} \\ &= \frac{1}{l_T\phi_1}\frac{\partial\phi_1}{\partial x}\Big|_{x=1}, \end{aligned} \tag{2.64}$$

where we have used the fact that $\phi_1|_{y\to\infty} = \phi_1|_{x=0} = 0$. For the first mode presented in Figure 2.11(a) we obtain

$$\beta_{T_l} = 5.7. \tag{2.65}$$

This result is used in Section 3.7 to extend the reduced-order model of Chapter 3 to include effects due to variations in the liquid temperature.

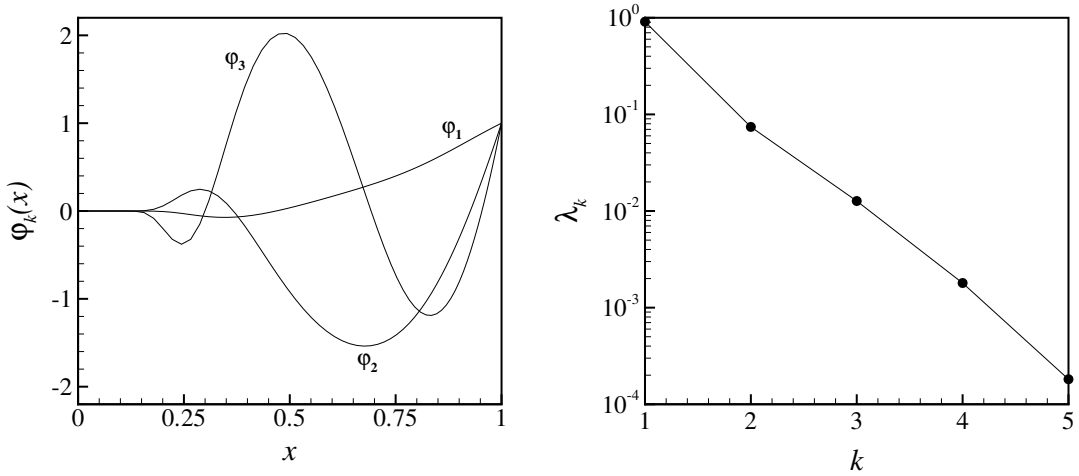

(a) POD modes

(b) Eigenvalues from POD

Figure 2.11: First three POD modes and first five normalized eigenvalues from POD analysis of the liquid temperature field for the computation of Figure 2.6. The first POD mode shape is almost monotonic. Most of the energy is captured by this mode, as indicated by the rapid decay of the eigenvalues.

Chapter 3

Constant transfer coefficient model

This chapter develops a reduced-order model of the diffusive processes for the interior of gas-vapor bubbles in a cold liquid. Motivated by the POD results of the previous chapter, we use constant transfer coefficients to estimate the heat and mass flux at the bubble wall. The model is computationally efficient with only two additional ODEs required to model the diffusive effects. We present linear analysis of the internal diffusion equations to provide a means for determining appropriate values of the transfer coefficients, based upon a characteristic timescale of bubble motion. The model equations are shown to agree with the full equations in the limit of low Peclet numbers. The radial dynamics obtained by the constant transfer model demonstrate better agreement of full bubble computations than other existing reduced-order models. Finally we extend the model to relax the cold liquid assumption.

3.1 Modeling the fluxes: the basis for the model

We presently focus our modeling efforts on the situations where we can assume an insoluble gas, cold liquid, equilibrium phase change and homobaricity. For these assumptions the equations describing a single bubble with heat and mass transfer were developed in Section 2.4. For convenience some of these are rewritten below, in terms of p and T, for an inviscid gas,

$$\tilde{p}_0\left[p - p_\infty(t)\right] = R\dot{V} + \frac{3}{2}V^2 + \frac{4}{Re}\frac{V}{R} + \frac{2}{WeR}, \tag{3.1}$$

$$\dot{R} = V, \tag{3.2}$$

$$\frac{dp}{dt} = \frac{-3\gamma}{R}\left[pV - \frac{1}{Pe_g}\frac{1}{R}\tilde{k}_w\frac{\partial T}{\partial y}\Big|_{y=1} - \frac{\tilde{T}_0}{\tilde{p}_0}\mathcal{R}_v T_w \dot{m}_v''\right], \tag{3.3}$$

$$\dot{m}_v'' = \frac{1}{Pe_{a-v}}\frac{\tilde{p}_0}{\tilde{T}_0}\frac{p}{\mathcal{R}_w T_w}\frac{1}{1-C_w}\frac{1}{R}\frac{\partial C}{\partial y}\Big|_{y=1}. \tag{3.4}$$

In the above equations we have used the radial coordinate that fixes the bubble wall, $y \equiv r/R(t)$, and subscript w denotes a variable evaluated at the bubble wall ($y = 1$). We have used the following property for a perfect gas, $\rho' c_p' = \frac{\gamma}{\gamma-1}\frac{p'}{T'}$, and have rewritten $PrRe$ and $ScRe$ in terms of the Peclet numbers, Pe_g and Pe_{a-v} (defined in Section 2.5.2). Recall that $\tilde{p}_0$ and $\tilde{T}_0$ are the initial bubble pressure and temperature under the alternative non-dimensionalization. In addition we define a new non-dimensional thermal conductivity of the gas, $\tilde{k} \equiv k/k_0 = k'/k_0'$, where k_0 and k_0' are the non-dimensional and dimensional initial values of thermal conductivity. Recall that we do not allow k to vary with temperature, but it will change throughout the bubble as the vapor concentration, C, changes.

To close the set of equations (3.1) to (3.4) we require the solution of the radial diffusion equations (2.12) and (2.50) to obtain the concentration and temperature gradients at the bubble wall. However the numerical integration of these two PDEs is very time consuming compared to the integration of the ODEs above. The goal of the present modeling is to reduce each of these PDEs to a few ODEs that are still able to capture the important features of the full equations. Motivated by the POD results of Section 2.5.2, we model the gradients at the bubble wall using constant mass and heat transfer coefficients, β_C and β_T, such that

$$\frac{\partial C}{\partial y}\Big|_{y=1} \approx -\beta_C\left(\bar{C} - C_w\right), \tag{3.5}$$

$$\frac{\partial T}{\partial y}\Big|_{y=1} \approx -\beta_T\left(\bar{T} - T_w\right). \tag{3.6}$$

Here the over-bar denotes the volume average over the bubble defined by equation (2.63). For each computation the transfer coefficients are a function of the Peclet numbers (see Tables 2.1 and 2.2). We presently assume them to be given, either from a POD analysis of an appropriate full computation, or from more complete versions of Tables 2.1 and 2.2. Due to the use of constant transfer coefficients, we call the present model the *constant transfer* model.

The only quantities remaining to be determined are the temperature and concentration at the bubble wall, and the volume averages of the temperature and concentration. For the present case of a cold liquid the wall temperature is simply given by equation (2.47) which is rewritten here,

$$T_w = T_{l_\infty}, \tag{3.7}$$

while the wall concentration is determined from the equilibrium condition (2.48) combined with equations (2.14) and (2.15),

$$C_w = \frac{1}{1+\theta} \tag{3.8}$$

$$\theta = \frac{\mathcal{R}_v}{\mathcal{R}_a}\left[\frac{p}{p_{v_{sat}}(T_w)} - 1\right]. \tag{3.9}$$

Note that the form of equation (3.8) ensures that $C_w \in [0,1]$. The average bubble temperature is estimated by applying the perfect gas law in a volume averaged sense to the bubble contents,

$$\frac{\bar{T}}{T_0} \approx \frac{p\rho_0}{p_0\bar{\rho}}, \tag{3.10}$$

$$\approx \frac{p}{p_0}\frac{R^3}{R_0^3}\frac{m_{a_0}+m_{v_0}}{m_{a_0}+m_v}, \tag{3.11}$$

where m_{a_0} and m_{v_0} are the initial masses of non-condensible gas and vapor in the

bubble, and $R_0 = p_0 = T_0 = 1$ has been written for clarity. Results from full computations indicate that this approximation is extremely accurate. The mass of vapor in the bubble, m_v, is determined by integrating

$$\frac{dm_v}{dt} = 4\pi R^2 \dot{m}_v'', \tag{3.12}$$

where $\dot{m}_v''$ is given by equation (3.4). The average vapor concentration is simply approximated by

$$\bar{C} \approx \frac{m_v}{m_{a_0} + m_v}. \tag{3.13}$$

The set of model equations (3.1) through (3.13) are now closed as long as we have an estimate for the transfer coefficients. As mentioned previously, the transfer coefficients depend upon the Peclet numbers, and can be determined from POD analysis. It is preferable for the reduced-order model not to rely on POD analysis, since in general one may not have access to an appropriate full computation. In the next section we appeal to some results from linear analysis to develop a simple method for determining the transfer coefficients as functions of Peclet numbers.

3.2 Linear analysis

The mass and heat diffusion equations (2.12) and (2.50) are rewritten in terms of T, Pe_g and Pe_{a-v}, and are linearized for small amplitudes (denoted by primes),

$$\frac{\partial C'}{\partial t} = \frac{1}{Pe_{a-v}} \frac{1}{y^2} \frac{\partial}{\partial y} \left(y^2 \frac{\partial C'}{\partial y} \right), \tag{3.14}$$

$$\frac{\partial T'}{\partial t} = \frac{1}{Pe_g} \frac{1}{y^2} \frac{\partial}{\partial y} \left(y^2 \frac{\partial T'}{\partial y} \right) + \frac{\gamma - 1}{\gamma} p', \tag{3.15}$$

These PDEs are furnished by the symmetry conditions, $\frac{\partial C'}{\partial y}|_{y=0} = \frac{\partial T'}{\partial y}|_{y=0} = 0$, and boundary conditions, $C'|_{y=1} = C'_w(t)$ and $T'|_{y=1} = 0$. The solution to the linearized system can be written in the frequency domain as

$$\hat{C}'(y,\omega) = \hat{C}'_w(\omega)\,\Theta(y,\omega;Pe_g), \tag{3.16}$$

$$\hat{T}'(y,\omega) = \frac{\gamma-1}{\gamma}\hat{p}'(\omega)\left[1-\Theta(y,\omega;Pe_{a-v})\right], \tag{3.17}$$

where the complex linear mode shape $\Theta(y,\omega;Pe)$ is given by

$$\Theta(y,\omega;Pe) = \frac{\sinh\sqrt{i\omega Pe}y}{y\sinh\sqrt{i\omega Pe}}. \tag{3.18}$$

Differentiating and volume averaging of equations (3.16) and (3.17) enable us to write

$$\left.\frac{\partial\hat{C}'}{\partial y}\right|_{y=1}(\omega) = -\Psi(\omega;Pe_{a-v})\,\hat{\bar{C}}'(\omega), \tag{3.19}$$

$$\left.\frac{\partial\hat{T}'}{\partial y}\right|_{y=1}(\omega) = -\Psi(\omega;Pe_g)\,\hat{\bar{T}}'(\omega), \tag{3.20}$$

where the transfer function $\Psi(\omega;Pe)$ is given explicitly as

$$\Psi(\omega;Pe) = \left\{\left[\sqrt{i\omega Pe}\coth\sqrt{i\omega Pe}-1\right]^{-1} - \frac{3}{i\omega Pe}\right\}^{-1}. \tag{3.21}$$

Since the transfer function depends upon ω the transforming of equations (3.19) and (3.20) back into the time domain would generally result in a convolution integral, which is of little use for obtaining estimates for the transfer coefficients, and difficult to evaluate numerically. In addition, the inverse transform of $\Psi(\omega;Pe)$ does not exist.

These difficulties are overcome by approximating the transfer function in the frequency domain, such that equations (3.19) and (3.20) can be inverted analytically

without resulting in a convolution integral. In order to obtain real valued quantities upon transforming into the time domain, we require the following property to hold for the approximation,

$$\Psi_{approx}(\omega^*; Pe) = \Psi^*_{approx}(\omega; Pe), \tag{3.22}$$

where ω^* denotes the complex conjugate of ω. In the constant transfer model we simply use the zeroth-order term of a Taylor series about some characteristic frequency, ω_0. The use of more sophisticated rational function approximations are explored in Appendix C, but are ultimately found to give less accurate results. The characteristic frequency that we choose is the isothermal bubble natural frequency which under the present non-dimensionalization simply corresponds to setting $\omega = \omega_0 = 1$ in equation (3.21). The appropriateness of the choice of the isothermal bubble natural frequency is further explored in Section 3.3. Equations (3.19) and (3.20) are transformed back into the time domain to obtain

$$\left.\frac{\partial C}{\partial y}\right|_{y=1} = -\Re\{\Psi\left(Pe_{a-v}\right)\}\left[\bar{C} - C_w\right], \tag{3.23}$$

$$\left.\frac{\partial T}{\partial y}\right|_{y=1} = -\Re\{\Psi\left(Pe_{g}\right)\}\left[\bar{T} - T_w\right], \tag{3.24}$$

where the imaginary part of the transfer function, $\Im\{\Psi(Pe)\}$, has necessarily been neglected in order to satisfy equation (3.22). In the above equations the frequency independent transfer function is defined as $\Psi(Pe) \equiv \Psi(1; Pe)$, and the linear perturbations have been written in terms of the original variables.

Comparing the above equations to the approximations (3.5) and (3.6) it is apparent that the transfer coefficients are given by

$$\beta_C \equiv \Re\{\Psi(Pe_{a-v})\}, \tag{3.25}$$

$$\beta_T \equiv \Re\{\Psi(Pe_g)\}. \tag{3.26}$$

$$\tag{3.27}$$

These final two equations close the set of model equations presented in Section 3.1 without the need for any POD analysis. In Section 3.5 we will test the reduced-order model by comparison to full computations. In the remainder of this section we explore some of the consequences of evaluating the transfer function at a single frequency and neglecting the imaginary part of the transfer function.

Figure 3.1 plots the real part, β, and phase θ, of the transfer function as the Peclet number is varied over many orders of magnitude. We see in the limit $Pe \ll 1$, which corresponds to nearly isothermal (and nearly uniform concentration) behavior, that $\beta \to 5$ and $\theta \to 0$. So for this case the transfer function *is* constant *and* real valued, and the transformations from frequency domain to time domain can be carried out exactly. Hence, for linear perturbations the model equations will become exact as Pe_g and $Pe_{a-v} \to 0$. It will be demonstrated in Section 3.4 that this property will also hold in the more general non-linear case.

Away from the low Peclet number limit we chose a single frequency at which to evaluate the transfer function in order to avoid a convolution integral on transformation back into the time domain. Obviously during a general bubble motion there are more than one timescale, so the best we can do is to choose the dominant one. Section 3.3 demonstrates that the bubble natural frequency is a good representation of the dominant frequency; the model can therefore be expected to give the best results possible within the current framework.

The imaginary part of the transfer function is also neglected after the transformation into the time domain. In the linear scenario the non-zero imaginary part is interpreted as a phase difference between the gradient and average value, which is immediately apparent if we express equations (3.19) and (3.20) parametrically in $\phi \in [0, 2\pi]$,

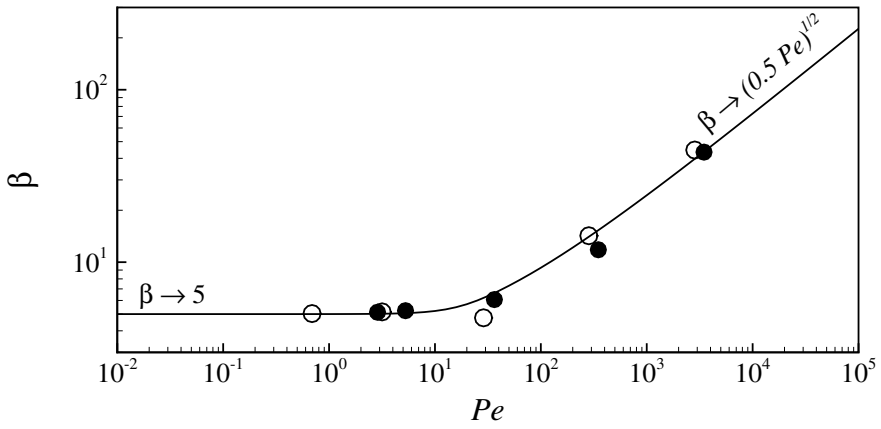

(a) Real part

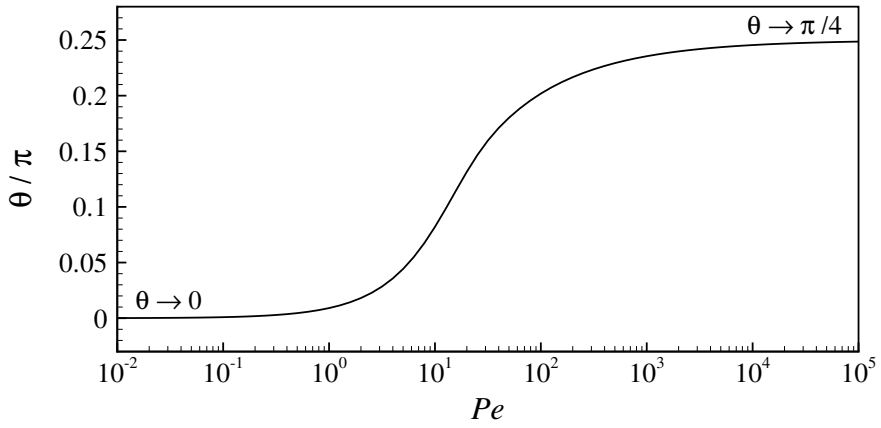

(b) Phase

Figure 3.1: Real part and phase of transfer function from linear analysis and β from POD analysis: —— Linear analysis; ● POD results from temperature fields; ○ POD results from concentration fields.

$$\left.\frac{\partial X'}{\partial y}\right|_{y=1} = -\epsilon|\Psi|\cos[\phi+\theta], \tag{3.28}$$

$$\bar{X}' = \epsilon\cos[\phi]. \tag{3.29}$$

In the above equations X is either C or T, ϵ is the steady-state linear amplitude of oscillation, and $|\Psi|$ and θ depend upon the Peclet number. Figure 3.2 plots the relation for a range of Peclet numbers. It is clear for $Pe \ll 1$ that the quantities are in phase, and during each cycle the transfer coefficients are positive constants. For increasing values of Pe there is an increasing phase difference leading to thicker and thicker cycle loops which results in negative transfer coefficients during some part of the cycle. This is consistent with observations from the full non-linear computations in Section 2.3.1. It is immediately apparent that the neglect of the phase difference, which is a direct consequence of using approximations (3.5) and (3.6), will preclude the model equations from being able to accurately replicate the complicated behavior of the temperature field that is observed in full computations.

Even though the constant transfer model, with the neglect of the phase difference, is unable to capture parts of the cycle where the transfer coefficients are negative, the POD results in Section 2.5.2 indicate that this particular detail is not of major importance since the vast majority of the energy is captured in the first POD mode. The POD results are used to further validate the use of the linear analysis in the determination of the transfer coefficients by superposing the values of β_T and β_C determined from POD analysis of full computations on the upper plot of Figure 3.1. Each of the data points represents an average of many computations at the given Peclet number (see Tables 2.1 and 2.2). We see that the data points follow the trend predicted by the linear analysis quite closely, indicating that linear analysis is a good means of determining the transfer coefficients in the absence of POD data.

We end this section by mentioning the rational function approximation to the transfer function that is discussed fully in Appendix C. The model equations that result from this more sophisticated approximation do not have the limitations that

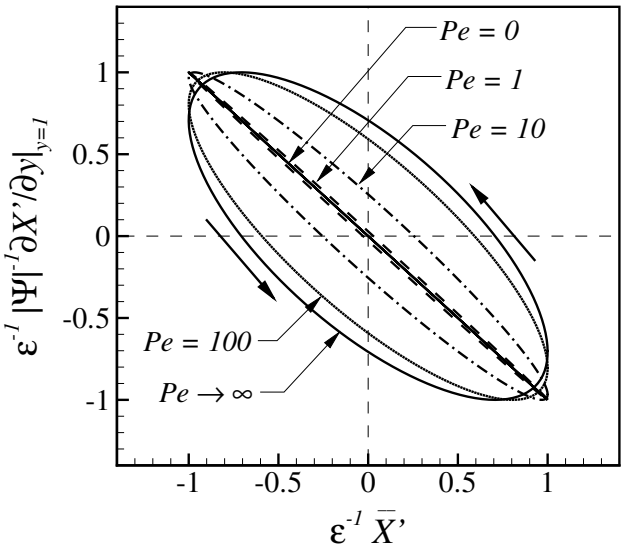

Figure 3.2: Gradient at bubble wall versus average of either temperature or concentration fields from linear analysis. For low Pe the relationship reduces to a straight line indicating the quantities are in phase, while for increasing values of Pe there is an increasing phase difference leading to thicker and thicker cycle loops.

the constant transfer model has. That is, the rational approximation model is not tuned for a single frequency, and it is able to capture the phase difference. While this model works extremely well for the linear amplitudes that the theory is based upon, it does not capture the non-linear bubble dynamics as accurately as the constant transfer model. Comparisons of the two models are made in the appendix.

3.3 Characteristic timescale

In the previous section the frequency, ω, in the transfer function given by equation (3.21) was set to a constant (unity) to avoid the convolution integral on transformation back into the time domain. Under the constant transfer model framework, where the gradients at the bubble wall are approximated by (3.5) and (3.6), the restriction to a single frequency is necessary and is an approximation when $Pe \not\ll 1$. The best that can be done is to select a single frequency that is likely to be most dominant for a general bubble motion. For a bubble forced with a spectrum of fre-

quencies the amplitude of the frequency response curve will be peaked at the bubble natural frequency, so it is reasonable to assume that the bubble natural frequency is the dominant frequency. Under the present non-dimensionalization this corresponds to setting $\omega = 1$. For larger bubbles, the polytropic natural frequency should be used rather than the isothermal one. In the upper limit this would result in the adiabatic natural frequency being approximately a factor $\gamma^{1/2}$ higher than the isothermal one. For air ($\gamma = 1.4$) this is a difference of less than 20% which is insignificant in comparison to other approximations already made, so for simplicity we use the isothermal natural frequency.

We now present some analysis to further justify the choice of bubble natural frequency in the specific setting of bubbles being forced with a negative Gaussian pressure pulse. Figure 3.3 plots the time variation of the bubble radius as computed by the homobarotropic computation (Section 2.4.4) for two forcings of different timescales; (a) shows the response to a very narrow, high amplitude pulse, while (b) shows the response to a broad, low amplitude pulse. The pulses have been chosen such that they both result in approximately the same maximum bubble growth. For the upper plot, where the forcing timescale is less than the bubble natural frequency ($t_w < 1$), the bubble response is independent of the forcing timescale. The fast forcing simply causes the bubble to grow and then bubble dynamics results in a series of collapses and rebounds on a timescale t_{R_m}. This timescale can be estimated by noting that $p_\infty(t) = p_\infty(0) = const.$ during the collapses and rebounds, which enables the analysis of Rayleigh to be applied. Indeed the time to collapse from the local maximum radius, R_m, to the point of minimum radius is approximately given by the well known Rayleigh collapse time (Brennen 1995), written here in non-dimensional units,

$$\begin{aligned} t_c &= 0.915 R_m \sigma^{-1/2} \\ &\approx 1.58 R_m. \end{aligned} \tag{3.30}$$

Here we have neglected surface tension effects ($We \gg 1$) in equation (2.10) to estimate

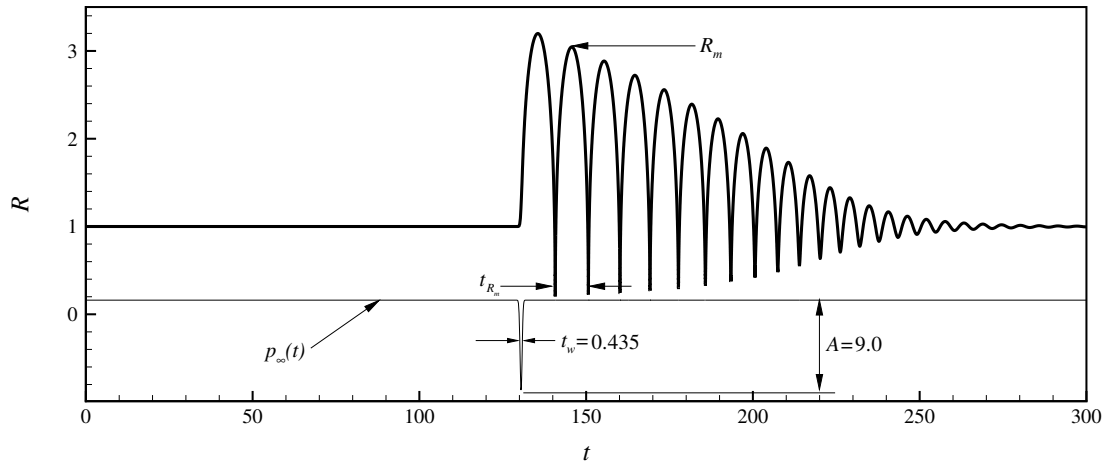

(a) Narrow, high amplitude pulse. Run 4,1(H).

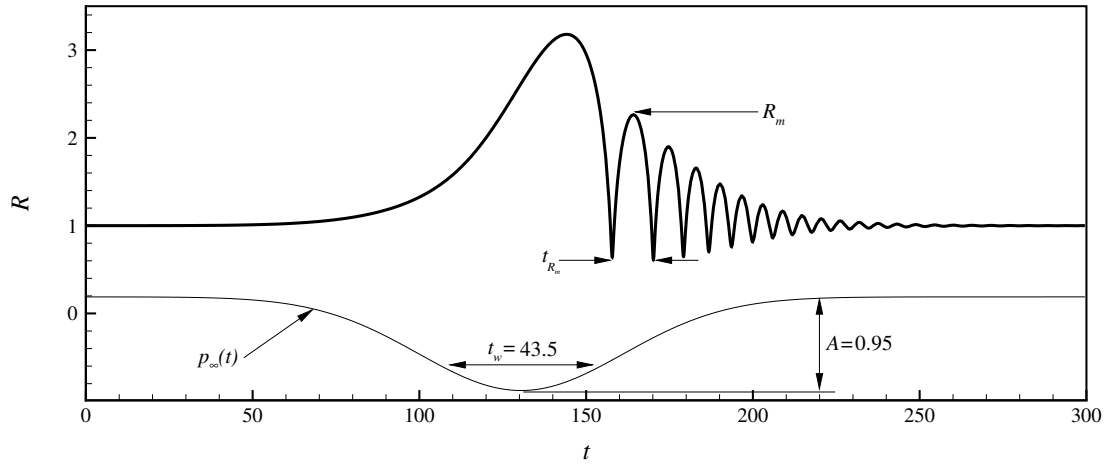

(b) Broad, low amplitude pulse. Run 40,100(a).

Figure 3.3: Time variation of bubble radius computed by homobarotropic computation for two different pulses. Conditions for each computation are identical except for the pulse characteristics. The narrow, high amplitude pulse in (a) illustrates a bubble response with a single timescale that is independent of the pulse. The broad, low amplitude pulse in (b) results in a bubble response with two timescales, one of which follows the timescale of the pulse.

$\sigma \approx \frac{1}{3}$, in order to make the last approximation. Strictly speaking this is the time of collapse of a spherical vapor cavity with zero gas content and no surface tension in an inviscid liquid, but these additional effects can be neglected on the basis that they only become important during a very brief moment in the final stage of collapse when the bubble radius is small. By symmetry of collapses and rebounds in Figure 3.3(a) it follows that a reasonable estimate for the timescale for rebounds is simply twice the Rayleigh collapse time, so that,

$$t_{R_m} \approx 3R_m, \tag{3.31}$$

$$\Rightarrow t_{R_m} = \mathcal{O}(1), \tag{3.32}$$

$$\Rightarrow 1/t'_{R_m} = \mathcal{O}(\omega'_0), \tag{3.33}$$

where in the last two equations it has been assumed that the bubble growth is relatively moderate. In certain applications where large bubble growth is encountered [for example, lithotripsy where bubble may grow 2 or 3 orders of magnitude larger than their initial size (Matula et al. 2002)] this approximation could not be justified. However, in the present case of moderate growth equation (3.33) demonstrates that the dominant frequency of bubble rebounds (given by the inverse of the characteristic time for bubble rebounds) scales with the bubble natural frequency.

The particular example in Figure 3.3(a) has a single characteristic timescale for bubble motion that is independent of the forcing timescale, t_w. By contrast, the situation in Figure 3.3(b) has a forcing timescale that is far greater than the bubble natural frequency ($t_w \gg 1$). The initial bubble growth occurs on the same timescale as the forcing, because the bubble is nearly in quasiequilibrium with the forcing pressure. After the initial growth the bubble undergoes collapses and rebounds on approximately the same timescale as in the previous case. Strictly speaking the Rayleigh analysis does not apply to the situation in Figure 3.3(b) because the far field pressure $p_\infty(t)$ is no longer constant during the collapses and rebounds, but we will assume that it is still a reasonable approximation for this and similar situations.

For this situation there are now two important timescales for the bubble motion; the forcing timescale and the timescale of the bubble collapses and rebounds. It is not immediately clear which of the timescales is more appropriate for determining the transfer coefficients for the model. Comparisons of model computations based upon both timescales are now used to justify the use of the bubble natural frequency in these circumstances.

Figure 3.4 plots the bubble radius as a function of time for the full computations, the constant transfer model based upon bubble natural frequency ($\omega = 1$) and the constant transfer model based upon inverse of forcing width ($\omega = 1/t_w$). The transfer coefficients for the model based upon $\omega = 1/t_w$ are determined by defining a new Peclet number, $Pe^{t_w} \equiv Pe/t_w$, and then computing $\beta = \Re\{\Psi(Pe^{t_w})\}$. On the gross scale [3.4(a)] the two model computations both appear to have good agreement with the full computation, although the bubble rebounds are slightly over damped. The closeup of the initial growth and subsequent two rebounds [3.4(b)] highlights the slight differences between the three computations. As might be anticipated the initial growth is most accurately predicted by the $\omega = 1/t_w$ model. Using $\omega = 1$ gives transfer coefficients that are too high, and which slightly overestimate bubble growth. By contrast, the attenuation of the rebounds is more accurately predicted by $\omega = 1$, since the timescale for this part of the computation is clearly of the order of the Rayleigh collapse time. Meanwhile, the smaller transfer coefficients with the $\omega = 1/t_w$ model results in over damped rebounds.

These results can be expressed in an alternative manner by plotting the temperature and concentration gradients versus the difference between the average and wall values of the temperature and concentration respectively (Figure 3.5). The curves for the two models are straight lines with slope equal to (the negative of) the transfer coefficient. It is interesting to note that neither of the models accurately estimate the large negative temperature gradients that occur during collapse, but this does not substantially impact the accuracy of the bubble dynamics. This is because the part of the cycle during which there are large negative temperature gradients is short; the bubble spends most of its time near the origin of Figure 3.5(a). During the brief

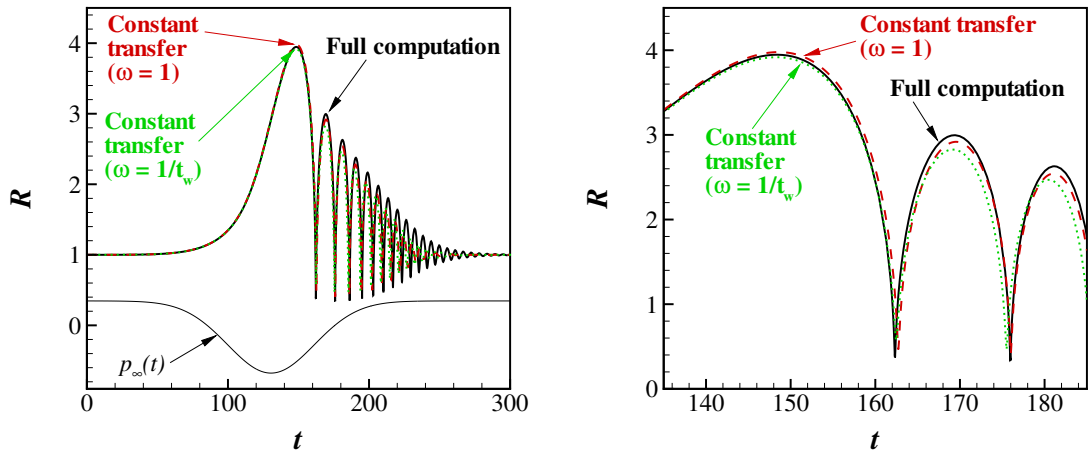

(a) Gross scale

(b) Closeup

Figure 3.4: Bubble radius computed with the full computation, and the constant transfer model based upon $\omega = 1$ ($\beta_T = 6.62$, $\beta_C = 6.21$) and $\omega = 1/t_w$ ($t_w = 43.5$, $\beta_T = \beta_C = 5.00$). The $\omega = 1/t_w$ model shows better agreement to the full computation for the initial expansion, while the $\omega = 1$ model shows better agreement of the attenuation of bubble rebounds. [Run 40,100(d).]

time of large negative gradients the bubble radius is very small, so that the surface area over which the heat flux is acting is small. It seems that it is most important to accurately model the heat transfer for the slow parts of the cycle when the bubble radius is large.

The plot of concentration in Figure 3.5(b) indicates that the $\omega = 1$ model more accurately matches the slope of the loops of the full computation than the model based upon $\omega = 1/t_w$. Hence the attenuation of the bubble rebounds are more closely matched when the constant transfer model is based upon the bubble natural frequency. However, Figure 3.5(b) indicates that perhaps an even steeper curve (that is a higher mass transfer coefficient) would achieve a better match and this may result in a more accurate model prediction of the rebounds in Figure 3.4.

Although in Figure 3.4(b) the constant transfer model based upon $\omega = 1$ is probably superior to the one based upon $\omega = 1/t_w$, the differences between the two are very slight. Figure 3.6 plots similar curves for the case where the forcing timescale is ten times that of Figure 3.4 and the differences between the models are further accen-

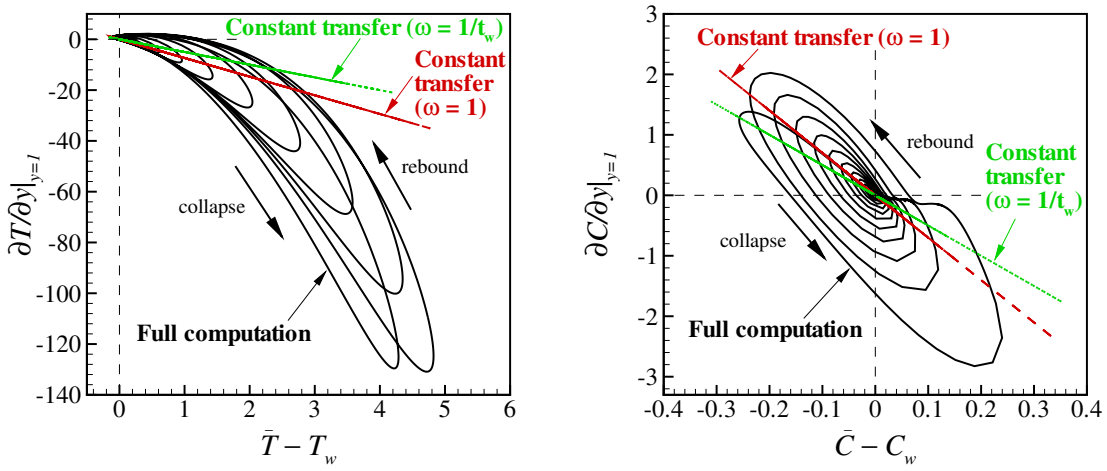

(a) Temperature (b) Concentration

Figure 3.5: Heat and mass transfer computed with the full computation, and the constant transfer model based upon $\omega = 1$ ($\beta_T = 6.62$, $\beta_C = 6.21$) and $\omega = 1/t_w$ ($t_w = 43.5$, $\beta_T = \beta_C = 5.00$). The steeper slope of the line for the $\omega = 1$ model shows better agreement to the full computation than the $\omega = 1/t_w$ model. The constant transfer model is not able to capture the phase lag effect that is present in the full computation, but this does not have a great impact on the radial bubble dynamics. Conditions as for Figure 3.4.

tuated. It is apparent that the error in the initial growth has increased substantially for the $\omega = 1$ model as has the error in the attenuation for the model based upon $\omega = 1/t_w$.

The choice of which model is most appropriate probably depends upon whether the maximum bubble growth or the attenuation of bubble rebounds is most important in the particular application. However, in general applications the timescale of the forcing may not be known a priori. In order to enable an unbiased assessment of the model we shall use the bubble natural frequency to compute the transfer coefficients for the model in the remainder of the thesis.

3.4 Analysis in the limit of small Peclet number

We now derive analytical solutions to the heat and mass diffusion equations based upon series expansions of T and C in the Peclet numbers. The constant transfer

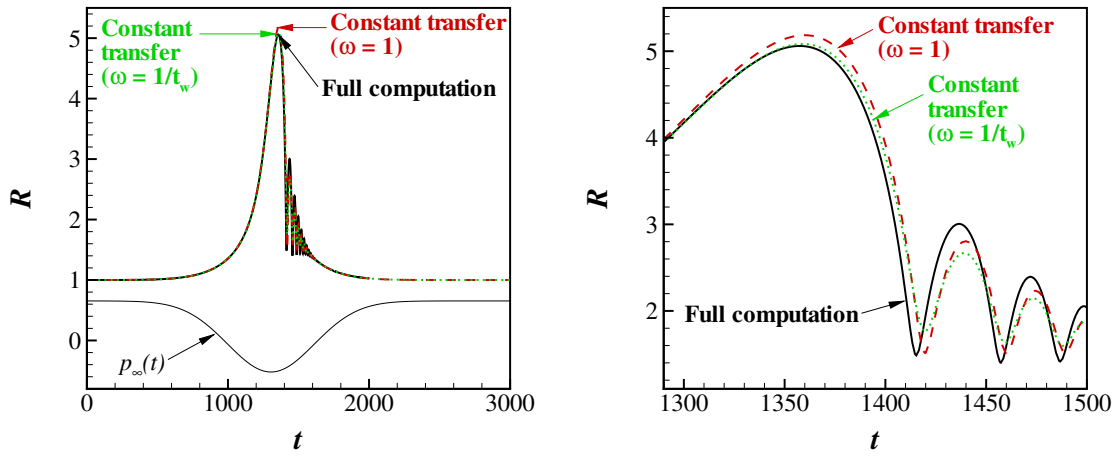

(a) Gross scale (b) Closeup

Figure 3.6: Bubble radius computed with the full computation, and the constant transfer model based upon $\omega = 1$ ($\beta_T = 6.62$, $\beta_C = 6.21$), and $\omega = 1/t_w$ ($t_w = 435$, $\beta_T = \beta_C = 5.00$). The forcing timescale is an order of magnitude larger than that in Figure 3.4, which accentuates the differences in the models. [Run 40,1000(c)].

model is shown to agree with the first order solution of the full equations.

We begin with the mass and heat diffusion equations (2.12) and (2.50) which are rewritten in terms of T, Pe_g, Pe_{a-v} and y as

$$\frac{\partial C}{\partial t} + \frac{u - y\dot{R}}{R}\frac{\partial C}{\partial y} = \frac{1}{R^2 Pe_{a-v}}\frac{\mathcal{R}T}{y^2}\frac{\partial}{\partial y}\left(\frac{y^2}{\mathcal{R}T}\frac{\partial C}{\partial y}\right), \tag{3.34}$$

$$\frac{\partial T}{\partial t} + \frac{U - y\dot{R}}{R}\frac{\partial T}{\partial r} = \frac{1}{R^2 Pe_g}\frac{1}{y^2}\frac{\partial}{\partial y}\left(\tilde{k}y^2\frac{\partial T}{\partial y}\right) + \frac{\gamma - 1}{\gamma}T\frac{\dot{p}}{p}. \tag{3.35}$$

The velocities are given by equations (2.51) and (2.52), which become

$$U = \frac{1}{RPe_g}\frac{\tilde{k}}{p}\frac{\partial T}{\partial y} - \frac{yR}{3\gamma}\frac{\dot{p}}{p}, \tag{3.36}$$

$$u = U + \frac{1}{RPe_{a-v}}\frac{\mathcal{R}_v - \mathcal{R}_a}{\mathcal{R}}\frac{\partial C}{\partial y}. \tag{3.37}$$

We shall also need equation (3.3) for the bubble pressure, which when combined with equation (3.4) becomes

$$\frac{\dot{p}}{p} = -3\gamma\left[\frac{\dot{R}}{R} - \frac{1}{R^2 Pe_g}\frac{\tilde{k}_w}{p}\frac{\partial T}{\partial y}\Big|_{y=1} - \frac{1}{R^2 Pe_{a-v}}\frac{\mathcal{R}_v}{\mathcal{R}_w}\frac{1}{1-C_w}\frac{\partial C}{\partial y}\Big|_{y=1}\right]. \quad (3.38)$$

Substituting equations (3.36) through (3.38) into equations (3.34) and (3.35) results in the following two PDEs for C and T,

$$\begin{aligned}
\frac{\partial C}{\partial t} &+ \left\{\frac{1}{R^2 Pe_g p}\left[\tilde{k}\frac{\partial T}{\partial y} - y\tilde{k}_w\frac{\partial T}{\partial y}\Big|_{y=1}\right] + \frac{1}{R^2 Pe_{a-v}}\left[\frac{\mathcal{R}_v - \mathcal{R}_a}{\mathcal{R}}\frac{\partial C}{\partial y} - \frac{\mathcal{R}_v}{\mathcal{R}_w}\frac{y}{1-C_w}\frac{\partial C}{\partial y}\Big|_{y=1}\right]\right\}\frac{\partial C}{\partial y} \\
&= \frac{1}{R^2 Pe_{a-v}}\frac{\mathcal{R}T}{y^2}\frac{\partial}{\partial y}\left(\frac{y^2}{\mathcal{R}T}\frac{\partial C}{\partial y}\right), \quad (3.39) \\
\frac{\partial T}{\partial t} &+ \left\{\frac{1}{R^2 Pe_g p}\left[\tilde{k}\frac{\partial T}{\partial y} - y\tilde{k}_w\frac{\partial T}{\partial y}\Big|_{y=1}\right] - \frac{1}{R^2 Pe_{a-v}}\frac{\mathcal{R}_v}{\mathcal{R}_w}\frac{y}{1-C_w}\frac{\partial C}{\partial y}\Big|_{y=1}\right\}\frac{\partial T}{\partial r} \\
&= \frac{1}{R^2 Pe_g}\frac{1}{y^2}\frac{\partial}{\partial y}\left(\tilde{k}y^2\frac{\partial T}{\partial y}\right) \\
&- 3(\gamma-1)T\left[\frac{\dot{R}}{R} - \frac{1}{R^2 Pe_g}\frac{\tilde{k}_w}{p}\frac{\partial T}{\partial y}\Big|_{y=1} - \frac{1}{R^2 Pe_{a-v}}\frac{\mathcal{R}_v}{\mathcal{R}_w}\frac{1}{1-C_w}\frac{\partial C}{\partial y}\Big|_{y=1}\right]. \quad (3.40)
\end{aligned}$$

We now assume the Peclet numbers to be small and let

$$Pe_g = \epsilon, \quad (3.41)$$

$$Pe_{a-v} = \theta\epsilon, \quad (3.42)$$

where $\epsilon \ll 1$ and $\theta = \mathcal{O}(1)$. We expand the variables and concentration dependent gas properties,

$$C(y,t) = C_w(t) + \theta\epsilon C_1(y,t) + \theta^2\epsilon^2 C_2(y,t) + \mathcal{O}(\epsilon^3), \quad (3.43)$$

$$T(y,t) = 1 + \epsilon T_1(y,t) + \epsilon^2 T_2(y,t) + \mathcal{O}(\epsilon^3), \quad (3.44)$$

$$\tilde{k}(y,t) = \tilde{k}_w(t) + \theta\epsilon\delta\tilde{k}C_1(y,t) + \theta^2\epsilon^2\delta\tilde{k}C_2(y,t) + \mathcal{O}(\epsilon^3), \quad (3.45)$$

$$\mathcal{R}(y,t) = \mathcal{R}_w(t) + \theta\epsilon\delta\mathcal{R}C_1(y,t) + \theta^2\epsilon^2\delta\mathcal{R}C_2(y,t) + \mathcal{O}(\epsilon^3), \quad (3.46)$$

where $\delta\tilde{k} \equiv \tilde{k}_v - \tilde{k}_a$ and $\delta\mathcal{R} \equiv \mathcal{R}_v - \mathcal{R}_a$. Substituting equations (3.43) through (3.46) into equations (3.39) and (3.40), and retaining only the zero-order terms yields

$$\frac{1}{y^2}\frac{\partial}{\partial y}\left(y^2\frac{\partial C_1}{\partial y}\right) = R^2\dot{C}_w \tag{3.47}$$

$$\frac{1}{y^2}\frac{\partial}{\partial y}\left(y^2\frac{\partial T_1}{\partial y}\right) = \frac{3pR^3(\gamma-1)}{\tilde{k}_w}\left[\frac{\dot{R}}{R^2} - \frac{\tilde{k}_w}{pR^3}\frac{\partial T_1}{\partial y}\Big|_{y=1} - \frac{1}{R^3}\frac{\mathcal{R}_v}{\mathcal{R}_w}\frac{1}{1-C_w}\frac{\partial C_1}{\partial y}\Big|_{y=1}\right]. \tag{3.48}$$

The solutions satisfying $C_1 = 0$ and $T_1 = 0$ at $y = 1$ are

$$C_1(y,t) = \frac{1}{6}R^2\dot{C}_w\left(y^2-1\right), \tag{3.49}$$

$$T_1(y,t) = \frac{pR^3(\gamma-1)}{2\tilde{k}_w}\left[\frac{\dot{R}}{R^2} - \frac{\tilde{k}_w}{pR^3}\frac{\partial T_1}{\partial y}\Big|_{y=1} - \frac{1}{3R}\frac{\mathcal{R}_v}{\mathcal{R}_w}\frac{\dot{C}_w}{1-C_w}\right]\left(y^2-1\right), \tag{3.50}$$

where the solution (3.49) has been used in the right-hand side of equation (3.50). Requiring self consistency of equation (3.50) yields

$$\tilde{k}_w\frac{\partial T_1}{\partial y}\Big|_{y=1} = pR^3\frac{\gamma-1}{\gamma}\left[\frac{\dot{R}}{R^2} - \frac{1}{3R}\frac{\mathcal{R}_v}{\mathcal{R}_w}\frac{\dot{C}_w}{1-C_w}\right], \tag{3.51}$$

so that the final solution for T_1 is given as

$$T_1(y,t) = \frac{pR^3}{\tilde{k}_w}\frac{\gamma-1}{2\gamma}\left[\frac{\dot{R}}{R^2} - \frac{1}{3R}\frac{\mathcal{R}_v}{\mathcal{R}_w}\frac{\dot{C}_w}{1-C_w}\right]\left(y^2-1\right). \tag{3.52}$$

Now that the first-order solutions for C and T have been found, we can insert them into equation (3.38) to obtain

$$\frac{\dot{p}}{p} = \frac{\mathcal{R}_v}{\mathcal{R}_w}\frac{\dot{C}_w}{1-C_w} - 3\frac{\dot{R}}{R} + \mathcal{O}(\epsilon), \tag{3.53}$$

which is the equation describing the pressure change in an isothermal bubble with infinitely fast mass diffusion. To obtain the first-order term, we would require the solution for C_2 and T_2. Note that if we set $C_w = 0$ and integrate, we obtain the relation for an isothermal (constant mass) gas bubble, $pR^3 = 1$. Inserting this result into equation (3.52) with $C_w = 0$ and $\tilde{k}_w = 1$, results in the same expression obtained by Prosperetti (1991) for a pure gas bubble. It is this expression that is the basis for their nearly isothermal model that is tested in Section 3.5.2.

Finally we insert the first-order solutions for C and T into the definition of the transfer coefficients [equation (2.62)] to obtain

$$\beta_C^{full} \equiv -\frac{\partial C/\partial y|_{y=1}}{\bar{C} - C_w} = 5 + \mathcal{O}(\epsilon), \tag{3.54}$$

$$\beta_T^{full} \equiv -\frac{\partial T/\partial y|_{y=1}}{\bar{T} - T_w} = 5 + \mathcal{O}(\epsilon). \tag{3.55}$$

These transfer coefficients, obtained from the full set of equations, match those that are used in the model equations as $\epsilon \to 0$. Thus, the model equations become exact as $Pe_g \to 0$ and $Pe_{a-v} \to 0$.

3.5 Evaluation of models

In this section we demonstrate that the constant transfer model is more accurate than other reduced-order models by comparing results directly to full bubble computations. We explore a wide range of forcings, ranging from the Gaussian pulses used in previous sections, to harmonic forcing where the frequency and amplitude is varied systematically. In addition we adapt the constant transfer model to one that assumes the mass diffusion to be infinitely fast, and we examine pure gas bubbles. This enables the thermal and mass modeling to be assessed independently.

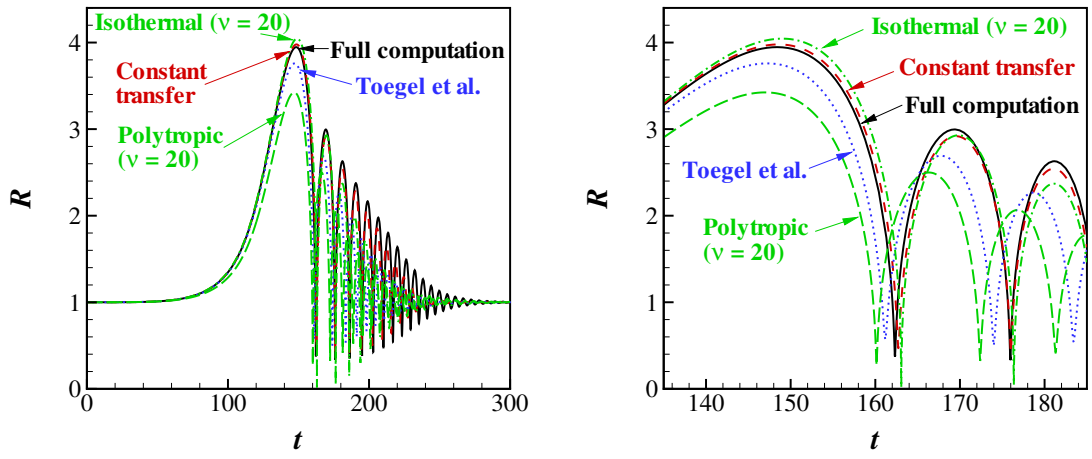

(a) Gross scale (b) Closeup

Figure 3.7: Bubble radius computed with full computation and a variety of models for a gas-vapor bubble with $Pe_g = 36.4$ and $Pe_{a-v} = 28.8$; Constant transfer model ($\beta_T = 6.62$, $\beta_C = 6.21$), model of Toegel et al. (2000), isothermal model ($\nu = 20$), polytropic model ($k_{\mathit{eff}} = 1.21$, $\nu = 20$). [Run 40,100(d)].

3.5.1 Gas-vapor bubbles

The constant transfer model is compared to the full computation and other reduced-order models for Gaussian forcings. Figures 3.7 and 3.8 compare the different models with a full computation for two pressure pulses of disparate timescales. As explained in Section 3.3 the constant transfer model slightly overestimates the initial growth and over damps the rebounds. However, the constant transfer model is superior to the other reduced-order models which show greater differences to the full computation. In particular the polytropic model significantly underestimates the initial bubble growth, due to the effective polytropic index $k_{\mathit{eff}} = 1.21$ being determined from linear analysis (Prosperetti et al. 1988). In reality the timescale for bubble growth is far slower than the timescale that is associated with the bubble natural frequency that was used to compute k_{eff}, so the true behavior is far closer to isothermal, or $k_{\mathit{eff}} = 1$. Interestingly, though the constant transfer model also uses the bubble natural frequency to compute transfer coefficients, it is clearly not as sensitive to its value.

The isothermal model makes a better estimate of the slow initial growth than the polytropic model, but in this case the growth is overestimated. This is likely due to

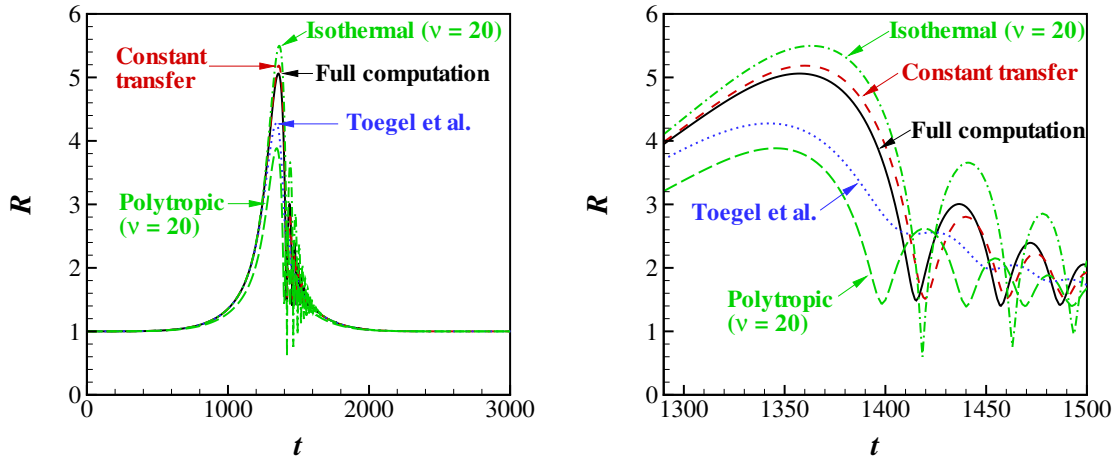

(a) Gross scale

(b) Closeup

Figure 3.8: Bubble radius computed with full computation and a variety of models for a gas-vapor bubble with $Pe_g = 36.4$ and $Pe_{a-v} = 28.8$; Constant transfer model ($\beta_T = 6.62$, $\beta_C = 6.21$), model of Toegel et al. (2000), isothermal model ($\nu = 20$), polytropic model ($k_{\mathit{eff}} = 1.21$, $\nu = 20$). The timescale of the pulse is an order of magnitude larger than that in Figure 3.7, which highlights the deficiencies of the various models. [Run 40,1000(c)].

the infinitely fast diffusion of vapor, as explained at the end of this section. There are also problems with the isothermal model that are associated with the use of an effective liquid viscosity, $\nu \equiv \nu'_{\mathit{eff}}/\nu'_l$, to account for damping due to the otherwise neglected diffusive effects. The value $\nu = 20$ is chosen to match linear analysis of the full diffusion equations (Prosperetti et al. 1988), and works reasonably well for the first bubble rebound in Figure 3.7(b). However, it increasingly over damps the subsequent rebounds. Furthermore, in Figure 3.8(b) the same value of effective viscosity results in under attenuated bubble rebounds. This might be corrected by using a higher effective viscosity, but the fact that the appropriate value to use is not known a priori is a major limitation of this approach.

The model of Toegel et al. (2000) (and the similar model used by Matula et al. (2002)) uses estimates for the fluxes based upon estimates of the diffusive penetration lengths. The timescale used in their estimates is $t_R \propto R/|\dot{R}|$, which results in the non-realistic situation of low heat and mass transfer during the final stage of collapse and initial rebound when $\dot{R} \approx 0$. While the duration of this non-realistic behavior

is so short as to not adversely impact the bubble dynamics the model has severe limitations due to the equations not matching the full equations in the limit of low Pe (slow timescales). This is demonstrated in both Figures 3.7 and 3.8, where the model of Toegel et al. significantly underestimates the initial growth. This is especially evident in the latter figure for which the forcing is ten times slower. In addition the model has an error in the treatment of the mass transfer, which results in the incorrect scenario of the mass transfer still being limited by diffusion in the event of the vapor concentration approaching unity. While this error is not substantial for the present plots where bubble growth is moderate and the vapor concentration is not near unity, for large bubble growths [such as those due to the lithotripsy pulses in Matula et al. (2002)] the error becomes significant.

The various models are now compared for a wide range of t_w, A, Pe_g and Pe_{a-v} in Figure 3.9. Plotted are the relative errors in some of the important variables. In comparing the isothermal, polytropic and adiabatic models, we use $\nu = 1$, for the lack of a better known value. The errors in all the variables are consistently lower for the constant transfer model than for other reduced-order models. In particular the constant transfer model yields estimates of R_{max} within a few percent of the full computation. For moderate bubble growths the important variable, $R_{rebound}$, is also within a few percent of the full computation, while for some larger bubble growths the errors are as high as 30%. The errors in R_{min} are typically within 20 to 30%, except for one data point where the error is as high as 80%. In the context of the small minimum radii, such large relative errors do not have significant consequences. In any case, the estimates of R_{min} of the constant transfer model are more accurate than those of the other models.

The constant transfer model yields estimates for T_{max} within about 20% of the full computations, which is more accurate than estimates from other models. Estimates of p_{max} and $\bar{C}_{min}$ from the constant transfer model are only accurate to within an order of magnitude, but these too are more accurate than those from the other reduced-order models. In addition, even such crude estimates may be useful in determining trends in sonochemical yields (Storey & Szeri 2001).

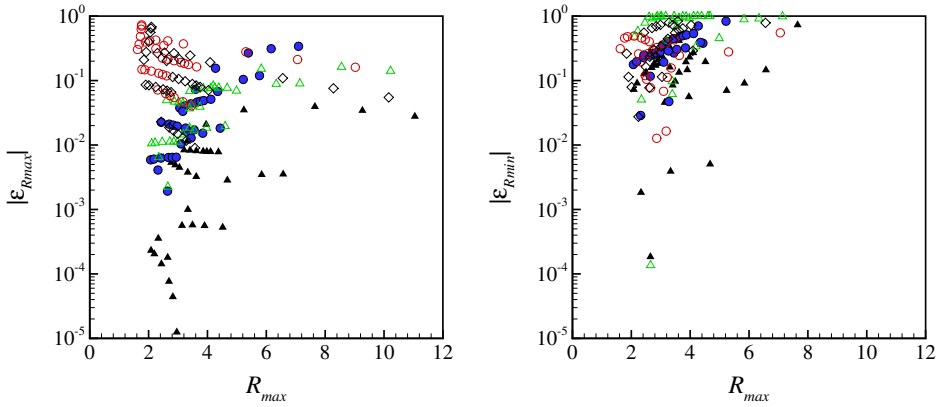

(a) Maximum radius

(b) Minimum radius

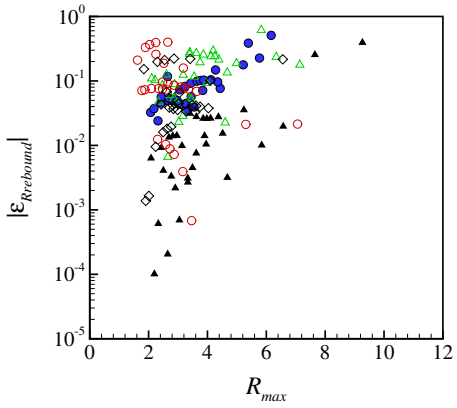

(c) Rebound radius

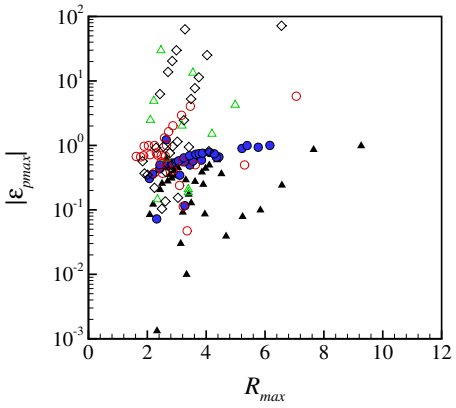

(d) Maximum bubble pressure

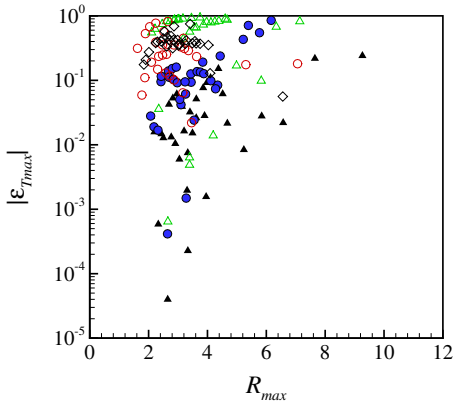

(e) Maximum average bubble temperature

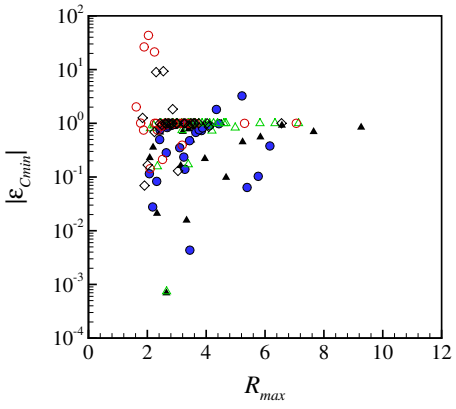

(f) Minimum average vapor concentration

Figure 3.9: Relative errors of important variables for different models over a wide range of forcing parameters. ▲ Constant transfer model; ● Toegel et al. (2000); △ isothermal ($\nu = 1$); ○ adiabatic ($\nu = 1$); ◇ polytropic ($\nu = 1$). Runs for all the data points are listed in Table A.2. All of the listed runs except for those indicated in the table have been used for this figure.

Finally we examine the importance of modeling mass diffusion by modifying the constant transfer model to one that assumes mass diffusion to be infinitely fast. This is achieved by redefining the pressure, p, in equations (3.1) and (3.3) to be the partial pressure of non-condensible gas, p_a. The constant vapor pressure $p_{v_{sat}}$ is then added to equation (3.1) and the $\dot{m}_v''$ term is removed from equation (3.3) to yield

$$\tilde{p}_0 \left[p_a + p_{v_{sat}} - p_\infty(t) \right] = R\dot{V} + \frac{3}{2}V^2 + \frac{4}{Re}\frac{V}{R} + \frac{2}{WeR}, \tag{3.56}$$

$$\frac{dp_a}{dt} = \frac{-3\gamma}{R}\left[p_a V - \frac{1}{Pe_g}\frac{1}{R}\tilde{k}_w \frac{\partial T}{\partial y}\Big|_{y=1} \right]. \tag{3.57}$$

Equations (3.4) and (3.12) are then replaced by

$$m_v = \frac{m_{a_0}}{\theta}, \tag{3.58}$$

where θ is given by equation (3.9). The above equation is derived by noting for infinitely fast mass diffusion, $\bar{C} = C_w$, which enables equation (3.8) and approximation (3.13) (which is now exact due to the uniform concentration distribution) to be combined.

The bubble radius computed by the full computation and the constant transfer model with both finite and infinitely fast mass diffusion is plotted in Figure 3.10(a). It is apparent that infinitely fast mass diffusion results in significant overestimation of the initial bubble growth and subsequent rebounds. The attenuation rate of the rebounds and the bubble minimum radii are underestimated. Plots of the average and wall vapor concentrations in Figure 3.10(b) show a higher average vapor concentration for the model with fast mass diffusion, which indicates that the overestimation of the bubble growths is due to too much evaporation into the bubble. The constant transfer model with finite diffusion is able to predict the average and wall vapor concentrations remarkably well. It appears that for relatively moderate growth, mass diffusion in the bubble interior is a limiting factor in the bubble growth. The same may not

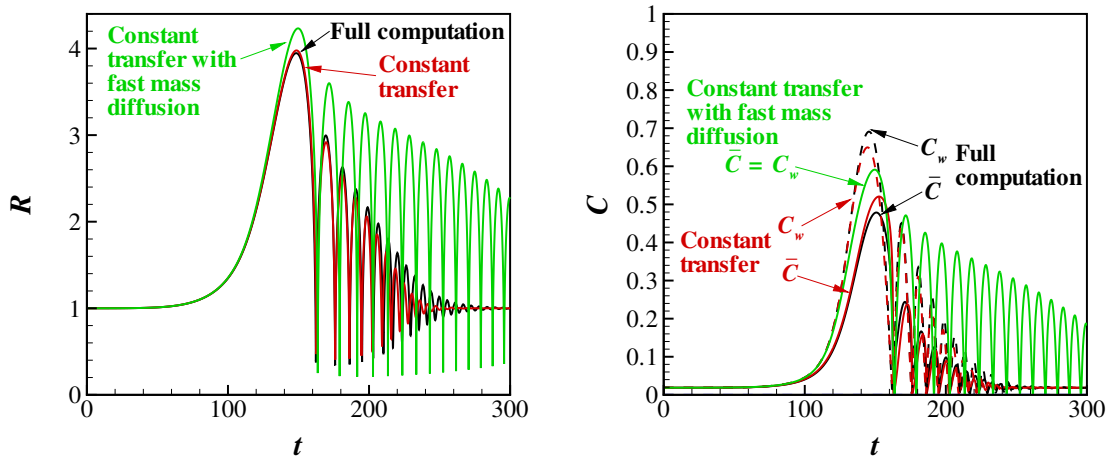

(a) Bubble radius

(b) Concentrations

Figure 3.10: Bubble radius and concentrations computed with the full computation, the constant transfer model with finite rate mass diffusion modeling and the constant transfer model with infinitely fast mass diffusion. The bubble consists of gas and vapor with $Pe_g = 36.4$ and $Pe_{a-v} = 28.8$. The importance of modeling the finite rate mass diffusion is illustrated by excessive bubble growth in the model that does not account for it. [Run 40,100(d)].

hold true for larger bubble growths, where the bubble interior may eventually consist almost entirely of vapor and hence the transport of vapor would not be limited by mass diffusion. In this case the denominators in equations (3.4) and (3.58) would approach zero and the model equations may become singular. In this limit the bubble practically consists of pure vapor with the pressure, p, simply being given by $p_{v_{sat}}$.

Another feature of the solution that is obtained by assuming infinitely fast mass diffusion is the absence of significant vapor content during the fast bubble collapse. Although it is not clear on the scale of Figure 3.10(b) the average vapor concentration during collapse obtained from the model with fast mass diffusion is an order of magnitude lower than it is for the full computation and the constant transfer model with finite rate diffusion. It is obvious that the vapor trapping effect identified by Storey & Szeri (2000) is important in this particular circumstance, and the mass diffusion modeling in the constant transfer model is able to capture this behavior. This may have important consequences in sonochemistry applications where the amount of vapor trapped in the bubble during collapse would impact on the chemical reactions. In

the present application of modeling bubble dynamics the modeling of mass diffusion is important during the collapse stage to avoid the far smaller minimum radii observed in Figure 3.10(a) for the model with fast mass diffusion.

3.5.2 Gas bubbles

The constant transfer model is now tested for the simpler situation of a pure gas bubble, thereby removing the need for mass diffusion modeling. This enables errors in approximations to the heat transfer to be gauged independently, and also enables comparison to other models that have been developed for heat transfer only.

Figures 3.11 and 3.12 compare computed bubble radii of different models to the full computation for gas bubbles with $Pe_g = 4.61$ and 34.8, respectively. For the lower value of Pe_g (Figure 3.11) the behavior is close to the isothermal limit, and as anticipated the constant transfer model is essentially identical to the full computation. In addition the nearly isothermal model of Prosperetti agrees almost exactly with the full computation, since this is within the limit for which the model is valid. The model of Storey & Szeri (2001) underestimates the attenuation because there is no thermal damping in either the isothermal or adiabatic limits that the model switches between. The polytropic model with effective viscosity (chosen to match linear analysis) underestimates the initial growth, probably due to too much viscous damping that results from the effective viscosity.

For the bubble with larger Pe_g the behavior departs from the isothermal limit. Figure 3.12 shows that the constant transfer model accurately captures the initial bubble growth and the attenuation of the bubble rebounds. The absence of thermal damping in the switching model of Storey & Szeri (2001) results in the slow decay of the rebounds. By contrast, the nearly isothermal model of Prosperetti over predicts the attenuation of the bubble rebounds. The polytropic model also behaves poorly since, as explained in Section 3.5.1, the use of a polytropic index of $k_{\mathit{eff}} = 1.21$ prevents the correct prediction of the initial expansion which is relatively slow and therefore nearer the isothermal limit. Again it seems that the constant transfer model

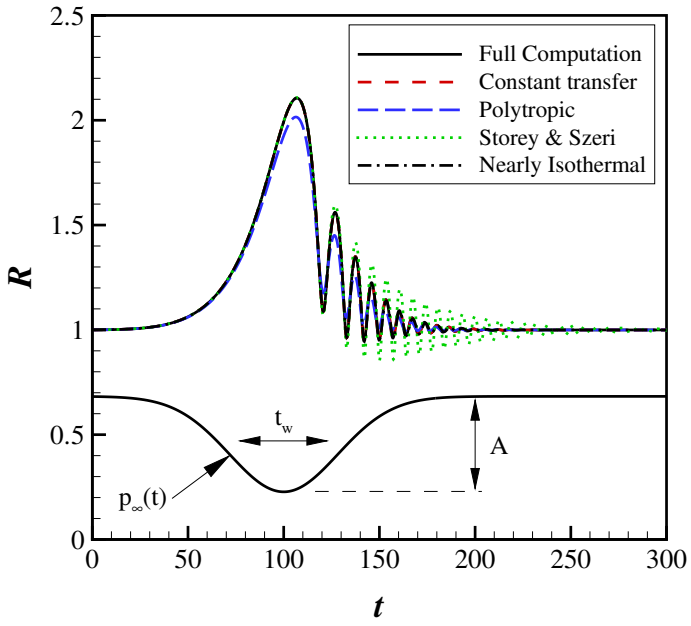

Figure 3.11: Computed radius for a gas bubble ($Pe_g = 4.61$) subject to a Gaussian decrease in far field pressure ($A = 1.0$, $t_w = 40.0$). The curves show comparisons to the full computation of the constant transfer model ($\beta_T = 5.05$), the polytropic model with effective damping ($\nu = 2.6$, $k_{eff} = 1.03$), the switching model of Storey & Szeri (2001), and the nearly isothermal model of Prosperetti (1991). [Run G4].

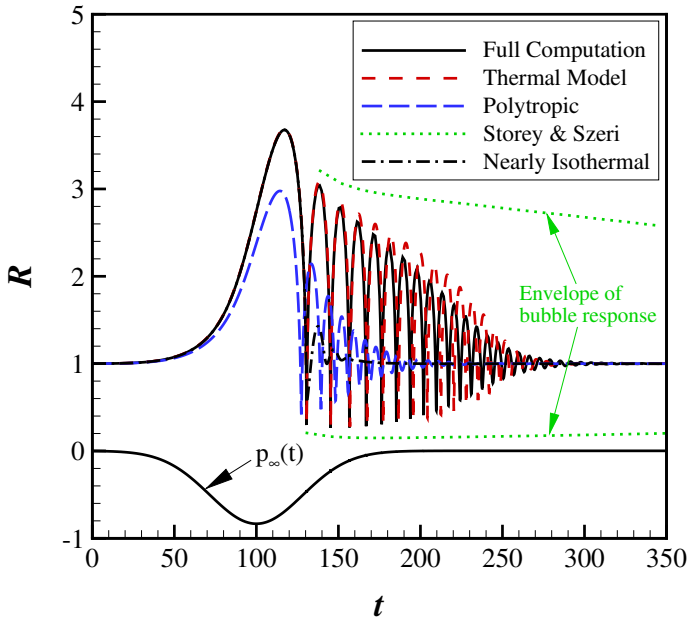

Figure 3.12: Computed radius for a gas bubble ($Pe_g = 34.8$) subject to a Gaussian decrease in far field pressure ($A = 1.0$, $t_w = 40.0$). The curves show comparisons to the full computation of the constant transfer model ($\beta_T = 6.54$), the polytropic model with effective damping ($\nu = 20$, $k_{eff} = 1.21$), the switching model of Storey & Szeri (2001), and the nearly isothermal model of Prosperetti (1991). [Run G40].

can correctly capture the nearly isothermal expansion even though we use a value of β_T that has been chosen to match behavior away from this limit.

Figure 3.12 demonstrates that the constant transfer model slightly underestimates the initial attenuation of the rebounds. This is in contrast to the case for a gas-vapor bubble in Figure 3.7 (which has a similar value of Pe_g) where the attenuation is overestimated. It is clear then that this is due primarily to the modeling of the mass diffusion. This is consistent with observations regarding Figure 3.5(b), in which it was suggested a higher value of mass transfer coefficient may be needed to achieve a better match of bubble rebounds. This would however presumably be at the expense of increasing the degree to which the constant transfer model overestimates the initial bubble growth.

3.5.3 Harmonic forcing

The constant transfer model is intended for application to bubbles exposed to the arbitrary pressure excursion that may arise in continuum bubbly model flows. While the previously used Gaussian pressure pulses provide a quick means of testing reduced-order models for a variety of forcings, it is perhaps more systematic to test them with harmonic forcings over a wide range of frequencies and amplitudes. In this section we compare the constant transfer model with the often used polytropic model [using the effective values of polytropic index, k_{eff}, and damping ratio, $\nu \equiv \nu'_{eff}/\nu'_L$, obtained to match linear theory (Prosperetti et al. 1988)] and the full computation of the complete conservation equations. The harmonic forcing field is given by,

$$p_\infty(t) = p_{\infty_0}\left(1 + A\sin\omega_f t\right), \tag{3.59}$$

where A is the non-dimensional amplitude and ω_f is non-dimensionalized by the linear natural bubble frequency. In the present application it is clear that the forcing frequency ω_f should be used as the characteristic frequency in equation (3.21) to compute the appropriate value of β_T for the constant transfer model. However, as mentioned previously, in more general applications the bubble forcing will not have a well defined frequency and we choose the characteristic frequency to be the bubble natural frequency. Therefore in order to provide an unbiased test of the model that can be extrapolated to general forcing, we compute β_T by setting $\omega = 1$ (corresponding to the natural bubble frequency) in equation (3.21), regardless of the actual forcing frequency. To be consistent, we also use $\omega_f = 1$ when computing the value of effective polytropic index and damping to use in the polytropic model.

Figure 3.13 shows a bifurcation diagram of the computed bubble radius sampled at every period of forcing pressure for a gas bubble with $Pe_g = 9.26$ driven at a forcing frequency $\omega_f = 0.8$ with an incrementally increasing driving pressure amplitude. Once steady-state was reached at $A = 1.2$ the pressure was increased at a rate of 10^{-3} per cycle up to $A = 1.5$ and then at a rate of 10^{-4} per cycle. The curves show comparisons

to the full computation of the constant transfer model and the polytropic model with and without effective damping ($\nu = 6.35$ and 1, respectively).

The curve for the constant transfer model is almost identical to the full computation through the first and second sub-harmonic bifurcations at $A \approx 1.61$ and 1.90. At $A \approx 1.96$ the full computation and constant transfer model both predict chaotic behavior for which the exact form was found to be very sensitive to tolerances in the numerical integration as well as the rate at which the driving pressure amplitude was increased. In contrast to the constant transfer model the curve for the polytropic model with effective damping ($\nu = 6.35$) is shifted significantly to the right and below the full computation. Interestingly the polytropic model without effective damping ($\nu = 1$) yields results that agree much more closely with the full computation, although the radius is slightly higher due to lack of thermal damping. It appears that the addition of effective damping to the polytropic model substantially delays the onset of the bifurcations as well slightly over damping the bubble response. The use of this model in certain regimes could result in gross errors in predicted bubble response. The excellent accuracy of the constant transfer model is to be expected, since the value of $Pe_g = 9.26$ is low enough to be near the low Peclet number limit, where the model equations are shown to agree with the full equations (Section 3.4). Indeed, the constant transfer model uses $\beta_T = 5.18$, which is close to the low Peclet number limit of 5.

Now the response of the different models at varying forcing frequencies are examined. Figure 3.14 shows the response of a gas bubble with $Pe_g = 9.26$ forced with non-dimensional pressure amplitude $A = 0.6$ over a range of frequencies. This plots shows the maximum value of bubble radius attained during a steady oscillation. The graph is constructed by picking a forcing frequency and integrating the equations forward in time until steady-state cycles are achieved. It should be noted that around each of the harmonic peaks there actually exist two different stable steady-state solutions (Prosperetti 1974, Lauterborn 1976). The solution that is found depends upon the initial conditions of the computation. We always start with a bubble in static equilibrium ($R = 1$ and $\dot{R} = 0$) and find only one of these solutions. If we also chose

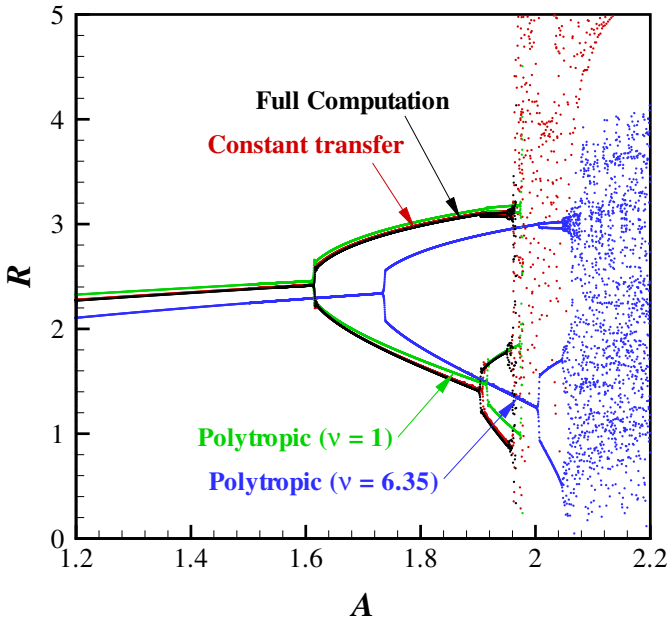

Figure 3.13: Bifurcation diagram of the bubble radius sampled at every period of the forcing pressure for a gas bubble ($Pe_g = 9.26$) driven with forcing frequency $\omega_f = 0.8$ and a slowly increasing pressure amplitude, A. The curves show comparisons to the full computation of the constant transfer model ($\beta_T = 5.18$) and the polytropic model with and without effective damping ($\nu = 6.35$ and 1, respectively, $k_{eff} = 1.079$). [Run G10].

initial conditions to find the other solution, we would be able to see the hysteresis behavior typical of many non-linear systems.

The constant transfer model shows excellent agreement with the full computation over all frequencies, even though the model is tuned for forcing at the bubble natural frequency ($\omega_f = 1$). By contrast, as first identified by Prosperetti et al. (1988), neither of the polytropic models are able to predict the location and magnitude of the harmonic peaks. Indeed the behavior of the polytropic model depends strongly on the value of effective damping that is used.

A feature of the polytropic model without effective damping is the peak occurring at $\omega_f \approx 0.63$ that is absent in all the other models. This peak is caused by a $\frac{3}{2}$ ultra-harmonic mode that is damped by the other models and the full computation. The existence of this spurious peak, and additional ultra-harmonic peaks at higher forcing amplitudes (Lauterborn 1976), gives rise to errors in the response of a bubble under certain forcings. Figure 3.15 illustrates this situation. The left plot is at a forcing frequency just below the ultra-harmonic peak ($\omega_f = 0.631$) where the isothermal model with and without effective damping closely matches the constant transfer model and full computation. However, a small increase in the forcing frequency ($\omega_f = 0.632$) results in a large change in behavior of the isothermal model without effective damping, as shown on the right plot. The amplitude of response has approximately doubled, and the period of the bubble motion has doubled. The behavior of the constant transfer model is virtually unchanged, in agreement with the full computation.

The bifurcation and frequency-response curves for a gas bubble with larger $Pe_g = 42.9$ are plotted in Figures 3.16 and 3.17. This value of Peclet number is significantly away from the low Peclet number limit ($\beta_T = 6.96$), but the figures show similar trends as for the previous case of lower Peclet number. Excellent agreement of the constant transfer model with the full computation is demonstrated through the first sub-harmonic bifurcation at $A \approx 1.56$. The agreement at the second harmonic bifurcation is not as good, with the full computation giving the bifurcation at $A \approx 1.85$ while the constant transfer model bifurcated at $A \approx 1.86$. The onset of chaotic oscil-

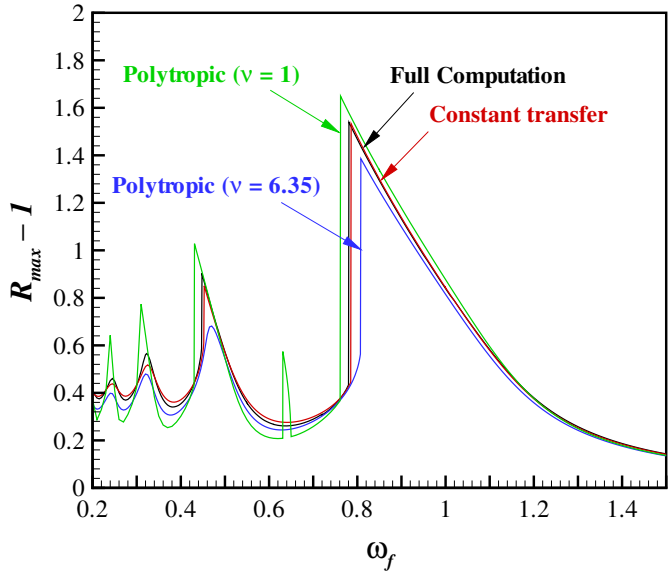

Figure 3.14: Frequency-response curves for the forced oscillations of a gas bubble ($Pe_g = 9.26$) for a dimensionless pressure amplitude $A = 0.6$. The curves show comparisons to the full computation of the constant transfer model ($\beta_T = 5.18$) and the polytropic model with and without effective damping ($\nu = 6.35$ and 1, respectively, $k_{eff} = 1.079$). [Run G10].

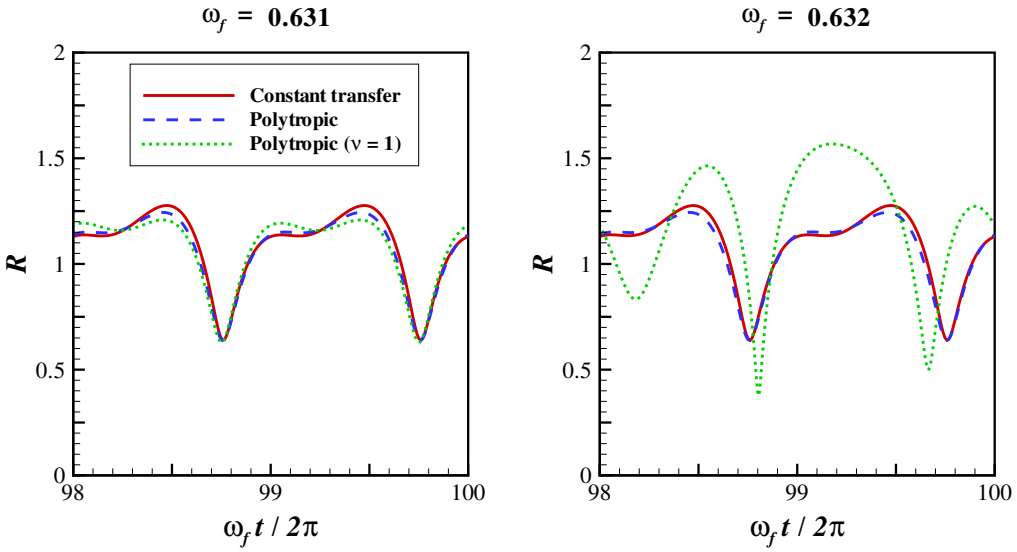

Figure 3.15: Bubble radius over two steady-state forcing cycles at $\omega_f = 0.631$ and $\omega_f = 0.632$ computed by constant transfer model and polytropic model with and without effective damping ($\nu = 6.35$ and 1, respectively). Conditions are as for Figure 3.14.

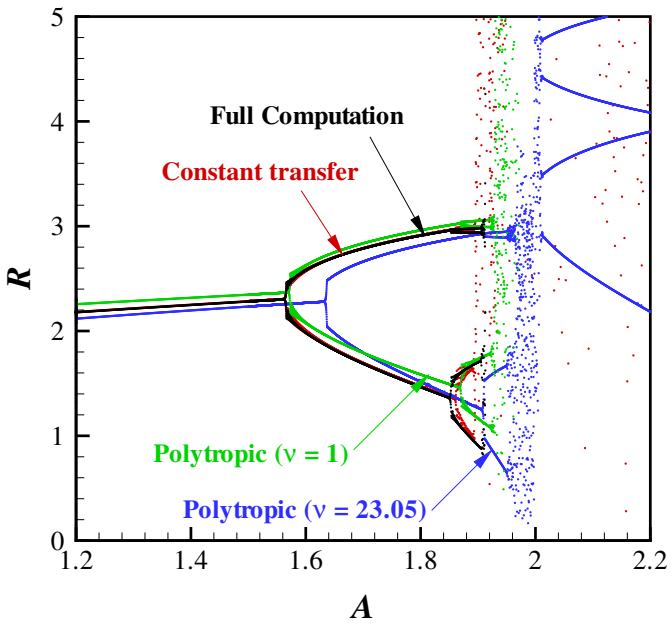

Figure 3.16: Bifurcation diagram of the bubble radius sampled at every period of the forcing pressure for a gas bubble ($Pe_g = 42.9$) driven with forcing frequency $\omega_f = 0.8$ and a slowly increasing pressure amplitude, A. The curves show comparisons to the full computation of the constant transfer model ($\beta_T = 6.96$) and the polytropic model with and without effective damping ($\nu = 23.05$ and 1, respectively, $k_{eff} = 1.230$). [Run G50].

lations set in at $A \approx 1.91$ for the full computation and at $A \approx 1.90$ for the constant transfer model.

The constant transfer model is again superior to either of the polytropic models, although the polytropic model without damping does show reasonable agreement with the full computation. Again the addition of effective damping causes the onset of the bifurcations to be delayed. At higher forcings ($A \gtrsim 2$) the polytropic model with effective damping returns from the chaotic oscillations to the sub-harmonic oscillations. It is important to note however that at these higher forcing amplitudes the curves appear to depend strongly upon numerical tolerances in the integration as well as the rate at which the amplitude is increased.

Figure 3.17 shows the frequency-response curves for the gas bubble with $Pe_g = 42.9$. Again we see excellent agreement of the constant transfer model with the full

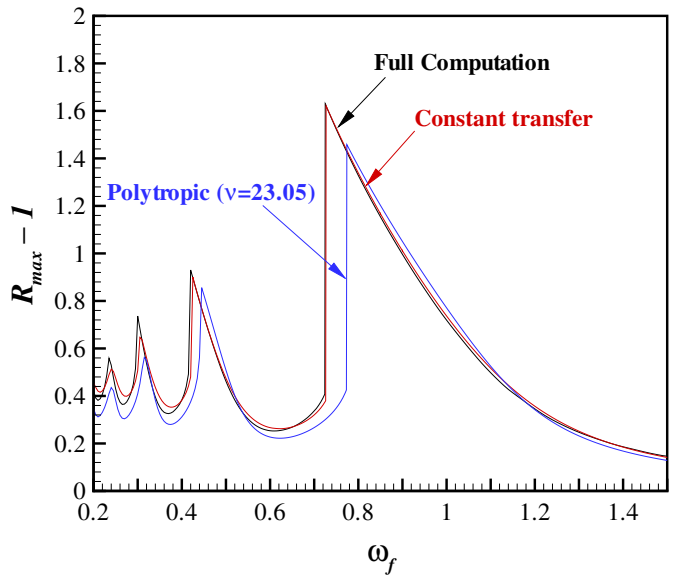

Figure 3.17: Frequency-response curves for the forced oscillations of a gas bubble ($Pe_g = 42.9$) for a dimensionless pressure amplitude $A = 0.6$. The curves show comparisons to the full computation of the constant transfer model ($\beta_T = 6.96$) and the polytropic model with effective damping ($\nu = 23$, $k_{eff} = 1.23$). [Run G50].

computation. The polytropic model with effective damping does not correctly predict the positions of the jumps and also appears to underestimate the maximum radius at low forcing frequencies. The polytropic model does a poorer job for the larger bubble radius, as may be expected because the viscous damping upon which the effective damping is based upon is of far lower magnitude for larger radius bubbles. The response curve for the polytropic model without effective damping (not shown here) exhibited many more peaks due to the existence of many ultra-harmonics. This is because the lower viscous damping of the larger radius bubble does not damp out any of these peaks. These results are consistent with Lauterborn (1976) who demonstrated that for small bubbles (high viscous damping) only the sub-harmonic peaks would show up, while for larger bubbles (low viscous damping) more and more peaks corresponding to ultra-harmonic modes are present.

3.6 Summary of the model

A new model for the diffusive effects in bubble dynamics has been presented. The model uses estimates for the fluxes of heat and vapor at the bubble wall based on constant heat and mass transfer coefficients. This approach was motivated by POD results that indicated that most of the energy is captured by the first POD mode. Linear analysis provides a means for computing the transfer coefficients, as well as indicating possible limitations of the approach, particularly for moderate or large Peclet numbers. The linear analysis was based on a dominant frequency (or timescale) which was taken to be the bubble natural frequency. Analysis of the constant transfer model equations show that they become exact as Pe_g and $Pe_{a-v} \to 0$. Comparison of the constant transfer model to full computations for both gas-vapor and pure gas bubbles indicate very good agreement for a wide range of Peclet numbers and forcing amplitudes, widths and frequencies. In all situations the constant transfer model was superior to other reduced-order models.

3.7 Extension of model for *hot* liquids

As mentioned in Section 2.3.2, it is necessary to include the temperature variation in the liquid for bubbles in a hot liquid where the temperature of the bubble wall, T_w, plays a critical role in determining the bubble dynamics. The analysis of Plesset & Zwick (1952) provides a means for estimating T_w, but the evaluation of the convolution integral becomes prohibitive for long computations. In this section we apply the same method that was used for the interior diffusion problems to the exterior temperature field to obtain an estimate of T_w.

3.7.1 Model equations

Introducing the liquid temperature variation into the model requires equation (3.7) to be replaced by a balance of energy at the interface, equation (2.28), which is rewritten here in terms of T and with the convective terms being neglected,

$$L\dot{m}_v'' = \frac{\tilde{T}_0}{PrReR}\left[\frac{\partial T_l}{\partial y} - k\frac{\partial T}{\partial y}\right]\Big|_{y=1}. \tag{3.60}$$

Following the treatment of the internal problem we approximate the temperature gradient in the liquid by

$$\frac{\partial T_l}{\partial y}\Big|_{y=1} \approx -\beta_{T_l}\left(T_w - T_{l_\infty}\right), \tag{3.61}$$

where β_{T_l} is the heat transfer coefficient for the liquid, that can be determined either from linear analysis (Section 3.7.2) or POD computations (Section 2.5.3). Substituting equation (3.61) together with (3.4),(3.6),(3.5),(3.8) and (3.9) into equation (3.60) results in an equation with T_w being the only free variable. This non-linear equation is solved for T_w at every time step in the computation using Newton Raphson iterations.

3.7.2 Linear analysis of liquid temperature field

The diffusion equation (2.5) for the liquid temperature is linearized for small amplitudes (denoted by primes),

$$\frac{\partial T_l'}{\partial t} = \frac{1}{PrRe}\frac{1}{y^2}\frac{\partial}{\partial y}\left(y^2\frac{\partial T'}{\partial y}\right), \tag{3.62}$$

and is furnished by boundary conditions, $T_l'|_{y=1} = T_w'(t)$ and $T_l'|_{y\to\infty} = 0$. The solution can be written in the frequency domain as

$$\hat{T}_l(y,\omega) = \hat{T}_w(\omega)\frac{\exp[-\sqrt{i\omega PrRe}y]}{y\exp[-\sqrt{i\omega PrRe}]}, \tag{3.63}$$

where the hat denotes the Fourier transform. Differentiating and evaluating at the

bubble wall results in

$$\left.\frac{\partial \hat{T}_l}{\partial y}\right|_{y=1}(\omega) = -\left(1+\sqrt{i\omega PrRe}\right)\hat{T}_w(\omega). \tag{3.64}$$

Analogous to the the interior problem (Section 3.2) we determine the heat transfer coefficient for the liquid side to be

$$\begin{aligned} \beta_{T_l} &\equiv \Re\{1+\sqrt{i\omega PrRe}\}|_{\omega=1}, & (3.65)\\ &= 1+\sqrt{PrRe/2}. & (3.66) \end{aligned}$$

Here (as in Section 3.2) it is assumed that the bubble natural frequency is dominant in a bubble motion. However, the typical bubble response in a hot liquid (Figure 2.6) appears to closely follow the timescale of the forcing, t_w. It is therefore useful to define a heat transfer coefficient based upon t_w as

$$\beta_{T_l}^{t_w} = 1+\sqrt{PrRe/2t_w}. \tag{3.67}$$

3.7.3 Sample result

The extended model is tested by comparing it to the full computation that was presented in Section 2.3.2. First we are required to set the value of the liquid heat transfer coefficient, β_{T_l}. The previous section presented two possible estimates of β_{T_l}, while Section 2.5.3 suggested another value of β_{T_l} based upon POD analysis of the liquid temperature field. Table 3.1 gives values of β_{T_l} as determined by the three methods for the computation of Section 2.3.2. It is clear that the result of the POD analysis is in reasonable agreement with that of the linear analysis based upon t_w, while the linear analysis based upon $\omega = 1$ yields a much higher value. This indicates, for thermally controlled bubbles, that $\omega = 1/t_w$ is a more appropriate

choice of dominant frequency than $\omega = 1$.

Method	β_{T_l}
Linear analysis, $\omega = 1$	30.66
Linear analysis, $t_w = 18.4$	7.914
POD analysis	5.7

Table 3.1: The value of the liquid heat transfer coefficient, β_{T_l}, determined by linear analysis with two different timescales, and POD analysis. The values obtained by the linear analysis based upon t_w and the POD analysis are in close agreement.

Figure 3.18 compares the bubble radius, R, and bubble wall temperature, T_w, from the full computation to that of the extended model, for the three different values of β_{T_l} from Table 3.1. Also plotted is the result of the model with $\beta_{T_l} \to \infty$, which is equivalent to the cold liquid model of the previous sections. This cold liquid model results in substantially different bubble dynamics, with the radius growing to $R_{max} \approx 12$ before collapsing (off scale on the plot). The results of the extended model for finite values of β_{T_l} are encouraging in that the bubble response is clearly damped by changes in T_w. However, the model is sensitive to the value of β_{T_l} that is used, and none of the estimates result in good agreement of the bubble dynamics. While it is likely that better agreement would be able to be obtained by finding an appropriate value of $\beta_{T_l} \in [7.914, 30.66]$ by trial and error, this value is not likely to be accurate for different bubble forcings. The deficiencies in the model for the liquid temperature are similar to those of the polytropic model for the internal problem, where the appropriate value of effective viscosity can not accurately be predicted a priori. In addition, even if the appropriate value of β_{T_l} was able to be determined, the hot liquid model is unable to capture some of the more subtle aspects of heat transfer in the liquid. Most notably, the model would not predict the relatively slow cooling of the bubble wall as illustrated by the full computation of Figure 3.18(b). For these reasons, the hot liquid model is of limited practical use.

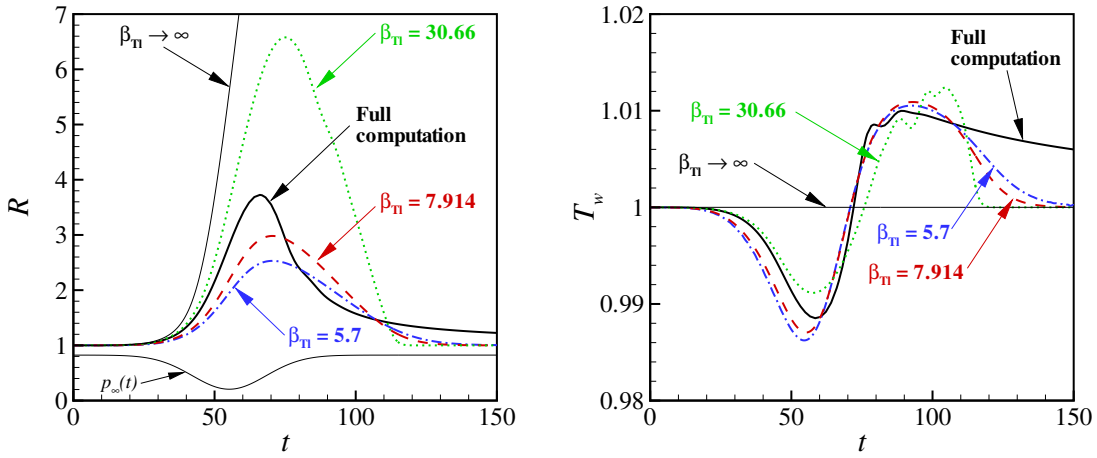

(a) Bubble radius

(b) Bubble wall temperature

Figure 3.18: Bubble radius, R, and bubble wall temperature, T_w, computed with full computation and the hot liquid model with four different values of β_{T_l}, for a gas-vapor bubble in a hot liquid. [Run 40,100(95)].

Chapter 4

Conclusions

This chapter contains a summary of the contributions of Part I of this thesis, along with some suggestions for future study.

4.1 Summary

We have performed an extensive set of computations for spherical gas-vapor bubbles, with heat and mass transfer in both the gas and liquid phases. These simulations have been systematically employed to indicate that there is a large parameter space for which numerous approximations are valid. Specifically, for the air-water systems considered in the thesis, it was demonstrated that the effect of dissolved air in the liquid can be neglected for bubble motions of short to moderate duration. In addition, the liquid temperature field may be assumed constant if the ambient temperature is not too high. The finite rate of phase change at the bubble wall was shown to have negligible effect on the bubble dynamics, which enables one to assume the vapor to be in equilibrium at the wall. Finally, the homobarotropic assumption was validated, even during strong collapses where the Mach number approaches unity. These four approximations enable the removal of all the field equations in the exterior liquid field, and the reduction of the number of partial differential equations in the gas interior from four to two. This represents a significant reduction in the computational effort. While each of the approximations have been widely used in the past, they have often been done so without any numerical validation. The numerical validations presented

will provide more confidence in the use of the approximations: both in results of full computations where the approximations reduce numerical work, and in results of reduced-order models that are often based on an approximate set of equations.

The proper orthogonal decomposition (POD) has been successfully applied to the interior temperature and concentration fields. This enabled large data sets from numerous full computations to be reduced to just a few mode shapes, that contained all the essential features of the solutions to the diffusion equations. The nature of the mode shapes were found to primarily depend on the Peclet number. Low Peclet numbers resulted in distributions that vary over the entire bubble interior, and high Peclet numbers resulted in an almost uniform distribution, with variation only near the bubble wall.

A new *constant transfer* model of diffusive effects was presented. The constant transfer model was motivated by the POD results, that indicated the use of constant transfer coefficients for both the heat and mass transfer would be reasonable. These were used to close the set of model equations in lieu of solving the interior diffusion equations. The value of the constant transfer coefficients could be determined directly from the first POD mode, and were demonstrated to depend upon the Peclet number. Linear analysis of the diffusion equations was also presented as a means for determining the transfer coefficients, without the need for POD results. The model equations were demonstrated to become exact as the Peclet numbers tend to zero. The constant transfer model is very efficient, with only two ordinary differential equations being required to capture the diffusive effects. It is also of simple form, enabling it to be readily implemented into existing and future continuum computations.

The constant transfer model has been evaluated by comparison to full computations for a wide range of forcings and bubble motions. It was found to capture the bubble dynamics within the desired accuracy. In particular the amplitudes of bubble growths and rebounds were within a few percent of the full computations. As expected, the model was shown to work extremely well for low Peclet numbers. In addition, we assessed the accuracy of some existing reduced-order models by comparison to full computations. These other models often lead to inaccurate bubble

responses. The constant transfer model was consistently more accurate than the best of the other reduced-order models.

4.2 Suggestions for future work

The constant transfer model has been shown to work well for the moderate bubble growths that have been presented in this thesis. However, it has not been validated for the explosive bubble growths and violent collapses that may occur in practice. For example, in a lithotripter the bubble may grow three orders of magnitude larger than its initial size. Presently the full computation is not able to compute such large growths and the subsequent violent collapse. Efforts should focus on the development of more robust full bubble computations.

In addition, as the intensity of the bubble collapse increases, the effect of liquid compressibility, variable gas transport properties and non-ideal gas behavior may become important issues. Future full bubble computations should include such effects to enable a systematic study to determine when these effects become important in terms of impacting the bubble dynamics.

Part II

Unsteady bubbly cavitating nozzle

Chapter 5

Introduction

The first model of two-phase flow through a converging-diverging nozzle was proposed by Tangren, Dodge & Seifert (1949). They employed a barotropic relation, which assumes that the fluid pressure is a function of fluid density only. This implies that the only effect of the disperse gas phase is to allow fluid compressibility which results in the bubbly mixture being treated as a single-phase compressible fluid. Brennen (1995) provides a general discussion of the barotropic model, as well as a summary of the work of Tangren et al. (1949).

Bubble dynamics are neglected by the barotropic model, but are thought to significantly alter the flow in cavitating nozzles, even in the mean. Wang & Brennen (1998) applied a nonlinear continuum bubbly mixture model (van Wijngaarden 1968, van Wijngaarden 1972, Biesheuvel & van Wijngaarden 1984) to the computation of the steady flow through a converging-diverging nozzle. This model incorporates the Rayleigh-Plesset equation to predict bubble size and growth as a function of position and time. Wang & Brennen found two different steady-state flow regimes to exist, and termed them *quasi-steady* and *quasi-unsteady*. The former is characterized by bubble growth that is induced by the low pressure region in the nozzle contraction, followed by a series of bubble collapses and rebounds downstream of the contraction. The quasi-unsteady solutions correspond to *flashing* flow. Varying the upstream conditions causes the flow to bifurcate from one regime to the other. The bifurcation of the steady-state equations has been studied by Delale, Schnerr & Sauer (2001).

To illustrate the two regimes, the method of Wang & Brennen is applied to a nozzle

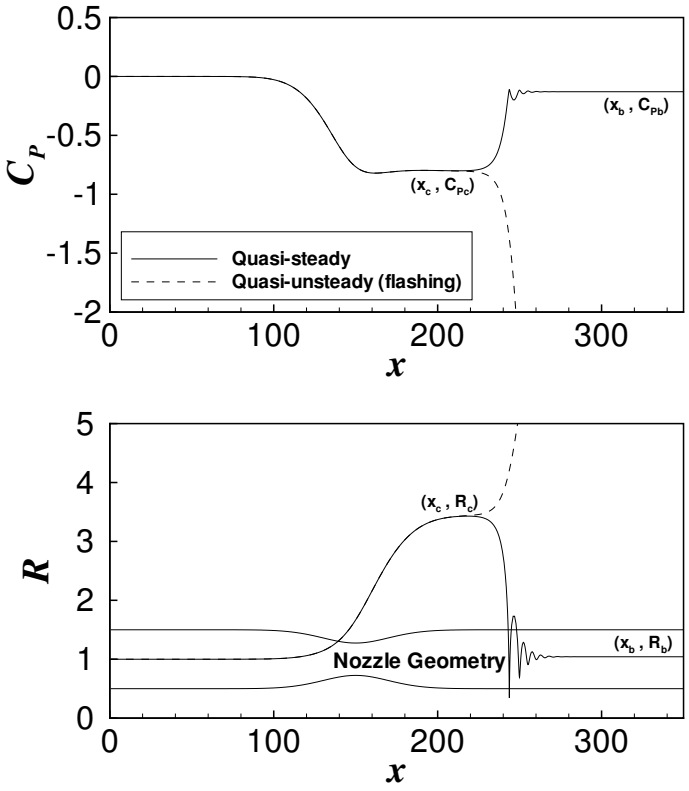

Figure 5.1: The pressure coefficient and bubble radius for two steady computations. Solid line is *quasi-steady* ($\sigma = \sigma^{+}_{crit}$), dashed line is *quasi-unsteady* or *flashing* ($\sigma = \sigma^{-}_{crit}$). The cavitation number is defined as, $\sigma = (p'_0 - p'_v)/\frac{1}{2}\rho'_L u'^2_0$, where p'_v is the vapor pressure of the liquid, p'_0 and u'_0 are the upstream pressure and velocity, and ρ'_L is the liquid density.

with a gentle contraction, depicted in Figure 5.1. Wang & Brennen investigated the bifurcation by varying the inlet void fraction; here we vary the cavitation number, σ, and achieve a similar result. Figure 5.1 presents the computed steady-state solutions for the pressure and bubble radius for cavitation numbers either side of the critical bifurcation value. The solid and dashed lines correspond respectively to the quasi-steady and quasi-unsteady solutions.

It is apparent in Figure 5.1 that the flashing solution has unbounded bubble growth which results in a physically unrealistic downstream pressure. Physically realizable steady-state solutions do not exist in this flow regime, and hence an *unsteady* code is required to examine these flows. Ishii, Umeda, Murata & Shishido (1993) proposed an unsteady bubbly flow model for the study of flows through a convergent-divergent

nozzle. However, by assuming that the pressure inside the bubbles is equal to the ambient fluid pressure, they neglected the bubble dynamics which are important in the cavitating nozzle flow. Chen & Heister (1996) incorporated bubble dynamics into the computation of bubbly flow through a nozzle by using a form of Rayleigh-Plesset equation that was modified to allow for high void fractions (Kubota, Kato & Yamaguchi 1992). However, the nozzle flow was not the focus of their work and was only studied in non-cavitating regimes for the purpose of demonstrating grid convergence.

The motivation of Part II of this thesis is to investigate the cavitating regimes where steady-state computations predict a physically unrealizable flashing solution. An unsteady quasi-one-dimensional code, based on the bubbly flow model used by Wang & Brennen, is employed to demonstrate that physically realizable solutions in the flashing regime involve *unsteady* bubbly shock waves propagating downstream from the nozzle contraction. An important restriction of the present results is that an *ad hoc*, but computationally fast, model is used for diffusive damping of the bubble radial motion. Delale (2002) employed a complicated model for thermal damping that indicated the steady-state computations are stabilized by thermal damping. However, the thermal model that they used has not been validated by comparison to full bubble computations. We employ the diffusive model of Part I to show that diffusive damping has only a minor impact on the stability of steady-state computations, if realistic treatments of diffusive damping are used. In addition, we demonstrate that the basic features of the nozzle flow are independent of the damping mechanisms.

5.1 Overview of contributions of this work

The main contributions of Part II of this thesis are as follows:

- Robust computation of *unsteady* bubbly cavitating nozzle flow.
- Demonstration that the physically realizable solution in the steady-state *flashing* regime involve *unsteady* bubbly shock waves propagating in the nozzle.

- Evaluation of the role of diffusive damping of bubble radial motions in the nozzle flow.

- Demonstration of agreement of the computation with two sets of experiments.

In Chapter 6 we present the model equations for the unsteady bubbly nozzle flow. In addition, the numerical method that we use to solve the equations, as well as grid convergence studies are presented.

The computations of unsteady bubbly shock waves propagating down a nozzle are presented in Chapter 7. Discussion on choking at the nozzle throat, and the critical back pressures that are required to cause the choking follows. The important role of effective damping is assessed, before comparing the bubbly model to a barotropic model.

Chapter 8 compares the bubbly computation to experiments of cavitating nozzles in both steady and unsteady situations, and for flows both with and without shocks.

Chapter 6

The model and numerical method

6.1 Model equations for nozzle flow

We consider a homogeneous* continuum bubbly mixture model that was first proposed by van Wijngaarden (1968, 1972). The model starts with the conventional quasi-one-dimensional continuity and momentum equations for flow of a compressible fluid through a nozzle,

$$\frac{\partial}{\partial t}(\rho A) + \frac{\partial}{\partial x}(\rho u A) = 0, \tag{6.1}$$

$$\rho \frac{Du}{Dt} + \frac{1}{2}\frac{\partial C_P}{\partial x} = 0. \tag{6.2}$$

Note that the viscous terms and gravity have been neglected in the momentum equation. The two-phase bubbly mixture is now assumed to be made up of an incompressible liquid phase with a dilute gas phase consisting of many spherical bubbles. By assuming that the flow properties vary on length scales that are large compared to the bubble radius and noting that the gas phase is restricted to being dilute we can, at any point in the flow, relate the local bubble radius to the local pressure by the Rayleigh-Plesset equation,

*Applying an order of magnitude analysis (Brennen 1995) indicates that, for the present nozzle flows, relative motion of the two phases can be neglected.

$$R\frac{D^2R}{Dt^2} + \frac{3}{2}\Big(\frac{DR}{Dt}\Big)^2 + \delta_D\frac{1}{R}\frac{DR}{Dt} + \frac{2}{We}\Big[R^{-1} - R^{-3k}\Big] + \frac{\sigma}{2}\Big[1 - R^{-3k}\Big] + \frac{C_P}{2} = 0. \tag{6.3}$$

The bubble population per unit liquid volume is fixed (neither fission nor fusion occur), so that the following relation between the mixture density and bubble radius holds,

$$\rho = \Big[1 + \frac{\alpha_0 R^3}{1-\alpha_0}\Big]^{-1}, \tag{6.4}$$

where α_0 is the initial volume void fraction. Equations (6.3) and (6.4) dynamically relate the mixture density to the mixture pressure. These two equations effectively replace the usual barotropic relation used for single phase flows, and allow the set of equations to be closed.

In equations (6.1) to (6.4) ρ is the mixture density made dimensionless by the constant liquid density, ρ'_L. The length and velocity scales used for non-dimensionalization are the equilibrium bubble radius, R'_0, and the nozzle inlet velocity, u'_0. The pressure coefficient is defined as $C_P = (p' - p'_0)/\frac{1}{2}\rho'_L u'^2_0$, where p'_0 is the upstream pressure. The cavitation number is defined as $\sigma = (p'_0 - p'_v)/\frac{1}{2}\rho'_L u'^2_0$, where p'_v is the vapor pressure of the liquid. The Weber number is given by $We = \rho'_L R'_0 u'^2_0/S'$, where S' is the (constant) surface tension. The use of the polytropic index, k, which varies from unity for isothermal flow to the ratio of the specific heats of the gas phase for adiabatic flow, assumes that the bubble contents are fully mixed. This assumption combined with the use of an *effective damping*, δ_D, to account for both viscous and diffusive contributions to damping of bubble radial motions, circumvents the need for solving unsteady diffusion equations at the scale of the bubble at every point in the flow.

The effective damping parameter, δ_D, is simply an alternative notation for the use

of an effective liquid viscosity described in Part I. In fact, δ_D may be written as

$$\delta_D = \frac{4}{Re}, \tag{6.5}$$

where, $Re \equiv u_0' R_0' / \nu_{eff}'$, is the often used Reynolds number, and ν_{eff}' is the effective liquid viscosity. Hence δ_D is clearly related to the dimensionless effective viscosity, $\nu \equiv \nu_{eff}'/\nu_L'$, defined in Part I. In Part II we use δ_D to notate the effective damping, except for in Section 7.4, where the impact of the use of effective damping is discussed, and recourse is made to the parameter ν.

The nozzle area, A, is nondimensionalized by the inlet area, A_0'. Since viscous terms are neglected, A_0' does not appear as a parameter of the computation; only the axial area variation of the nozzle is relevant. Parenthetically, for comparisons to real experimental nozzles it is required that $\sqrt{A_{min}'} \gg R_{max}'$ for the continuum approximation to hold.

6.2 Numerical method

Equations (6.1) through (6.4) are integrated using a one-dimensional Lagrangian finite volume scheme. This formulation allows the substantial derivatives to be treated as ordinary derivatives, and hence the Rayleigh-Plesset equation can be integrated as an ordinary differential equation. Consider a quasi-one-dimensional nozzle divided longitudinally into $N-1$ control volumes. Denoting the position of the control volume faces as x_j $(j = 1, 2, \ldots, N)$, we can define the nozzle areas and their derivatives at these positions,

$$A_j = A(x_j), \tag{6.6}$$

$$\frac{dA_j}{dx} = \frac{dA}{dx}(x_j), \tag{6.7}$$

where $A(x)$ and $dA(x)/dx$ are known functions. Each control volume face moves at the local fluid velocity and therefore

$$\frac{dx_j}{dt} = u_j, \tag{6.8}$$

where u_j is shorthand for $u(x_j(t), t)$. Integrating equations (6.1) and (6.2) over the control volumes we obtain, for $j = 1, 2, \ldots, N-1$,

$$\begin{aligned} \frac{d}{dt}\int_{x_j}^{x_{j+1}} \rho A dx &= 0, & (6.9)\\ 2\frac{d}{dt}\int_{x_j}^{x_{j+1}} \rho u A dx &= A_j C_{P_j} - A_{j+1} C_{P_{j+1}} + \int_{x_j}^{x_{j+1}} C_P \frac{dA}{dx} dx. & (6.10) \end{aligned}$$

Equations (6.9) and (6.10) respectively describe the rate of change of the total mass and momentum in the j^{th} control volume. Also, equation (6.3) can be split into two first-order equations at each face ($j = 1, 2 \ldots, N$),

$$\frac{dR_j V_j}{dt} + G_j + \frac{C_{P_j}}{2} = 0, \tag{6.11}$$

$$\frac{dR_j}{dt} - V_j = 0, \tag{6.12}$$

where,

$$G_j = \frac{V_j^2}{2} + \delta_D \frac{V_j}{R_j} + \frac{2}{We}\Big[R_j^{-1} - R_j^{-3k}\Big] + \frac{\sigma}{2}\Big[1 - R_j^{-3k}\Big]. \tag{6.13}$$

Finally, the density and bubble radius at the faces are related by

$$\rho_j = \Big[1 + \frac{\alpha_0 R_j^3}{1 - \alpha_0}\Big]^{-1}. \tag{6.14}$$

To integrate this system of (as yet exact) equations, it remains to approximate the integrals in equations (6.9) and (6.10). A second-order approximation is used,

$$\int_{x_j}^{x_{j+1}} f dx \;=\; \frac{\Delta x_j}{2}(f_j + f_{j+1}) + O(\Delta^3), \tag{6.15}$$

where $\Delta x_j \equiv x_{j+1} - x_j$, and f is any of ρA, $\rho u A$, or $C_P \frac{dA}{dx}$.

Equations (6.6) to (6.14) are $8N - 2$ ordinary differential equations for $8N$ unknowns ($\rho_j, R_j, V_j, C_{P_j}, u_j,\ A_j, dA/dx_j$, and x_j at the edges of the control volumes, $j = 1, 2, \ldots, N$). Specifying both of the boundary pressures, C_{P_1} and C_{P_N} closes the system. Alternative boundary conditions, such as the non-reflective boundary condition developed by Colonius, Brennen & d'Auria (1998) and Colonius et al. (2000), and the impedance boundary condition used in Section 8.2.1, have also been successfully implemented.

The equations are solved in the Lagrangian coordinate system, whereas the nozzle boundary conditions should be implemented in an Eulerian coordinate system. To circumvent this situation a special control volume with a fixed upstream face and a moving downstream face is used at the upstream boundary. Hence we replace equation (6.8) for the $j = 1$ case with $x_1 =$ constant. Additional flux terms are also added to equations (6.9) through (6.12). It is clear that the control volume will become very large as the downstream face is convected away from the stationary upstream face. Re-meshing is required to ensure that the accuracy of equation (6.15) is maintained. This is achieved by simply splitting the control volume into two as necessary as the computation proceeds. Maintaining consistency with the order of approximation of equation (6.15), variable values at the new face are obtained by linearly interpolating from values at either side. As a new control volume is created at the upstream boundary a control volume is removed from the downstream boundary. Hence the downstream boundary is only approximately fixed in position, with fluctuations caused by the truncations as well as net expansions or compressions of the fluid over the entire domain. In practice the downstream boundary is positioned far enough

from the nozzle contraction that, after initial transients, there are no appreciable gradients in the solution near the boundary, so that the exact location of the boundary is not important.

The discretized equations have similar properties to those arising in earlier work (Colonius et al. 1998, 2000) that examined the generation of bubbly shocks by an oscillating plane boundary. That is, they are stiff, and do not conserve mass precisely when an explicit time marching scheme is used. Hence an implicit Euler method is used for the basic time advancement. This is combined with a Richardson extrapolation method (Hairer & Wanner 1996, Press et al. 1994). The basic premise of the method is to compute a series of predictions for the solution at the new time level based on different numbers of subdivisions of the time interval. The series of predictions is then used to extrapolate to the limit of zero time step, and to provide an error estimate for the integration. The overall time step is adjusted based on the number of subdivisions and the error estimate.

The basic time advancement of the extrapolation method is the implicit Euler method. Using the integration scheme on equations (6.8) to (6.12) and going through the algebra, we can reduce the number of independent variables to $2N$ resulting in equations of the form,

$$F_j(X_k^{n+1}) = 0, \quad j = 1, \ldots, 2N, \quad k = 1, \ldots, 2N, \tag{6.16}$$

where $\vec{X} \equiv [u_1, R_1, x_2, R_2, x_3, R_3, \ldots, x_N, R_N]$. In each equation F_j, various parameters of the problem also appear as well as the fields from previous time levels. Newton's method is used to solve the nonlinear equations. The system of equations (6.16) results in a six-banded Jacobian matrix, enabling relatively efficient solution.

Grid convergence studies were conducted for flows in the regime where a steady bubbly shock wave stands in the diverging portion of the nozzle. For each of the three different grid resolutions the back pressure was lowered to initiate the flow, and the computation was performed until steady-state was reached. Figure 6.1 presents the

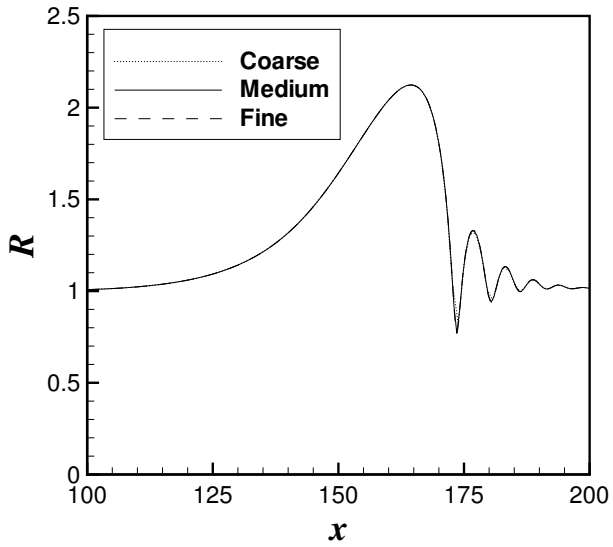

Figure 6.1: The bubble radius computed with the unsteady nozzle code for three different grid resolutions. Grid independence is demonstrated by the solutions for the two most refined grids being virtually identical.

computed bubble radius for the different grid resolutions. The medium and fine grids are indistinguishable indicating that the solution is mesh-independent. The coarse grid is slightly different in the first two collapses because it is not quite fine enough to fully resolve the series of bubble rebounds and collapses following the bubbly shock. In the remainder of the thesis all results presented have enough grid points to fully resolve the bubbly shock structure.

Chapter 7

Results

The non-dimensional parameters that are chosen to be studied are $\alpha_0 = 10^{-2}$, $We = 117$, $\delta_D = 0.43$, $k = 1.4$ (adiabatic) and σ ranging from about 0.93 to 1.20. These correspond to atmospheric pressure at the nozzle inlet ($p'_0 = 101.3kPa$) with water at 20°C ($\rho'_L = 1000kg/m^3$, $S' = 0.073N/m$, $p'_v = 3.5kPa$) and air bubbles of equilibrium radius, $R'_0 = 10^{-4}m$, with inlet velocity, u'_0, ranging from 12.7 to $14.5m/s$. The value of δ_D is chosen to achieve realistic solutions with only a few bubble rebounds. It is shown later that for an effective damping less than about 0.5 the macroscopic flow properties are independent of the effective damping. The nozzle has a Gaussian area variation given by

$$A(x) = 1 - (1 - A_{min})e^{-(\frac{x-x_0}{w})^2}, \tag{7.1}$$

and for the present study we focus on the values $A_{min} = 0.75$, $x_0 = 150.0$, $w = 30.0$.

7.1 Flow regimes

A series of computations are performed where the back pressure is varied over a wide range. As the back pressure is changed we obtain different mass flow rates through the nozzle, and hence the cavitation number is also varying.

The computed pressure, bubble radius and flow velocity for a typical set of com-

putations are presented in Figure 7.1. The solid lines represent final steady-state solutions (obtained by computing until steady-state is reached), while the dashed lines represent instantaneous flow fields as an unsteady shock wave travels downstream through the nozzle.

It is seen that much like the quasi-one-dimensional nozzle flows for a perfect gas, different regimes exist depending upon the value of the back pressure (or cavitation number). These regimes are

(i) Steady solution with no shocks ($0 > C_{Pb} > C_{Pcrit_1}$)

Recall that for any *inviscid* flow in a nozzle with equal inlet and outlet areas (such as the one being examined) that no steady-state, shock free solutions exist for a non-zero pressure drop. If a pressure drop is applied the flow will accelerate until it becomes choked at the throat. A shock will then form in the diverging section of the nozzle, with its position depending upon the value of the pressure drop. The entire total enthalpy drop is achieved over the shock, with all other parts of the flow remaining isentropic.

In the present bubbly model there is no macroscopic viscosity of the fluid, but there are losses associated with the bubble dynamics. These are accounted for by the effective damping, δ_D, in the Rayleigh-Plesset equation. Provided that the effective damping is not zero, then for a small pressure drop a steady-state, shock free solution is obtained. One such solution is plotted as curve (i) in Figure 7.1. It is apparent that there is only small growth of the bubble radius, and no collapses and rebounds.

(ii) Stationary shock in diverging section of nozzle ($C_{Pcrit_1} > C_{Pb} > C_{Pcrit_2}$)

The pressure drop is now large enough to cause choking at the throat and the formation of a steady bubbly shock wave in the diverging section of the nozzle. Curve (ii) represents one such solution. The bubbly shock structure is most apparent in the graph of the bubble radius, which shows the characteristic bubble growth followed by a succession of collapses and rebounds. The pressure

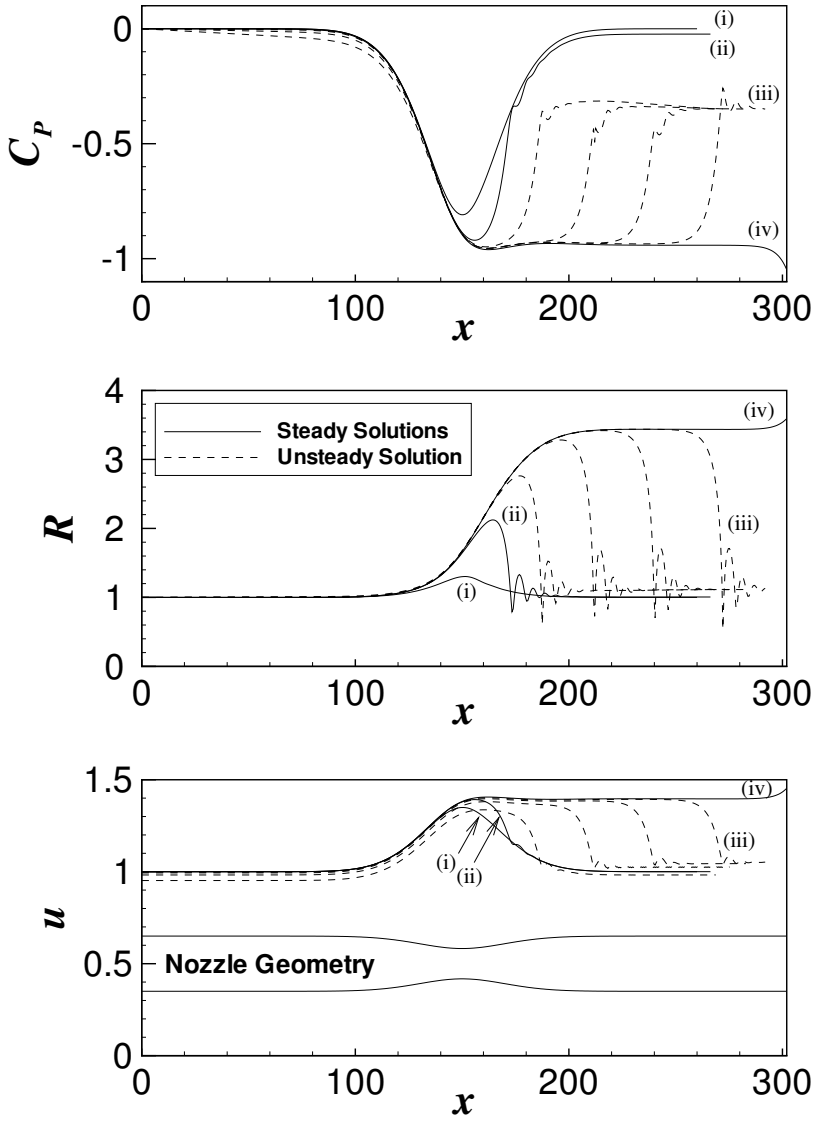

Figure 7.1: The pressure coefficient, bubble radius and flow velocity for four different back pressures (and cavitation numbers). (i) Steady-state solution with no shocks ($\sigma = 1.20$), (ii) Shock standing in diverging section of nozzle ($\sigma = 0.940$), (iii) Unsteady shock traveling down nozzle ($\sigma = 0.932$), (iv) Steady-state solution with expansion near nozzle exit ($\sigma = 0.937$). (All computations have $\alpha_0 = 10^{-2}$, $We = 117$, $\delta_D = 0.43$.)

in this case also exhibits a relatively sharp recovery associated with the bubbly shock wave.

It would be expected that the shock position would be a function of the back pressure in a manner analogous to the gas dynamics case. This is shown to be the case in Section 8.2, where the computed shock position is compared with experimentally observed shock positions.

(iii) Unsteady shock traveling down nozzle ($C_{Pcrit_2} > C_{Pb} \gtrsim -\sigma$)

The pressure drop is now large enough to cause the bubbly shock wave to move out of the diverging section and propagate downstream. The dashed curves of Figure 7.1 show the solution at four different times. The time interval between each curve is constant, so it is evident that the propagation speed of the bubbly shock is approximately constant.

It is also interesting to note that while the structure of the shock in terms of the bubble radius and flow velocity remains essentially the same at each time instant, the structure in terms of the pressure does not. This is apparent in the last of the instantaneous curves which shows a larger pressure peak at the position of first collapse. In actuality similar pressure peaks manifest themselves at other earlier instances in the computation, but by coincidence the time instances shown on the plot do not exhibit these. Studying similar plots with a far higher temporal resolution indicates that the magnitude of the pressure peak at first collapse in fact oscillates in time, probably due to acoustic waves reflecting between the shock and the boundary. The pressure is far more sensitive to these waves than either the bubble radius or flow velocity.

Given the upstream and downstream radius, as well as the upstream pressure, equation (6.69) of Brennen (1995) can be used to compute the speed of the one dimensional shock. This was done for the case illustrated with favorable comparisons. However, the computed shock speed is very sensitive to the value of upstream pressure that is used; indeed it is possible to compute a shock speed of zero with only the smallest of changes to the upstream pressure.

It is likely that within this range of back pressures it is physically possible to have a final *steady-state* solution where the flow in the nozzle is "over-expanded", and the increase to the back pressure takes place across a system of compressions and expansions outside the nozzle.

(iv) Steady, under-expanded flow ($C_{Pb} \lesssim -\sigma$)

Now the back pressure is low enough to allow the shock to pass through the downstream boundary and out of the computational domain. The flow in the nozzle is "under-expanded" and expands near the end of the nozzle to match the back pressure. This is apparent in curve (iv) of the pressure plot in Figure 7.1, which shows the expansion taking place near the domain boundary. The flashing solution of Figure 5.1 is one of these solutions, albeit with an unrealistically low back pressure.

If we choose the back pressure to match the pressure upstream of the shock wave (that is, $C_{Pb} \approx -\sigma$), then there would be no such expansion. This corresponds to the "perfectly expanded" solution of the flow of a perfect gas.

Calculations with a lower void fraction of $\alpha_0 = 10^{-3}$ were performed to evaluate the effect of void fraction on the various regimes discussed above. Figure 7.2 presents the bubble radius for this series of computations. Once again the solid lines correspond to steady solutions while the dashed lines represent a time series of the unsteady solution. The behavior is qualitatively similar to that of the higher void fraction computations. As expected, the lower void fraction results in higher maximum bubble radius and hence more violent collapses.

7.2 Choking

As the cavitation number is decreased, the back pressure will also decrease naturally until, eventually, the flow becomes choked. The decrease of the cavitation number can be considered as a combination of two physical changes to the flow; decreasing the inlet pressure, p_0', and/or increasing the inlet velocity, u_0'. If we consider situations

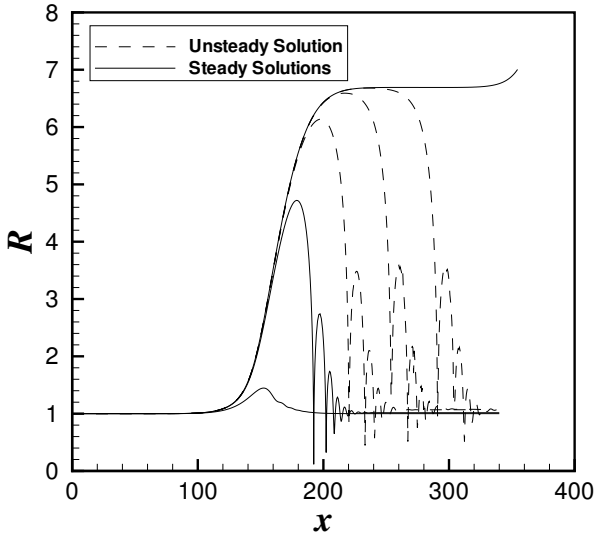

Figure 7.2: The bubble radius for a set of calculations with lower void fraction ($\alpha_0 = 10^{-3}$, $\sigma = 0.688$ to 1.000, $We = 159$, $\delta_D = 0.37$). The same four regimes that existed for the higher void fraction flow are illustrated.

where the inlet pressure is fixed then only the inlet velocity is changing, and from the definition of the cavitation number,

$$u_0' = \left[\frac{p_0' - p_v'}{\frac{1}{2}\rho_L'\sigma}\right]^{\frac{1}{2}}. \tag{7.2}$$

The dimensional mass flow rate is given by

$$\begin{aligned} \dot{m}' &= \rho_0' u_0' A_0' \\ &= \rho_L'(1-\alpha_0) u_0' A_0'. \end{aligned} \tag{7.3}$$

Substituting equation (7.2) into equation (7.3), non-dimensionalizing by the choked mass flow rate, and canceling all the constant inlet conditions yields the following simple equation for the non-dimensional mass flow rate,

$$\dot{m} \equiv \frac{\dot{m}'}{\dot{m}'_{crit}} = \left[\frac{\sigma_{crit}}{\sigma}\right]^{\frac{1}{2}}, \tag{7.4}$$

where, σ_{crit} is the cavitation number at choking.

Many calculations of the steady flow solution were carried out with varying cavitation numbers. Figure 7.3 plots the non-dimensional mass flow rate (computed by equation (7.4)) versus the back pressure which is obtained as a result of each calculation. Results with effective dampings ranging from 0.22 to 0.85 are shown. It is interesting to note that the variation of effective damping does not affect the critical choking back pressure. This is discussed further in Section 7.3. As expected, for a given back pressure, cases with a smaller effective damping have a larger mass flow rate.

Figure 7.4 presents the bubble radius for four different back pressures indicated by (i)-(iv) in Figure 7.3. Curve (i) in Figure 7.4 illustrates that for small pressure drops there are no bubble collapses or rebounds. This accounts for the straight sections of the curves in Figure 7.3. For larger pressure drops bubble collapses and rebounds become apparent (curve (ii) in Figure 7.4). This increases the losses in the system and hence causes the curved sections in Figure 7.3. This smooth transition to choked flow continues as the pressure drops become larger and the bubble dynamics become more pronounced (curve (iii) in Figure 7.4), until eventually the flow chokes and a bubbly shock wave forms (curve (iv) in Figure 7.4).

7.3 Critical back pressures

For a particular set of flow parameters it would be useful to be able to predict the back pressure at which the flow chokes and shocks form (C_{Pcrit_1}), as well as the back pressure at which the shock becomes unsteady and begins traveling downstream through the constant area portion of the nozzle (C_{Pcrit_2}). The first transition is difficult to analyze since it is not clear when a series of bubble collapses and rebounds

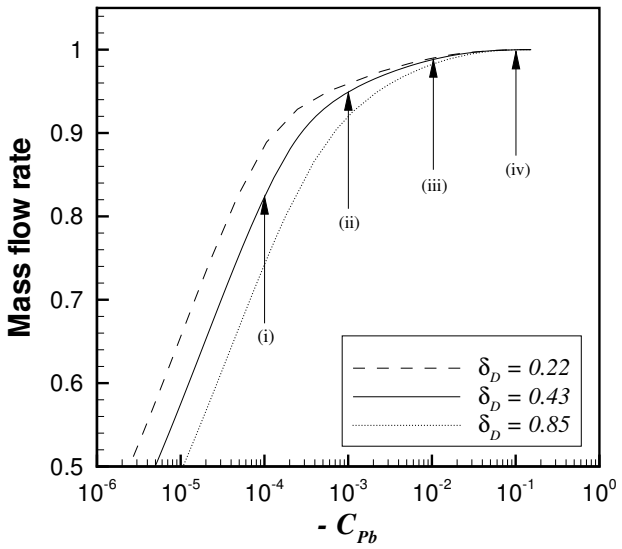

Figure 7.3: Non-dimensional mass flow rate as a function of back pressure coefficient for different values of effective damping, δ_D, in the range 0.22 to 3.78 ($\alpha_0 = 10^{-2}$, $We = 117$).

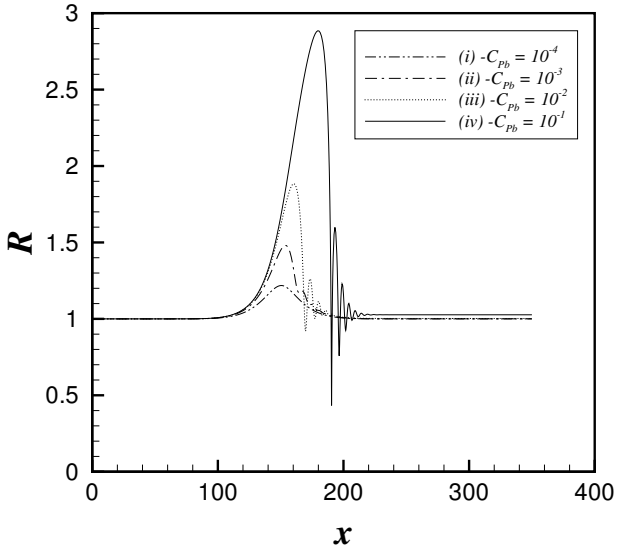

Figure 7.4: The bubble radius computed for the four back pressures indicated in Figure 7.3 ($\delta_D = 0.43$, $\alpha_0 = 10^{-2}$, $We = 117$).

become a bubbly shock, and the finite thickness of a bubbly shock wave means that the nozzle area change that occurs over the shock thickness cannot be neglected. However, the second transition occurs in the constant area part of the nozzle and enables the one-dimensional jump conditions to be used to predict C_{Pcrit_2}.

Consider the typical steady bubbly shock wave shown in Figure 5.1. Integrating the steady forms of equations (6.1) and (6.2) from the position of critical radius upstream of the shock (x_c), to a position well downstream of the shock (x_b) yields

$$\rho u A\Big|_{x=x_c}^{x=x_b} = 0, \tag{7.5}$$

$$A(2\rho u^2 + C_P)\Big|_{x=x_c}^{x=x_b} - \int_{x_c}^{x_b} C_P \frac{dA}{dx} dx = 0. \tag{7.6}$$

Also note that at positions x_c and x_b the derivatives with respect to x vanish, so that for the steady flow the Rayleigh-Plesset equation reduces to

$$C_P(R_{c,b}) = -\sigma\Big[1 - R_{c,b}^{-3k}\Big] - \frac{4}{We}\Big[R_{c,b}^{-1} - R_{c,b}^{-3k}\Big]. \tag{7.7}$$

Substituting equation (7.7) into (7.6), and noting that the integral term in equation (7.6) vanishes because there is no area change between x_c and x_b, yields a nonlinear equation relating R_b to R_c. Noticing that for the current computations $R_b = 1 + R_b'$ where $R_b' \ll 1$, it is useful to linearize this equation with respect to R_b'. Neglecting terms higher than second-order, allows R_b' to be determined as an explicit function of R_c,

$$R_b' = \frac{h(R_c) - \rho_0}{3\alpha_0 h(R_c) - \omega_N^2}, \tag{7.8}$$

where,

$$\begin{aligned} h(R_c) &\equiv \frac{C_P(R_c)}{2} + \rho(R_c)u_c^2 \\ &= \frac{C_P(R_c)}{2} + \frac{\rho_0^2}{\rho(R_c)}, \end{aligned}$$

and ω_N is the bubble natural frequency which is computed by

$$\omega_N^2 \equiv \frac{3k\sigma}{2} + (3k-1)\frac{2}{We}.$$

Once R_b' is computed, the following variables can also be computed to first-order,

$$R_b = 1 + R_b', \tag{7.9}$$

$$C_{P_b} = -2\omega_N^2 R_b', \tag{7.10}$$

$$u_b = 1 + 3\alpha_0 R_b'. \tag{7.11}$$

Of course the present method requires knowledge of the critical radius R_c. It would be preferable to be able to predict the critical back pressure from knowledge of the flow parameters only. Wang & Brennen (1998) neglected the integral term of equation (7.6), and assumed that the critical bubble radius was large compared to the equilibrium radius to develop the simple approximate expression, $R_c = (\sigma/2\alpha_0)^{1/3}$. Applying the method to the computation of Figure 5.1 where $\sigma_{crit} = 0.932$ and $\alpha_0 = 10^{-2}$ yields $R_c = 3.598$, and $C_{Pb_{crit2}} = -0.035$. This is vastly different from the back pressure in Figure 5.1 which is -0.151. From the computation of Figure 5.1 we find that the critical radius is in fact 3.429 which is approximately 5% lower than that predicted by the method of Wang & Brennen. Using this value of R_c in equations (7.8) and (7.10) yields $C_{Pb_{crit2}} = -0.160$, which compares well with the value in Figure 5.1.

In order to obtain a reasonable estimate of the critical back pressure, it is therefore crucial to first obtain an accurate estimate of the critical radius. The most significant

source of error in Wang & Brennen's estimate of R_c is the neglect of the integral term of equation (7.6) when integrating from the initial condition through the nozzle contraction to the position of critical radius. Wang (1999) addresses this issue and formulates a complicated non-linear equation for R_c, which has to be solved numerically and is subject to a convergence condition. It is likely that this estimate would result in a better estimate of the critical back pressure.

It is important to note that the preceding analysis does not involve the effective damping. That is, the critical back pressure is independent of the effective damping used. This has already been observed in Section 7.2, where it was demonstrated that the onset of choking did not change when the effective damping was varied. The role of the effective damping is discussed more fully in the next section.

7.4 Effect of damping

The present model employs the use of an effective damping parameter to account for all radial damping mechanisms of the bubble motion. This is achieved by using a total "effective" liquid viscosity to include the contributions to damping from acoustic radiation and mass and thermal diffusion. Some analytical and empirical expressions for contributions to the total effective viscosity from viscous, acoustic and thermal effects are reviewed by van Wijngaarden (1972). Those estimates are generally based on low amplitude linear motions, such as the attenuation of sound waves, whereas in the nozzle flow there is strong bubble growth and collapse. Recent studies (Watanabe & Prosperetti 1994, Kameda & Matsumoto 1996, Matsumoto & Kameda 1996) have investigated the diffusive damping mechanism for non-condensible gas bubbles in the non-linear regime by numerically solving the full unsteady diffusion equations at the scale of the bubble. They indicate that the simple model that we have used may not be able to correctly capture the diffusive effects, which may have an impact on the structure of the bubbly shock waves. However other important damping effects, such as acoustic radiation and bubble fission, have not yet been fully addressed in any of the studies. We demonstrate the validity of our approach, first by showing that the

value of effective damping parameter used does not significantly affect the basic flow features, and then by accounting for diffusive damping by implementing the constant transfer model of Part I into steady-state computations.

Colonius et al. (2000) demonstrated that for low frequency forcing of bubbles it is relatively unimportant to model the detailed diffusive processes in the bubble. They demonstrated that the value of effective damping parameter used does not have a significant impact on the macroscopic flow field as long as it is below a critical value. Their result hinged on the fact that the dissipation associated with the shock jump conditions is much larger than, and independent of, the dissipation provided by any of the damping processes that are modeled by the effective damping. For the present nozzle flow being studied the independence of the shock jump conditions on the value of the effective damping have been previously observed in Sections 7.2 and 7.3. Moreover, we now demonstrate that for realistic values of effective damping that the basic flow features are also independent of the magnitude of the effective damping parameter so long as it is sufficiently small (in the asymptotic sense). A series of unsteady computations with effective damping ranging from 0.22 to 3.78 was performed. The initial values of the other parameters were held constant, but the final values of the parameters varied slightly due to the re-normalization with the inlet velocity. Figure 7.5 plots the bubble radius for each of these calculations at a time when the bubbly shock is propagating in the constant area section of the nozzle. For values of effective damping lower than about 0.5 the macroscopic behavior becomes independent of effective damping. That is, there is large growth of the bubble radius followed by a rapid collapse; the jump conditions across the shock are not significantly impacted by the value of effective damping. The main effect of decreasing the effective damping is to increase the amplitude and number of the bubble rebounds. For larger values of effective damping the bubble growth begins to be affected, eventually limiting the growth to the extent that there is no sharp collapse. For the results presented elsewhere in this paper the effective damping is chosen to be small enough so that the macroscopic flow properties are independent of decreases or small increases in the effective damping.

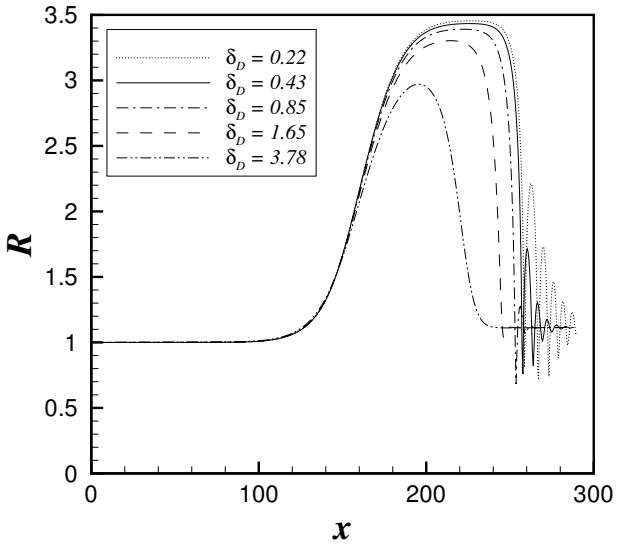

Figure 7.5: Bubble radius for a series of different values of effective damping, δ_D, in the range 0.22 to 3.78 ($\sigma = 0.76$ to 0.95, $-C_{P_b} = 0.27$ to 0.36, $We = 115$ to 153).

While we have demonstrated that the important features of the nozzle flow are independent of the value of effective damping, Delale (2002) claims that thermal damping can stabilize the *flashing* solutions obtained in a steady-state computation. Their model of heat transfer is based upon a series of complicated mathematical manipulations and approximations, and has yet to be validated by comparison to full bubble computations. We examine this possible stabilizing effect by implementing the validated constant transfer model of Part I into steady-state nozzle computations.

Figure 7.6 plots the bubble radius and pressure coefficient computed with the constant transfer model of Part I, the isothermal model (with and without effective damping) and the adiabatic model (without effective damping), for different values of σ. The nozzle geometry and inlet void fraction are the same as in the previous sections, while the liquid is water at 25°C and atmospheric pressure with air-vapor bubbles of equilibrium radius, $R_0' = 4 \times 10^{-5}$m. This results in the values of dimensionless parameters given in the figure. These are only approximate, since the computations were carried out under the non-dimensionalization of Part I, and then converted to the present non-dimensionalization by re-normalizing with the inlet velocity. The exact

values for the parameters, in both non-dimensionalizations, are given in Appendix D. As in Part I, the parameter $\nu \equiv \nu'_{eff}/\nu'_L$, represents the ratio of effective viscosity (which is chosen to match damping in linear analysis) to the actual liquid viscosity. Hence, for $\nu = 1$ the computation does not use an effective viscosity. The value of ν is directly related to the damping coefficient, δ_D, which as explained in Section 6.1 may be written in terms of a Reynolds number based upon the effective liquid viscosity.

For the high value of σ in (a), it is apparent the none of the respective models are close to the flashing instability. The isothermal model with an effective liquid viscosity ($\nu = 15$) shows fairly close agreement to the constant transfer model, while the computation without effective viscosity ($\nu = 1$) exhibits under damped rebounds. It is also apparent that the adiabatic model (used throughout Part II of this thesis) is not appropriate, since the slow initial growth is far closer to isothermal behavior. Nevertheless, the conclusions regarding the existence of unsteady bubbly shock waves in the nozzle will also remain valid in the isothermal case.

As σ is lowered slightly, the isothermal model without effective viscosity reaches the flashing solution limit as shown in (b). The isothermal model with effective viscosity and the constant transfer model both remain stable, until σ is lowered further in (c), at which point the isothermal model with effective viscosity also becomes unstable. Clearly, the use of effective viscosity in the isothermal model delays the onset of the flashing instability. Finally, a further decrease in σ results in the constant transfer model reaching the flashing instability limit as shown in (d). It is interesting to compare the bubbly shock structure of the constant transfer model in (d) to that of the isothermal model in (c). While the decay of the bubble rebounds in the shocks are different, they do not exhibit the vast differences in shock structure that were illustrated in some circumstances by Watanabe & Prosperetti (1994) and Kameda & Matsumoto (1996).

At first glance it appears that the diffusive damping has a significant impact on the nozzle flow, since it causes the onset of the flashing instability to be delayed. However, closer examination shows that this delay is minor, since the difference between the cavitation numbers at the onset of instability in the isothermal model [(b)] and at

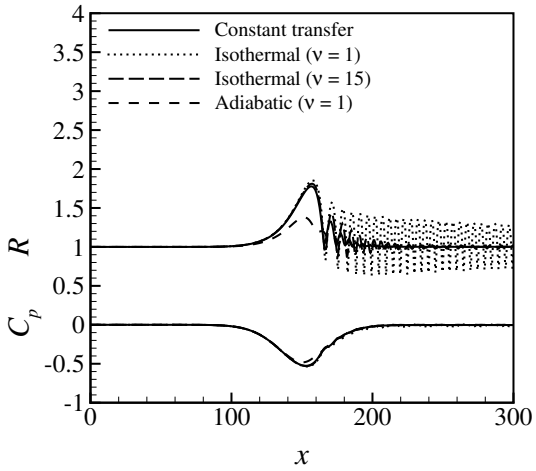

(a) $\sigma = 1.112$: All models sub-critical.

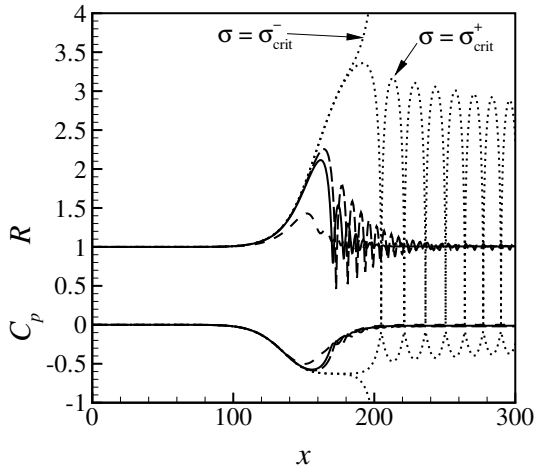

(b) $\sigma \approx 1.078$: Isothermal ($\nu = 1$) critical.

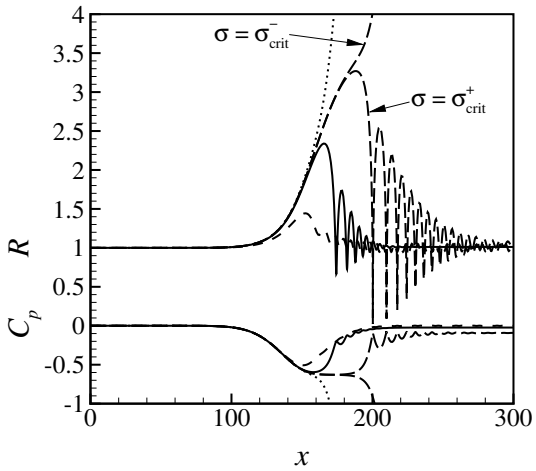

(c) $\sigma \approx 1.070$: Isothermal ($\nu = 15$) critical.

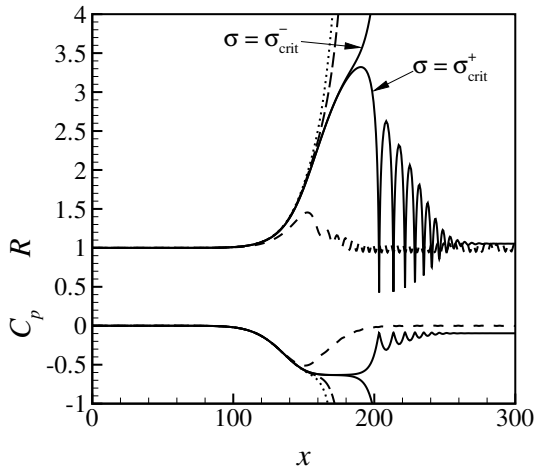

(d) $\sigma \approx 1.064$: Constant transfer model critical.

Figure 7.6: Bubble radius and pressure coefficient computed with various heat and mass transfer models for different values of σ. The constant transfer model (of Part I) uses $\beta_T = 7.35$ and $\beta_C = 7.01$. The nozzle geometry is the same as in Figure 7.1, while $\alpha_0 = 10^{-2}$, $We \approx 102$ and $\delta_D \approx 0.007$ (for $\nu = 1$), or $\delta_D \approx 0.1$ (for $\nu = 15$).

the onset of instability in the constant transfer model [(d)] is only about 1%. In addition, similar delays in the onset of the flashing instability occur as a result of using an effective viscosity, as illustrated in Figure 7.6 by comparing (b) and (c). Although the thermal damping mechanism proposed by Delale (2002) is shown to exist, the effect for realistic models of diffusive damping is unimportant, and can also be obtained using the crude effective viscosity model employed throughout Part II of this thesis.

7.5 Comparison to barotropic model

Barotropic results for isothermal ($k = 1$) nozzle flow were first reported by Tangren et al. (1949) and differs from the present model in that bubble dynamic effects are neglected; at every point in the barotropic flow the bubbles are in equilibrium with the local pressure. Brennen (1995) presents the barotropic results for any polytropic index, and non-dimensionalizing those equations for the case $k \neq 1$, and $u_0' \neq 0$ yields the following set of equations,

$$u = \frac{1-\alpha_0}{A(1-\alpha)}, \tag{7.12}$$

$$u^2 - 1 = \tilde{\sigma}\Big[1 - r^k - \frac{k}{k-1}\frac{\alpha_0}{1-\alpha_0}\Big\{1 - r^{k-1}\Big\}\Big], \tag{7.13}$$

$$C_P = \tilde{\sigma}\Big[r^k - 1\Big], \tag{7.14}$$

where r is defined as

$$r \equiv \frac{\alpha_0(1-\alpha)}{\alpha(1-\alpha_0)}, \tag{7.15}$$

and $\tilde{\sigma} = p_0'/\frac{1}{2}\rho_L' u_0'^2$ is a parameter which is the same as the cavitation number if $p_v' = 0$. Equation (7.12) represents continuity, equation (7.13) is the momentum equation that has been integrated using the barotropic relation given by equation (7.14). Substi-

tuting equation (7.12) into equation (7.13) yields an algebraic equation that can be solved for α if the nozzle area and initial void fraction is specified. The flow velocity and pressure can then be computed from equations (7.12) and (7.14), respectively.

Consider solving for α in the nozzle throat, where $A = A_{min}$. Equations (7.12) and (7.13) have either zero, one or two real roots, depending upon the value of $\tilde{\sigma}$. For high values of $\tilde{\sigma}$ there exist two real roots, corresponding to sub-sonic and supersonic conditions. Given that the initial condition is sub-sonic, only the sub-sonic root is valid for these conditions. As $\tilde{\sigma}$ is lowered the two roots approach each other until, for a particular critical value of $\tilde{\sigma}$, there is only the single sonic solution at the throat, corresponding to choked flow. For this $\tilde{\sigma}_{crit}$ the flow downstream of the throat can be either sub-sonic or supersonic, depending on the downstream boundary condition. For values of $\tilde{\sigma}$ below $\tilde{\sigma}_{crit}$, there are no solutions, indicating that no steady-state solutions exist.

It is useful to compare the results of the present paper (which we term the dynamic calculations) with those of the barotropic model. To compare the barotropic calculations we first proceed to find $\tilde{\sigma}_{crit}$ by trial and error. That is, $\tilde{\sigma}$ is varied until equations (7.12) and (7.13) have only the sonic root at the throat. The value of $\tilde{\sigma}_{crit}$ will depend only upon the initial void fraction, α_0, and throat area, A_{min}. For the computations of Figure 7.1 ($\alpha_0 = 10^{-2}$, $A_{min} = 0.75$) we find that $\tilde{\sigma}_{crit} = 1.011$. This is different to the critical cavitation number in Figure 7.1, which is $\sigma_{crit} = 0.937$. The difference of $\tilde{\sigma}_{crit} - \sigma_{crit} = 1.011 - 0.937 = 0.074$ is due to the (constant) vapor pressure, p'_v, of the liquid. It is chosen to keep this algebraic difference constant for comparisons at all values of σ. That is, to compare a barotropic calculation to a dynamic computation with a cavitation number of σ, we use $\tilde{\sigma} = \sigma + 0.074$.

The computed dynamic and barotropic pressures for three different cavitation numbers are presented in Figure 7.7. The upper graph presents comparisons for a flow that is far from critical (high cavitation number). The curves for the dynamic and barotropic calculations overlay each other indicating that for flows which are far from critical bubble dynamics are not important and the barotropic model is valid.

The middle graph compares the two models for a flow that is almost critical

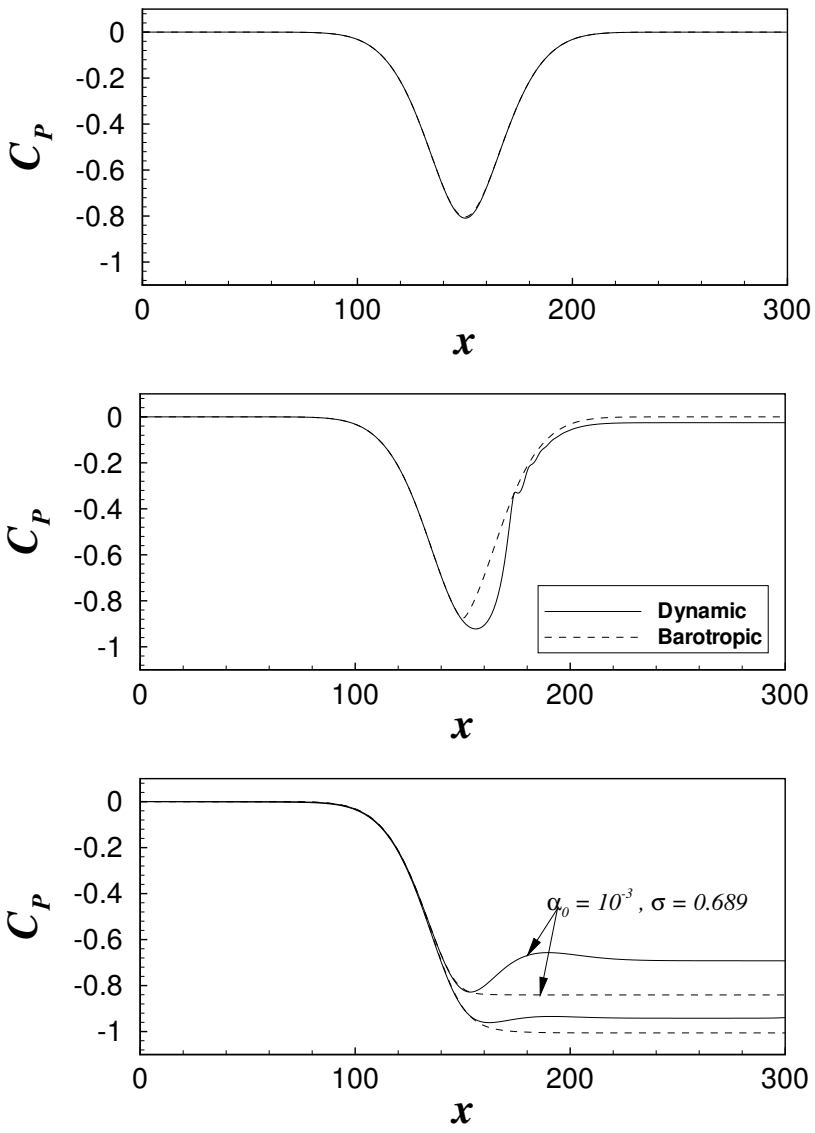

Figure 7.7: Comparison of pressures for dynamic and barotropic computations for $\sigma = 1.200$ (upper), $\sigma = 0.940$ (middle), and $\sigma = 0.937$ (lower). ($\alpha_0 = 10^{-2}$ unless otherwise specified.)

(cavitation number only slightly above critical). The agreement is good up until the throat, at which point the dynamic computation develops an asymmetry due to the radial inertia associated with the bubble growth. It is apparent that the barotropic model is no longer valid, due to the effects of bubble dynamics.

The lower graph presents comparisons for computations at the critical condition. Agreement is excellent up until just after the throat, at which point the pressure in the dynamic computation increases above the minimum value attained near the nozzle throat. The minimum pressure in the throat being lower than the back pressure is again caused by the radial inertia that the bubbles have as they approach the throat. The barotropic model is unable to model this behavior due to the neglect of bubble dynamics. Also presented in the lower figure is a comparison at critical condition for a lower initial void fraction of 10^{-3}. It is noted that the differences between the dynamic and barotropic models are greatest for the lower void fraction flow. This is consistent with the observation in Section 7.1 that lower void fraction computations have a higher maximum bubble radius and more violent bubble collapses.

Chapter 8

Comparison to experiments

8.1 Shock free steady flow

Here we will compare the results of the bubbly model with the experiments of Ishii et al. (1993) who measured the pressure, void fraction, and flow velocities of both the liquid and gas components at four locations in a steady nozzle flow, and compared them with their own bubbly flow model. Their model assumed that the pressure inside a bubble was equal to the ambient pressure, and hence neglected any of the bubble dynamics described by the Rayleigh-Plesset equation. They did however account for relative motion between the liquid and gas phases, which may be important to correctly predict the void fraction distribution in the nozzle.

The nozzle had an area that varied linearly to a throat with area ratio (relative to the inlet) of 0.375, and then expanded to an area ratio of 0.50 at the exit. The flow conditions were water at 20°C ($\rho'_L = 998kg/m^3$, $p'_v = 3.5kPa$, $S' = 0.073N/m$), with air bubbles with *average* equilibrium radius, $R'_0 = 10^{-4}m$, with inlet velocity, $u'_0 = 3.90m/s$, and inlet pressure, $p'_0 = 182kPa$. These conditions resulted in a cavitation number, $\sigma = 23.5$ and Weber number, $We = 20.7$. From the air and water mass flow rates that are provided, and assuming no relative motion at the inlet, it is possible to compute the inlet void fraction as approximately, $\alpha_0 = 0.039$.

Since the experimental data is only for a steady flow, a steady code based on that of Wang & Brennen (1998) is used to compute the solution. In addition the barotropic solution discussed in Section 7.5 is calculated. Figure 8.1 shows the comparisons of

the dynamic computation (solid lines) and the barotropic calculation (dashed lines) to the experimentally measured pressures, void fractions and velocities of Ishii et al. (1993). The maximum bubble growth in this flow is only about 7% which results in $\sqrt{A'_{min}}/R'_{max} = 124$, so the continuum approximation is valid. The small amount of bubble growth implies that bubble dynamics are not important for this flow. This accounts for the barotropic computation being almost identical to the dynamic computation. For flows nearing the critical regime, bubble dynamics become important and the dynamic and barotropic models obtain vastly different results.

Agreement of these models to the experimental pressure and liquid velocities is excellent, as it was also for the model of Ishii et al. The computed void fraction fares much worse. The only point of agreement is right in the throat itself, with the other points being considerably lower upstream of the throat and higher downstream of the throat. The considerably more complicated model of Ishii et al., which incorporates the relative motion of the phases, had reasonable success at matching the first and last experimental points, but significantly underestimated the void fraction at and immediately downstream of the throat. The more recent work of Wang & Chen (2002) uses a dynamic bubbly model that also accounted for phase relative motion, and obtained superior agreement to the experimental void fraction distribution.

8.2 Unsteady flows with shocks

Sandhu & Jameson (1979) performed experiments in a converging-diverging nozzle with equal inlet and outlet areas, and a throat area ratio of 0.132. The nozzle *diameter* varied linearly between the transitions, which meant the area varied quadratically. In the implementation of the unsteady code, the function describing the throat area was constructed of Gaussian and error functions to ensure that it was infinitely differentiable, even at the transitions. The amount of smoothing at the transitions was kept to a minimum so as to have minimal impact on the flow.

Sandhu & Jameson used a surfactant to reduce bubble coalescence and hence maintain a large proportion of very fine bubbles. The surfactant would reduce the

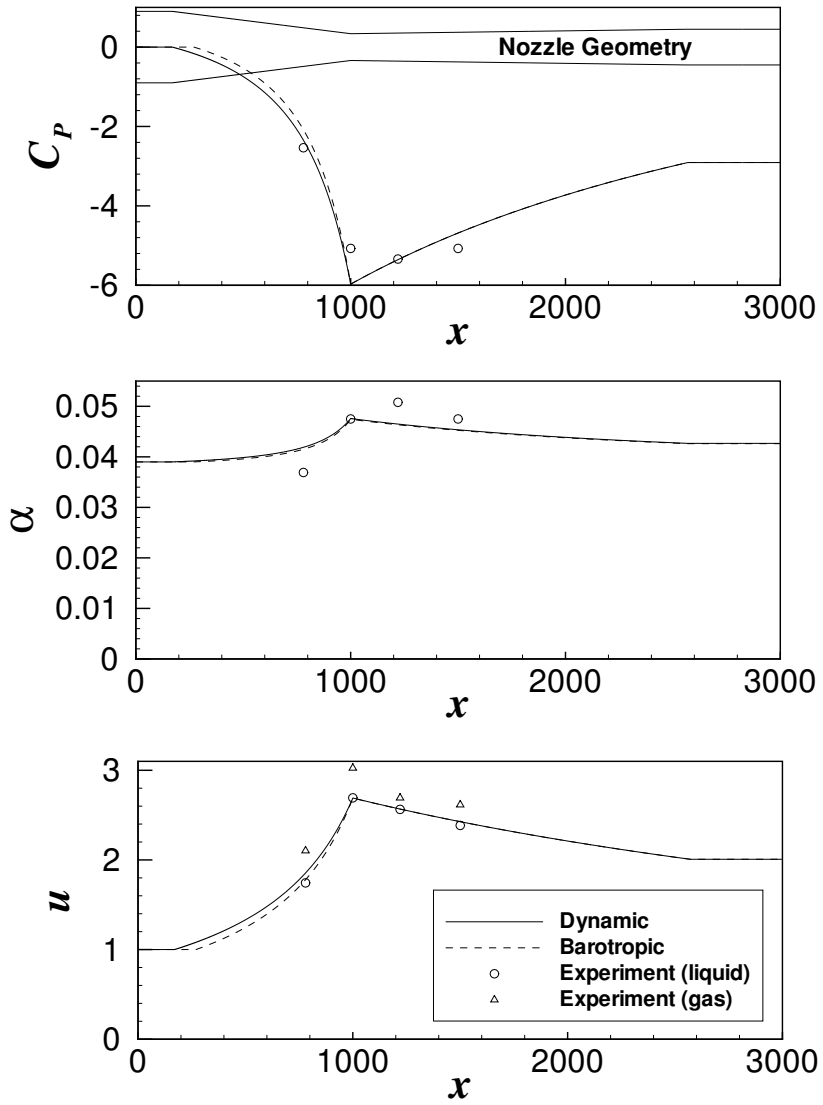

Figure 8.1: Comparison of Ishii et al.'s experimentally measured pressures, void fractions and velocities with barotropic and computed solutions ($\alpha_0 = 0.039$, $\sigma = 23.5$, $We = 20.7$, $\delta_D = 0.5$)

surface tension of the water, but in the absence of any data we use $S' = 0.073N/m$, which is the value for water at 20°C. Other flow conditions are, water with density and vapor pressure, $\rho'_L = 1000kg/m^3$ and $p'_v = 3.5kPa$, inlet pressure, $p'_0 = 214kPa$, and air bubbles with *average* equilibrium radius, $R'_0 = 6 \times 10^{-5}m$. The inlet velocity was not specified in Sandhu & Jameson, but from a range of volume flow rates it was possible to determine that the velocity ranged from 1.1 to $3.1m/s$. It was found by trial and error with the steady code that an inlet velocity of $u'_0 \approx 2.27m/s$ resulted in choked flow. The above values resulted in a cavitation number, $\sigma = 81.6$ and Weber number, $We = 4.1$. In calculations we use an effective damping of $\delta_D = 15.2$, which was determined to be "asymptotically small" according to the method discussed in Section 7.4.

Computations with different back pressures were performed. In each case as the back pressure was lowered the flow accelerated until at some instance the flow became choked and a bubbly shock wave formed in the diverging section of the nozzle. The position of the shock would oscillate about its steady-state position for a few cycles. Computations were carried out until it was clear where the final steady-state position of the shock was.

For these flows the maximum bubble growth was over 300% which results in $\sqrt{A'_{min}}/R'_{max} = 20$. The continuum approximation is probably still valid, but it should be noted that the dilute gas phase assumption is violated with void fractions as high as 25% being reached. Hence bubble-bubble interactions are important, and the Rayleigh-Plesset equation should be modified to account for this. Nevertheless, the upper plot of Figure 8.2 shows reasonable agreement of the computed steady-state shock position to the experimental observations presented in Figure 4 of Sandhu & Jameson. The rightward shift of the computed points may be attributed to the friction losses in the experiment that are not accounted for in the model. To end up with a bubbly shock in a certain fixed position, the experiment would require a larger negative back pressure to overcome the additional frictional losses. Assuming a fully developed turbulent pipe flow, and that the frictional effects do not significantly alter

the flow field * we can estimate the pressure drop associated with viscous losses in the experiment. For the data point at $C_{P_b} \approx -20$ in the upper plot of Figure 8.2 we estimate the viscous losses in the experiment to be $\Delta C_{P_{visc}} \approx 4.0$. Hence if we were to include the friction losses in the model we would have to lower the back pressure an additional 4.0 units to achieve a shock in the same position. This corresponds to moving the data point 4.0 units to the left, which would then give good agreement with the experimental results.

The lower plot of Figure 8.2 shows that the computed throat pressure is about 10% larger than that measured experimentally, and does not closely follow the upward trend on the right of the graph. These differences can again be attributed to the friction losses in the experiment that are not accounted for in the model. In the experiment a relatively small negative back pressure can result in a shockfree flow since there are appreciable friction losses to support the pressure gradient. Hence the experimental data points trend upwards on the right of the graph. The numerical model however only has losses in the bubble dynamics, so the same negative back pressure results in the flow accelerating until it chokes and a bubbly shock forms. Hence the throat pressure remains at the constant choked value.

8.2.1 Effect of impedance boundary condition

In physical experiments there is usually a length of pipe (that may have valves and other apparatus) downstream of the nozzle section before the fluid exits into the atmosphere or reservoir. This has the effect of adding some impedance to the system, so that the back pressure is not accurately controlled immediately downstream of the nozzle section; instead it would tend to fluctuate about some mean value. To investigate the effect that this would have on the computed shock position an impedance BC was implemented at the downstream boundary. This was done, for illustrative purposes, using a simple force balance model at the boundary,

*This assumption is only reasonable for flows with shocks, where the dissipation associated with the shock jump conditions is far greater than viscous losses.

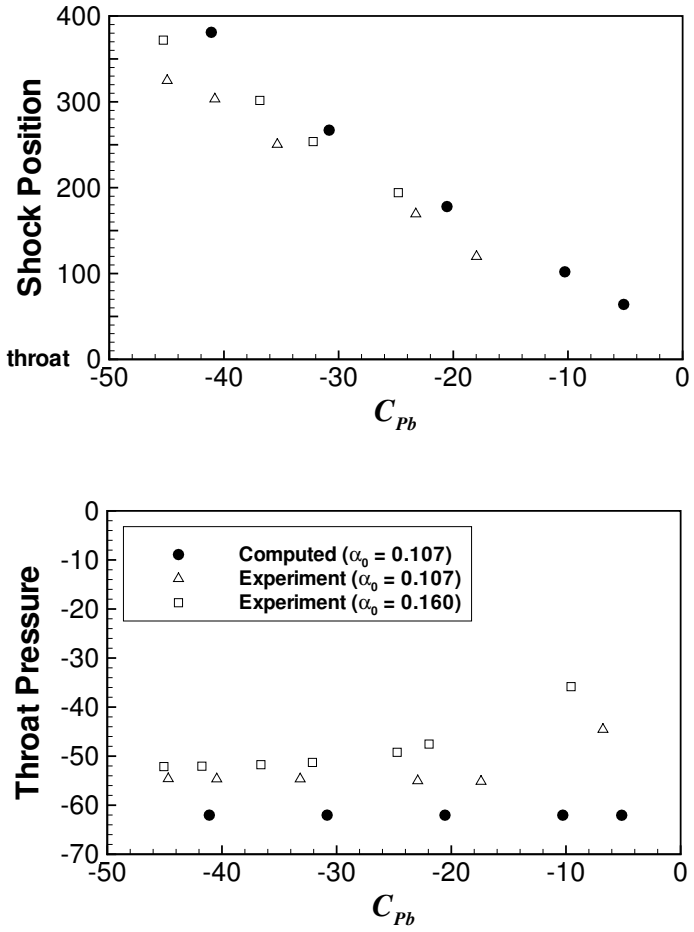

Figure 8.2: Shock position and throat pressure as functions of back pressure for present computation and experimental observations of Sandhu et al. (Parameters are, $\sigma = 81.6$, $We = 4.1$, $\delta_D = 15.2$.)

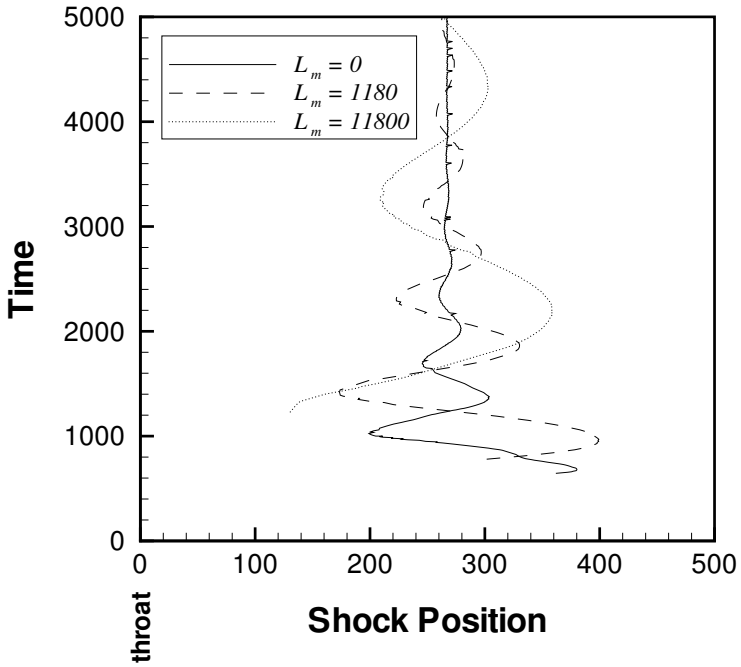

Figure 8.3: Shock position versus time for different impedance lengths ($C_{Pb} = -30.8$)

$$p_N - p(t) = \rho L_m \frac{du_N}{dt}, \tag{8.1}$$

where ρ is the average density of the bubbly mixture at the boundary, L_m is a specified impedance length, [†] $p(t)$ is the specified back pressure, and p_N and u_N are the pressure and velocity at the last grid point in the computational domain.

Figure 8.3 plots the time evolution of the shock position for three different impedance lengths. In each case the shock position exhibits the behavior of a damped oscillator. The final steady-state shock position and the initial amplitude of oscillation are independent of the impedance length. Initially the shock position oscillates back and forth about 200 bubble radii which, based on the average equilibrium bubble radius of the experiment, corresponds to 12 mm. This is of the same order as the 2-5 mm observed in the experiment. As would be expected, the period of the transient oscillations increases with increasing impedance length.

[†]Specifying $L_m = 0$ results in our previously used specified pressure BC.

The dependence of the oscillation frequency on impedance length can be explained by considering acoustic modes in the length of duct between the shock and the downstream boundary. Assuming that the length, L, and the linear (zero frequency) sound speed, c, between the bubbly shock and the downstream boundary are constant, and neglecting the flow velocity as being small compared to the sound speed, then this region is governed by the acoustic wave equations. The boundary conditions can be expressed in terms of the non-dimensional complex impedance, ζ,

$$\hat{p} = \rho c \zeta \hat{u}. \tag{8.2}$$

Equation (8.1) directly yields $\zeta = -i\omega L_m/c$ as the value of impedance at the downstream boundary. It should be noted that equation (8.2) is an approximation for the far more complicated behavior of the bubbly shock; in reality there would be a complex dynamic interaction between the bubbly shock and an acoustic wave. Nevertheless we assume a complex value for the shock impedance, and then solve the resulting acoustic problem for a series of discrete complex frequencies. Figure 8.4 plots the lowest (fundamental) frequency as a function of impedance length for three assumed values of shock impedance. As expected these theoretical curves show that the real part of the frequency decreases as the impedance length is increased. Note that the normalized frequency is $\pi/2$ for the case of infinite shock impedance and zero impedance length. This corresponds to the familiar resonant frequency for an open-closed tube.

Also plotted on Figure 8.4 are some points obtained from computations. The real part of the frequency is obtained by applying a fast Fourier transform (FFT) to the time series of the shock position. [‡] The imaginary part of the frequency is computed from the ratio of amplitudes of successive peaks on Figure 8.3. It is worth noting that the damping ratio is approximately constant for all values of impedance length, so that the attenuation *per cycle* is independent of impedance length. The

[‡]There are not enough cycles to allow use of an FFT for the two highest impedance lengths, so the frequency is computed by measuring the period of oscillation in Figure 8.3.

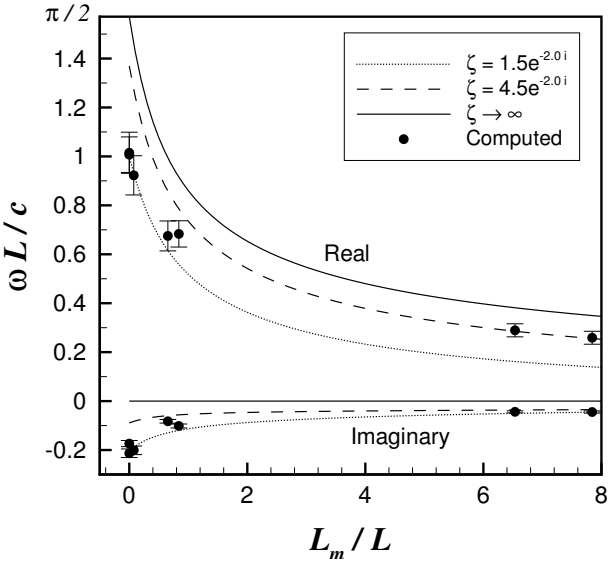

Figure 8.4: Frequency of shock oscillation as a function of impedance length ($C_{Pb} = -30.8$)

error bars essentially indicate the resolution of the FFT. Estimates of the error due to not knowing the domain length and sound speed precisely were also made, but were about an order of magnitude smaller than the resolution of the FFT.

The acoustic theory correctly predicts the trend of decreasing real frequency with increasing impedance length for complex shock impedances with magnitudes ranging from near unity to infinity. In the limit of infinite shock impedance the theory results in an imaginary frequency of zero, in contrast to the computed data points. To obtain reasonable absolute agreement for both real and imaginary frequencies it is necessary to use a shock impedance with magnitude ranging from 1.5 to 4.5 and a complex phase of about -2. If we were to further allow the magnitude of the shock impedance to be a function of frequency, it is conceivable that we could obtain a single theoretical curve to match all the computed data points. In any case, the frequency of the shock oscillation is demonstrated to be governed by acoustic modes between the shock and the downstream boundary, and so in physical experiments the observed frequency would depend upon the experimental apparatus that existed between the shock and the pressure release surface.

Chapter 9

Conclusions

An efficient and accurate numerical method has been developed for computing unsteady, quasi-one-dimensional, bubbly cavitating flows through converging-diverging nozzles. Four different flow regimes are shown to exist depending on the value of the back pressure. For small negative back pressures there exist steady-state solutions with no shocks. As the back pressure is lowered the flow becomes choked, and a steady bubbly shock wave forms in the diverging section of the nozzle. For lower back pressures the bubbly shock wave begins to travel downstream in the diverging section of the nozzle. This unsteady bubbly shock wave is the correct solution in the regime where steady-state computations result in *flashing* solutions. Finally, for even lower back pressures, there exist under-expanded, steady-state solutions with no shocks.

The treatment of diffusive damping of bubble radial motion by the use of an effective damping parameter has shown to have negligible impact on the macroscopic features of the nozzle flow. In addition, the application of the more sophisticated diffusive model of Part I showed only minor differences in the bubbly shock structure, and also demonstrated negligible impact on the onset of the flashing instability in the steady-state computations.

Results of the bubbly cavitating computation are demonstrated to agree with barotropic models for those cases where bubble dynamics are not important, but show that in many instances that the neglect of bubble dynamics in the barotropic models can not be justified. The computations show reasonable agreement with two sets of

experiments; one where spatial variations of flow variables are measured in steady flows, and the other where throat pressure and shock position are measured for flows with bubbly shocks. The frequency of oscillation of the shock position is shown to be dependent on downstream impedance, and can be explained by considering acoustic modes in the region between the shock and downstream boundary.

Appendix A

Parameters for computations

This appendix presents non-dimensional parameters used in all the computations and the results from the individual POD computations. In addition the function fit of the saturation vapor pressure of water to temperature is specified.

A.1 Dimensionless parameters

The properties for air, water and water vapor are all taken from Lide (2001-2002a) and Lide (2001-2002b). All computations use the non-dimensional quantities specified in Section 2.1. Under this non-dimensionalization it is apparent that many of the non-dimensional parameters will only be functions of the ambient temperature and pressure. For all computations the ambient pressure is fixed at one atmosphere, while the ambient temperature takes on three different values. Table A.1 lists the non-dimensional parameters for each of the ambient temperatures. In addition the ratios of specific heats for the air and water vapor are respectively taken to be $\gamma_a = 7/5$ and $\gamma_v = 4/3$, and the molecular weights are $M_a = 28.97$ and $M_v = 18.02$.

Other parameters are non-dimensionalized by the initial bubble radius and its associated isothermal natural frequency and will therefore depend upon these quantities. Table A.2 lists the non-dimensional parameters for all the computations presented. The first number in the run label refers to the dimensional bubble size in μm and the second to the dimensional forcing width in μs. The letter in parentheses indicates the forcing amplitude as listed explicitly in Table A.3. All runs are at an ambient

T_0' (°C)	Pr	Sc	$D \times 10^{-3}$	$\mathfrak{R}_u$	μ_a	k_a	μ_v	k_v
25	6.13	446.3	12.1	1.989	0.0209	0.0432	0.0112	0.0308
60	2.98	237.2	15.3	1.987	0.0431	0.0436	0.0238	0.0329
95	1.85	155.0	20.0	1.974	0.0728	0.0458	0.0409	0.0360

Table A.1: Dimensionless parameters that only vary with ambient temperature. Parameters are; dimensional ambient temperature (T_0'), liquid Prandtl (Pr) and Schmidt (Sc) numbers, mass diffusivity of air-vapor (D), universal gas constant ($\mathfrak{R}_u$), viscosities and thermal conductivities of air (μ_a and k_a), and water vapor (μ_v and k_v).

temperature of 25°C unless there is a number in parentheses which would indicate the temperature. If the run label is preceded with a 'G', then it is a computation for a pure gas bubble, otherwise it is for a gas-vapor bubble.

A.2 POD parameters and results

Table A.3 lists all of the individual computations used to obtain the averaged results presented in Section 2.5.2. The forcing amplitude and parameters pertaining to the selection of the snapshots together with the results of the individual POD computations are provided.

A.3 Saturation vapor pressure

The following equation and parameters are used to model the temperature dependence of the water vapor saturation pressure,

$$p'_{v_{sat}} = p'_c \exp\left[-T'_c/T'\right], \tag{A.1}$$

$$p'_c = 1.17 \times 10^8 kPa, \tag{A.2}$$

$$T'_c = 5200K, \tag{A.3}$$

where the two parameters are determined by fitting to the data points in Lide (2001-2002a). The accuracy of the fit is shown in Figure A.1. In Table A.2 the two fitting

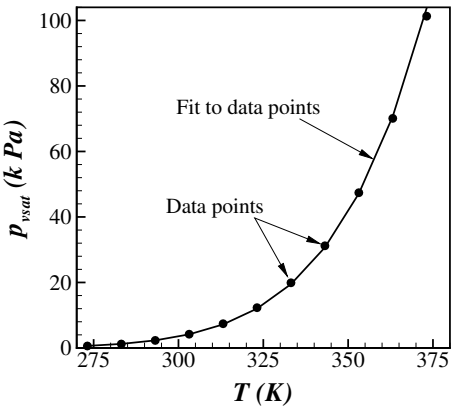

Figure A.1: Curve fit to data for vapor pressure of water as a function of temperature.

parameters are non-dimensionalized in a manner consistent with Section 2.1. That is, $\tilde{p}_c \equiv p'_c/\rho'_l(R'_0\omega'_0)^2$ and $\tilde{T}_c \equiv c'_{pl}T'_c/(R'_0\omega'_0)^2$.

Run(s)	Pe_g	Pe_{a-v}	Re	We	$\tilde{p}_{\infty_0}$	$\tilde{T}_0$ $\times 10^{-3}$	H $\times 10^{6}$	L $\times 10^{-3}$	$\tilde{p}_c$ $\times 10^{-6}$	$\tilde{T}_c$ $\times 10^{-3}$	Σ	t_w	A	$-C_{p_m}-\sigma$
0.6,0.1(a)-(f)[a]	2.87	0.691	18.7	6.46	0.131	1.61	183.1	3.14	0.151	28.0	3.34×10^{-5}	4.65		
0.6,1(a)-(c)[a]	2.87	0.691	18.7	6.46	0.131	1.61	183.1	3.14	0.151	28.0	3.34×10^{-5}	46.5		
4,1(a)-(f)	5.27	3.17	85.9	20.4	0.276	3.39	86.7	6.64	0.319	59.1	1.52×10^{-4}	4.79		
4,10(a)-(e)	5.27	3.17	85.9	20.4	0.276	3.39	86.7	6.64	0.319	59.1	1.52×10^{-4}	47.9		
4,100(a)-(e)	5.27	3.17	85.9	20.4	0.276	3.39	86.7	6.64	0.319	59.1	1.52×10^{-4}	479		
40,1(H)[b]	36.4	28.8	780	168	0.336	4.12	71.4	8.07	0.388	71.8	5.54×10^{-4}	0.435	9.0	2.68
40,10(a)-(f)	36.4	28.8	780	168	0.336	4.12	71.4	8.07	0.388	71.8	5.54×10^{-4}	4.35		
40,100(a)-(f)	36.4	28.8	780	168	0.336	4.12	71.4	8.07	0.388	71.8	5.54×10^{-4}	43.5		
40,1000(a)-(e)	36.4	28.8	780	168	0.336	4.12	71.4	8.07	0.388	71.8	5.54×10^{-4}	435		
400,10(a)-(b)[a]	349	284	7711	1641	0.343	4.21	69.8	8.25	0.396	73.4	1.78×10^{-3}	0.430		
400,100(a)-(b)[a]	349	284	7711	1641	0.343	4.21	69.8	8.25	0.396	73.4	1.78×10^{-3}	4.30		
4000,10(a)-(d)[a]	3475	2841	77030	16370	0.344	4.22	69.7	8.26	0.397	73.6	5.64×10^{-3}	0.043		
4000,100(a)[a]	3475	2841	77030	16370	0.344	4.22	69.7	8.26	0.397	73.6	5.64×10^{-3}	0.430		
40,100(60)[c]	25.2	20.9	1350	152	0.402	5.44	42.2	9.20	0.464	84.9	1.65×10^{-2}	40.0	0.90	0.0371
40,100(95)[d]	6.99	7.37	951	34.9	1.939	28.6	8.65	41.8	2.240	403	7.12×10^{-1}	18.4	0.30	0.290
G4[e]	4.61		87.0	20.9	0.270	3.31								
G10[e]	9.26		204	46.2	0.305	3.74								
G40[e]	34.8		791	172	0.326	3.99								
G50[e]	42.9		987	215	0.327	4.01								

[a] Only used for POD computations.
[b] Only used for figure 3.3(a).
[c] Temperature is 60°C, only used for figure B.2(a).
[d] Temperature is 95°C, only used for figure B.2(a), and in sections 2.3.2 and 3.7.
[e] Pure gas bubbles.

Table A.2: Dimensionless parameters for all computations. All computations are for air-vapor bubbles in water at 25°C and atmospheric pressure unless indicated. Parameters are gas Peclet numbers for heat and mass diffusion, (Pe_g and Pe_{a-v}), liquid Reynolds (Re) and Weber (We) numbers, ambient pressure ($\tilde{p}_{\infty_0}$), ambient temperature ($\tilde{T}_0$), Henry's Law constant (H), latent heat of vaporization (L), pressure and temperature parameter for water vapor pressure fit ($\tilde{p}_c$ and $\tilde{T}_c$ [see section A.3]), thermodynamic parameter for liquid-vapor (Σ), width of forcing Gaussian (t_w), amplitude of forcing Gaussian (A) and maximum applied tension ($-C_{p_m}-\sigma$). Where the amplitude of forcing and maximum tension are not given it indicates that a range of forcings have been used; these are either specified individually in table A.3 or within the text.

Run(s)	A	$-C_{p_m}-\sigma$	$m-1$	t_{start}	t_{end}	β_T	β_C	$1-\lambda_{1_T}$	$1-\lambda_{1_C}$
0.6,0.1(a)	1.3	0.0352	160	0	80	5.035	5.021	4.7×10^{-4}	6.1×10^{-5}
0.6,0.1(b)	1.5	0.0613	160	0	80	5.047	5.026	6.9×10^{-4}	8.1×10^{-5}
0.6,0.1(c)	1.7	0.0875	160	0	80	5.072	5.032	1.2×10^{-3}	1.1×10^{-4}
0.6,0.1(d)	2.0	0.127	160	0	80	5.047	5.039	2.6×10^{-3}	1.8×10^{-4}
0.6,0.1(e)	2.5	0.192	160	0	80	4.996	5.042	9.8×10^{-3}	3.7×10^{-4}
0.6,0.1(f)	3.0	0.258	160	0	80	4.447	5.035	4.0×10^{-3}	6.0×10^{-4}
0.6,1(a)	1.75	0.0940	150	0	300	5.023	5.021	7.1×10^{-5}	2.1×10^{-5}
0.6,1(b)	1.80	0.101	150	0	300	5.116	5.038	2.4×10^{-3}	5.0×10^{-5}
0.6,1(c)	1.85	0.107	150	0	300	5.683	5.074	3.7×10^{-2}	1.7×10^{-4}
4,1(a)	1.05	0.0223	100	0	80	5.568	5.117	7.3×10^{-3}	3.9×10^{-3}
4,1(b)	1.10	0.0361	100	0	80	5.245	5.105	1.3×10^{-2}	4.4×10^{-3}
4,1(c)	1.20	0.0638	100	0	80	5.390	5.075	1.4×10^{-2}	5.5×10^{-3}
4,1(d)	1.30	0.0914	100	0	80	5.578	5.039	1.3×10^{-2}	6.6×10^{-3}
4,1(e)	1.35	0.105	100	0	80	5.797	5.021	8.5×10^{-3}	7.1×10^{-3}
4,1(f)	1.40	0.119	100	0	80	5.153	5.001	6.3×10^{-3}	7.6×10^{-3}
4,10(a)	1.00	0.00849	150	0	300	5.061	5.117	5.4×10^{-4}	6.2×10^{-4}
4,10(b)	1.05	0.0223	150	0	300	4.788	5.211	1.1×10^{-2}	1.8×10^{-3}
4,10(c)	1.065	0.0265	150	0	300	5.441	5.237	3.3×10^{-3}	2.6×10^{-3}
4,10(d)	1.08	0.0306	150	0	300	4.923	5.238	2.1×10^{-3}	3.8×10^{-3}
4,10(e)	1.10	0.0361	150	0	300	5.289	5.194	6.9×10^{-3}	6.0×10^{-3}
4,100(a)	1.03	0.0168	200	0	2000	5.005	5.015	6.4×10^{-6}	6.5×10^{-5}
4,100(b)	1.04	0.0196	200	0	2000	4.987	5.088	4.7×10^{-5}	2.0×10^{-4}
4,100(c)	1.045	0.0209	200	0	2000	5.010	5.220	1.3×10^{-4}	7.6×10^{-4}
4,100(d)	1.047	0.0215	200	0	2000	5.519	5.379	8.9×10^{-4}	1.8×10^{-3}
4,100(e)	1.048	0.0218	200	0	2000	4.988	5.364	5.5×10^{-4}	2.9×10^{-3}
40,10(a)	1.10	0.0439	100	0	100	5.055	5.617	3.2×10^{-2}	2.3×10^{-2}
40,10(b)	1.20	0.0775	100	0	100	6.565	5.636	3.4×10^{-2}	2.4×10^{-2}
40,10(c)	1.25	0.0943	100	0	100	7.118	5.605	3.5×10^{-2}	2.4×10^{-2}
40,10(d)	1.30	0.111	100	0	100	6.031	5.536	2.8×10^{-2}	2.5×10^{-2}
40,10(e)	1.40	0.145	100	0	100	6.191	5.240	2.6×10^{-2}	2.7×10^{-2}
40,10(f)	1.50	0.178	100	0	100	6.241	4.721	2.2×10^{-2}	3.1×10^{-2}
40,100(a)	0.95	-0.00645	150	0	300	5.981	4.641	1.9×10^{-2}	2.2×10^{-2}
40,100(b)	0.96	-0.00310	150	0	300	5.556	4.505	2.4×10^{-2}	2.2×10^{-2}
40,100(c)	0.97	0.00261	150	0	300	7.139	4.335	3.2×10^{-2}	2.4×10^{-2}
40,100(d)	0.985	0.00530	150	0	300	7.387	4.002	2.6×10^{-2}	2.8×10^{-2}
40,100(e)	0.99	0.00698	150	0	300	6.090	3.880	3.0×10^{-2}	3.0×10^{-2}
40,100(f)	1.00	0.0103	150	0	300	7.530	3.585	2.7×10^{-2}	3.4×10^{-2}
40,1000(a)	0.95	-0.00645	200	0	2000	5.015	5.053	1.5×10^{-4}	5.9×10^{-3}
40,1000(b)	0.96	-0.00310	200	0	2000	5.052	5.179	6.0×10^{-4}	1.2×10^{-2}
40,1000(c)	0.97	0.00261	200	0	2000	5.378	5.098	1.6×10^{-3}	2.5×10^{-2}
40,1000(d)	0.98	0.00362	200	0	2000	5.396	4.435	1.0×10^{-2}	4.7×10^{-2}
40,1000(e)	0.985	0.00530	200	0	2000	5.488	3.780	6.9×10^{-3}	7.0×10^{-2}
400,10(a)	0.10	-0.298	100	0	40	14.74	14.77	2.2×10^{-2}	2.1×10^{-2}
400,10(b)	3.00	0.697	100	0	40	12.09	15.58	3.5×10^{-2}	1.0×10^{-2}
400,100(a)	1.00	0.0105	100	0	100	10.66	13.27	5.5×10^{-2}	8.5×10^{-2}
400,100(b)	1.10	0.0448	100	0	100	9.735	13.34	5.5×10^{-2}	8.3×10^{-2}
4000,10(a)	0.10	-0.299	100	0	40	44.58	44.68	1.1×10^{-2}	1.1×10^{-2}
4000,10(b)	3.0	0.698	100	0	40	44.27	44.44	1.1×10^{-2}	1.0×10^{-2}
4000,10(c)	10.0	3.10	100	0	40	42.83	44.46	1.1×10^{-2}	8.1×10^{-3}
4000,10(d)	13.0	4.14	100	0	40	42.49	45.52	1.2×10^{-2}	7.2×10^{-3}
4000,100(a)	1.0	0.0105	100	0	40	43.14	44.46	1.1×10^{-2}	8.3×10^{-3}

Table A.3: Parameters and results for POD computations. Parameters are amplitude of Gaussian forcing (A), maximum applied tension ($-C_{p_m}-\sigma$), number of snapshots minus one ($m-1$), times where the sequence of snapshots are started (t_{start}) and ended (t_{end}). Results obtained from POD computations are; heat (β_T) and mass (β_C) transfer coefficients of first POD mode, and fractions of energy *not* captured by first POD modes ($1-\lambda_{1_T}$, $1-\lambda_{1_C}$).

Appendix B

Simplifications to full equations

The approximations presented in Section 2.4 enable simplifications to be made to the original equations. Here the accuracy of these approximations are examined in detail using scaling arguments and numerical experiments. In the following sections each of the approximations are examined independently by plotting relative error versus the appropriate parameter that has been determined from scaling analysis. The relative error, ϵ_X, are defined by

$$\epsilon_X \equiv \frac{X^{approx} - X^{complete}}{X^{complete}}, \tag{B.1}$$

where X is a particular variable on interest. The superscripts represent the approximate solution obtained from the simplified equations, and the solution obtained with the more complete equations. In each section the new simplification is introduced to the set of equations that employ the simplifications made in the previous sections. Thus, for example, all computations presented in Sections B.2 through B.4 use the insoluble gas approximation presented in Section B.1.

We seek simplifications that give a maximum bubble radius, R_{max}, and the rebound bubble radius, $R_{rebound}$, to within a few percent of the values obtained from the more complete computation. The less important minimum bubble radius, R_{min}, should be within about 10%. These criteria are specifically for applications where only the bubble dynamics are required to be accurate, and we often find that the simplifi-

cations result in maximum bubble pressures, p_{max}, average temperatures, $\bar{T}_{max}$, and minimum concentrations, $\bar{C}_{min}$, that are correct to only within an order of magnitude. If we were interested in applications where these quantities were of concern (for example sonoluminescence) then some of the following simplifications should not be applied.

B.1 Insoluble gas

We now proceed with a scaling analysis to determine under what circumstances diffusion of gas in the liquid can be neglected. If we assume the process of gas entering the bubble is limited by liquid side diffusion, then the amount of gas that is available to enter the bubble would scale with the boundary layer thickness determined by the mass diffusivity in the liquid and the timescale of the forcing, which in non-dimensional terms is given by $\sqrt{t_w/(ScRe)}$. For sufficiently small values of $t_w/(ScRe)$ the amount of gas readily available to the bubble would be limited, and we would be able to neglect the diffusion of gas in the liquid.

In order to validate the scaling analysis, Figure B.1 compares the simplified insoluble gas computation to the full computation by plotting ϵ_X versus $t_w/(ScRe)$. We see that the relative errors in R_{max}, $R_{rebound}$ and, to a lesser extent, R_{min} scale with this parameter, as would be expected from the scaling analysis. The trends for p_{max}, T_{max} and $\bar{C}_{min}$ are similar although there is considerably more scatter in the data. Importantly, we can see that for the present air-water system errors in the bubble dynamics due to assuming an insoluble gas will be less than a few percent as long as the following condition is met,

$$t_w/(ScRe) \lesssim 10^{-3}. \tag{B.2}$$

It should be reiterated that this condition (B.2) is determined for the current air-water system at 25°C and atmospheric pressure. It would be necessary to re-evaluate the

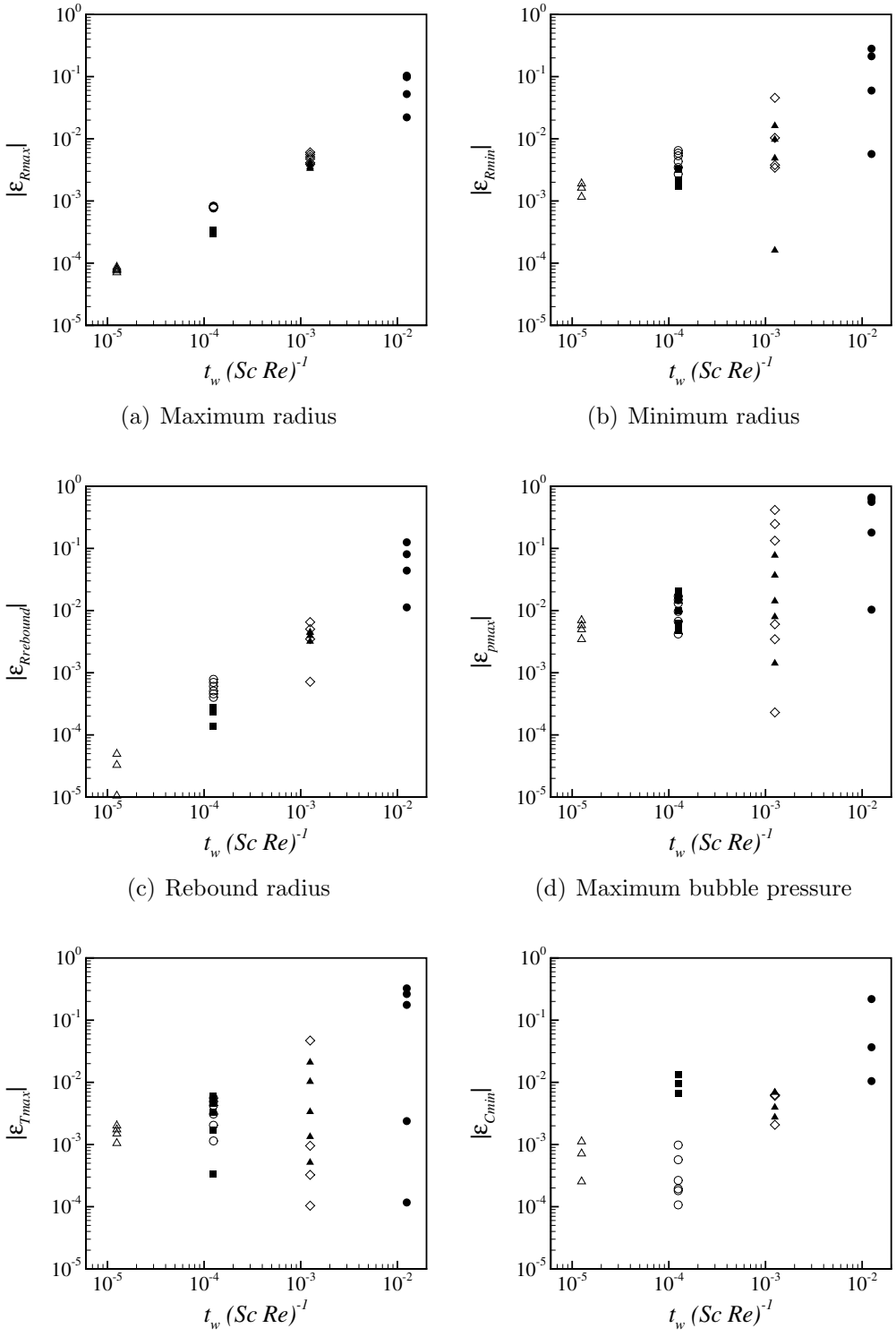

(a) Maximum radius (b) Minimum radius

(c) Rebound radius (d) Maximum bubble pressure

(e) Maximum average bubble temperature (f) Minimum average vapor concentration

Figure B.1: Relative errors due to neglecting mass diffusion of air in liquid. ■ 4,1(a)-(f); ▲ 4,10(a)-(e); ● 4,10(a)-(e); △ 40,10(a)-(f); ○ 40,100(a)-(f); ◇ 40,1000(a)-(e).

condition for other situations, where the solubility of the gas may be different. For example, if the system was at a lower temperature, or comprised of carbon-dioxide and water we would expect a much higher concentration of dissolved gas in the liquid, and the limit (B.2) would have to be decreased. It is also useful to note that if (B.2) is satisfied then there is minimal impact on $\bar{T}_{max}$ and $\bar{C}_{min}$, while the error in p_{max} would be reduced to acceptable levels if the criteria (B.2) was decreased by an order of magnitude. This suggests the insoluble gas approximation could also be used in circumstances where these quantities are relevant.

B.2 Cold liquid

For bubbles with $PrRe \gg 1$ Brennen (1995) examined the thermal effects for bubble growth due to a step decrease in pressure and identified the timescale of bubble growth, the applied tension, and the following thermodynamic parameter of the liquid,

$$\Sigma'(T') \equiv \frac{L'^2 \rho_v'^2}{\rho_l'^2 c_{pl}' T' \alpha_l'^{1/2}}, \tag{B.3}$$

as being important in whether thermal effects will have an impact on bubble growth. In equation (B.3) $\alpha_l' = k_l'/\rho_l' c_{pl}'$ is the thermal diffusivity of the liquid. Note that Σ' has units of $m/s^{3/2}$. Assuming the analysis to approximately hold for bubble growth caused by a Gaussian decrease in pressure (rather than a step change) we define a non-dimensional parameter based directly on the analysis of Brennen (1995),

$$\Theta \equiv \frac{t_w \Sigma^2}{-C_{p_m} - \sigma}, \tag{B.4}$$

$$= \frac{t_w' \Sigma'^2 \rho_l'}{p_v' - p_{\infty_{min}}'}, \tag{B.5}$$

where $\Sigma \equiv \Sigma'/R_0' \omega_0'^{3/2}$ is the non-dimensional thermodynamic parameter, $C_{p_m} = -\tilde{p}_{\infty_0} A$ is the minimum pressure coefficient, and $t_w' = t_w/\omega_0'$ is the dimensional

timescale for the Gaussian pressure forcing. Note that the analysis is for positive tensions, $-C_{p_m} - \sigma > 0$, so that Θ is always positive. The analysis indicates that thermal effects in the liquid can be neglected for the low values of Θ. For most liquids Σ'^2, and consequently Θ (for reasonable timescales and tensions), increases by many orders of magnitude as the liquid temperature is increased from the triple point to the critical point. So for low temperatures, Θ is generally small enough and we can neglect the temperature variation in the liquid. Hence we refer to this approximation as the *cold liquid* approximation.

The analysis is validated in Figure B.2 which plots error in different variables due to neglecting heat transfer in the liquid versus the non-dimensional parameter Θ. All data points are for air-water bubbles at 25°C unless otherwise indicated. We see that the error in R_{max} increases with Θ as would be expected from the analysis. There is scatter in the data, as may be expected since the analysis was for a (large) step change in pressure, while we apply it here to a Gaussian pressure variation. The trends of the other variables are not as apparent, perhaps largely because there are no data points for the higher temperature cases. This is because at these higher temperatures, the bubble does not undergo a violent collapse, so there is not a well defined minimum and rebound radius (Section 2.3.2).

Importantly it is noted that for all the computations at 25°C the error in the R_{max} and $R_{rebound}$ is less than a few percent and for R_{min} less than about 10%, so for modeling bubble dynamics the cold liquid assumption is valid for water at this temperature. The assumption also has little impact on $\bar{T}_{max}$ with errors less than 10%, while the errors in p_{max} and $\bar{C}_{min}$ are as high as about 50%, so that neglecting the effect of liquid temperature would only be able to yield order of magnitude results for these quantities. We conclude that for water at 25°C the bubble dynamics will not be significantly affected by making the cold liquid assumption.

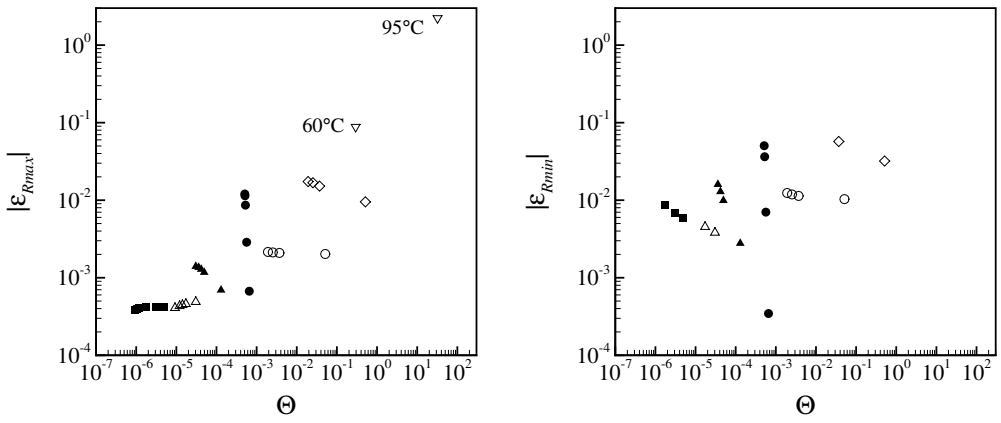

(a) Maximum radius (b) Minimum radius

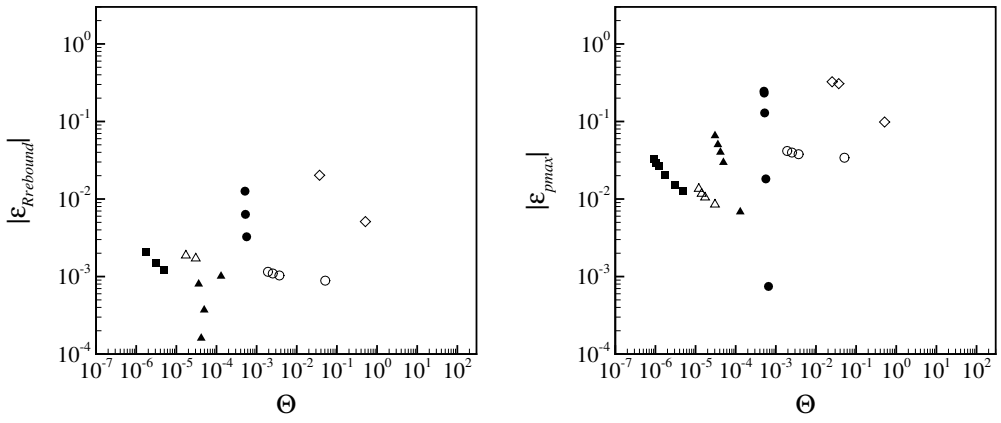

(c) Rebound radius (d) Maximum bubble pressure

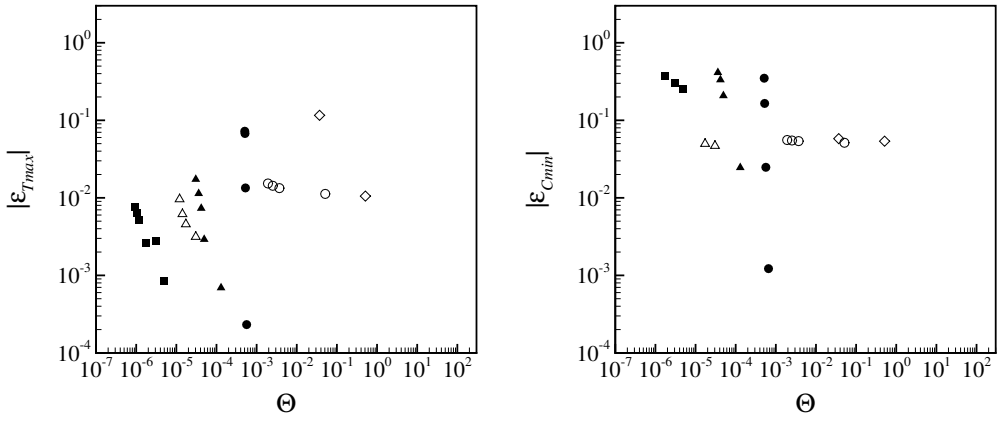

(e) Maximum average bubble temperature (f) Minimum average vapor concentration

Figure B.2: Relative errors due to neglecting temperature changes in liquid. ■ 4,1(a)-(f); ▲ 4,10(a)-(e); ● 4,10(a)-(e); △ 40,10(a)-(f); ○ 40,100(a)-(f); ◇ 40,1000(a)-(e); ▽ 40,100(60) and 40,100(95).

B.3 Equilibrium phase change

In the absence of non-condensible gas, Plesset & Prosperetti (1977) demonstrate that for α of order unity then the non-equilibrium correction is of order of the Mach number of the bubble wall. Here we examine the validity of assuming equilibrium phase change by varying the value of accommodation coefficient, α, and also modifying the code to allow for the vapor pressure at the bubble wall to be in equilibrium, for which we denote the results as $\alpha \to \infty$. Figure B.3 plots the error due to changing α from its assumed true value of 0.4, versus the maximum Mach number. We would expect to see the errors for the variables associated with the collapse increase with Mach number. While there is such a trend for the error in R_{min}, it is only slight. Indeed the errors remain low even as the Mach number approaches unity. This is presumably due to the presence of a non-condensible gas in the full computations. This decreases the impact of varying α since the phase change is limited by finite rate mass diffusion, rather than non-equilibrium effects.

Regardless of the trends of the errors with Mach number, Figure B.3 shows that assuming equilibrium phase change ($\alpha \to \infty$) has only small impact on R_{max}, R_{min} and $R_{rebound}$ compared to using $\alpha = 0.4$. However the effect on p_{max} and $\bar{C}_{min}$ is fairly significant, probably due to the role that finite rate phase change plays in trapping vapor during the fast bubble collapse (Storey & Szeri 2000). It is important to note that if the true value of α is significantly lower than 0.4 then assuming equilibrium phase change would result in significant error in bubble dynamics, as demonstrated by the large errors of the $\alpha = 0.04$ computations.

To summarize it has been demonstrated that the bubble dynamics are not significantly impacted by the assumption of equilibrium phase change, as long as the true value of accommodation coefficient is of order 0.1 or greater.

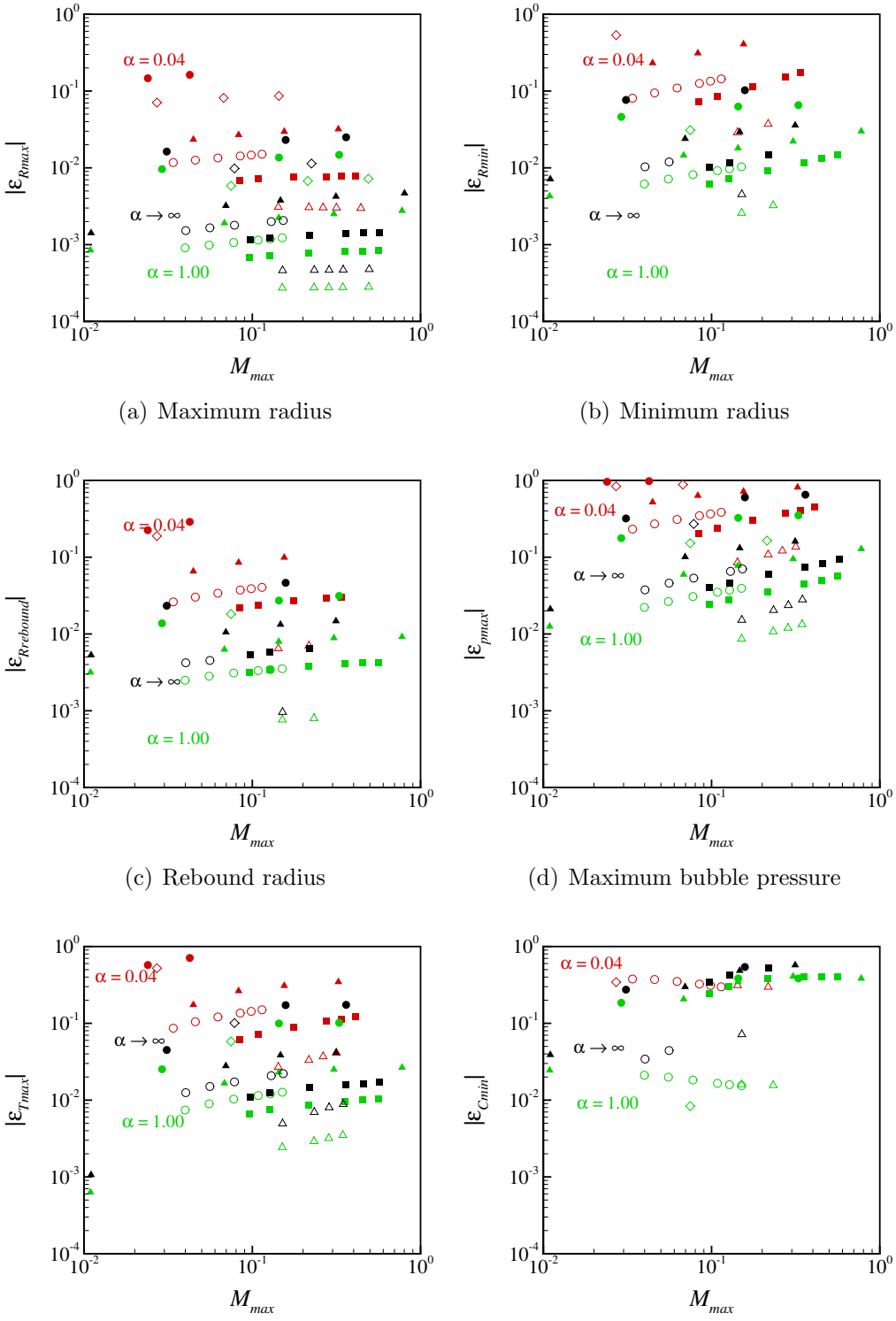

(a) Maximum radius (b) Minimum radius

(c) Rebound radius (d) Maximum bubble pressure

(e) Maximum average bubble temperature (f) Minimum average vapor concentration

Figure B.3: Relative errors due to varying value of accommodation coefficient (α). ■ 4,1(a)-(f); ▲ 4,10(a)-(e); ● 4,10(a)-(e); △ 40,10(a)-(f); ○ 40,100(a)-(f); ◇ 40,1000(a)-(e).

B.4 Homobaricity

The validity of the homobarotropic approximation has been analyzed by Nigmatulin et al. (1981) and Prosperetti et al. (1988) who demonstrate, for the cases where the bubble radius is far smaller than the acoustic wavelength of the gas, that the relative difference in pressure at the bubble center to pressure at the bubble wall scales with the square of the Mach number of the bubble wall. Therefore the approximation is likely to be valid for most bubble motions, except perhaps during the violent collapse when the Mach number may become high.

Figure B.4 plots the relative error due to assuming homobaricity versus the maximum Mach number of the bubble wall based upon the sound speed of the gas. During a bubble motion the maximum in Mach number occurs during the first collapse stage, just prior to the point of minimum radius, so we would not expect large errors prior to this point. Indeed the error in R_{max} are all well under 1%, as are the error in $R_{rebound}$. The error in the quantities associated with the collapse (that is R_{min}, p_{max}, $\bar{T}_{max}$ and $\bar{C}_{min}$) only show very slight increasing trends with maximum Mach number. For R_{min} and p_{max} the errors are less than 10%, which is perhaps surprisingly small given maximum Mach numbers are approaching unity. These results are consistent with Lin et al. (2002) who demonstrate through numerical comparisons that the bubble dynamics are not significantly impacted by the homobarotropic assumption even for Mach numbers exceeding unity. Analysis in the same paper suggests that it is not the bubble wall Mach number that is important for determining whether the homobarotropic assumption can be made, but the bubble wall acceleration. They also suggest a simple way to correct homobarotropic computations for the pressure non-uniformities that exist in the more precise computations.

Based upon the smallness of the errors in the bubble dynamics shown here, and the results of Lin et al. (2002), it is clear that the homobarotropic assumption is valid in the present applications.

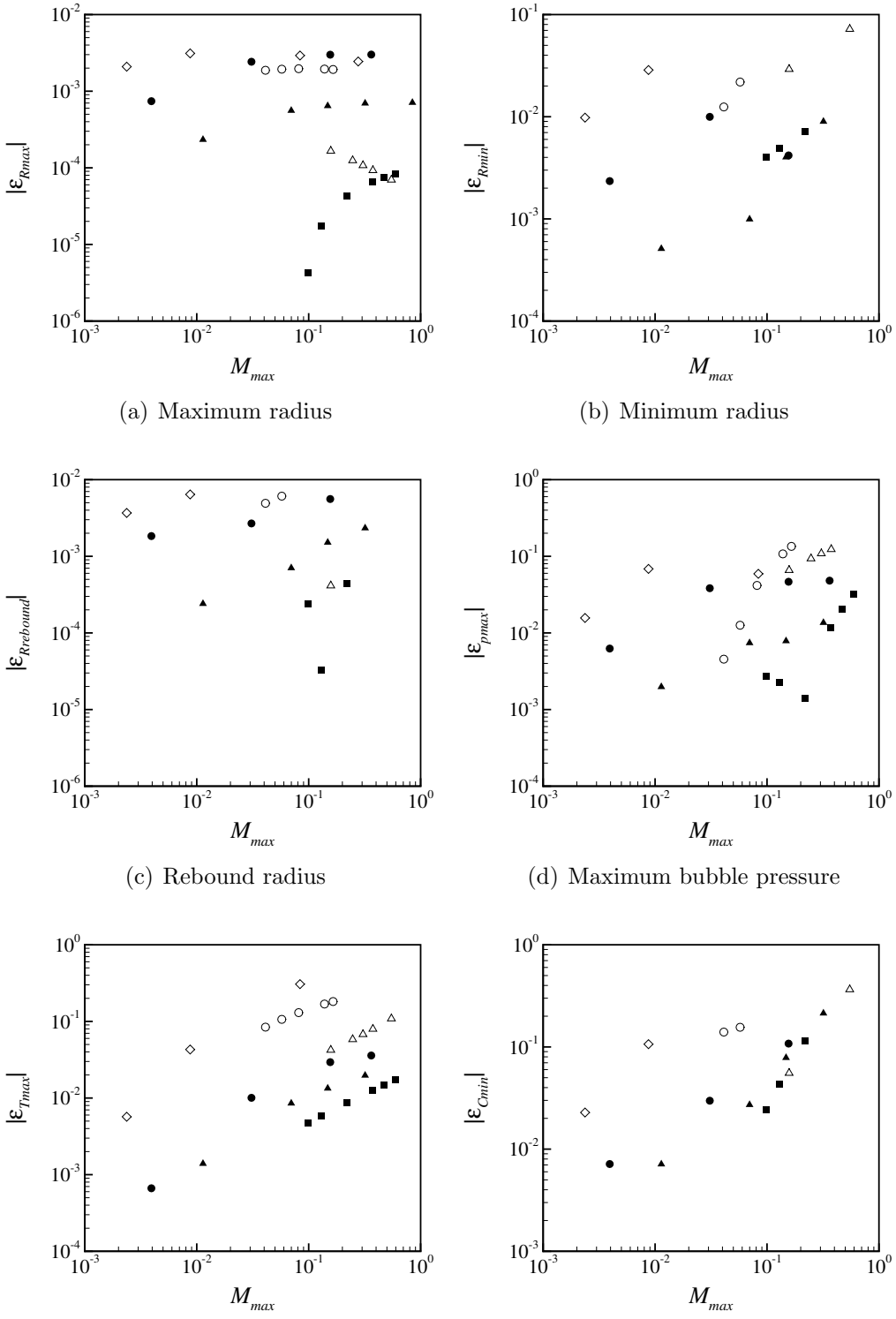

(a) Maximum radius (b) Minimum radius

(c) Rebound radius (d) Maximum bubble pressure

(e) Maximum average bubble temperature (f) Minimum average vapor concentration

Figure B.4: Relative errors due to homobarotropic assumption. ■ 4,1(a)-(f); ▲ 4,10(a)-(e); ● 4,10(a)-(e); △ 40,10(a)-(f); ○ 40,100(a)-(f); ◇ 40,1000(a)-(e).

Appendix C

Approximation of transfer function in frequency domain

In Section 3.2 the transfer function, $\Psi(\omega; Pe)$, was crudely approximated by the zeroth term in the Taylor Series about a specific frequency. The selection of a single frequency, and the subsequent neglect of the imaginary part, precluded the constant transfer model from capturing certain aspects of the diffusive behavior. We now present a model based upon a rational function approximation for the transfer function. We presently focus on modeling the thermal behavior of a pure gas bubble, which enables the thermal model to be developed independently of the mass diffusion model. However, the method is readily extended to enable modeling of the mass diffusion.

C.1 Approximation and model equations

We wish to approximate the transfer function, given by equation (3.21), by another function that will yield a tractable and useful set of equations when equation (3.20) or (3.19) are transformed back into the time domain. We begin by rewriting equation (3.21) for $z \equiv i\omega Pe$,

$$\Psi(z) \equiv \left\{ \left[\sqrt{z} \coth \sqrt{z} - 1 \right]^{-1} - \frac{3}{z} \right\}^{-1}. \tag{C.1}$$

This is approximated by the following rational function,

$$\Psi^{m,n}_{approx}(z) = \frac{\sum_{i=0}^{m} a_i}{1 + \sum_{i=1}^{n} b_i}, \tag{C.2}$$

where the a_i and b_i are determined by matching terms in the series expansions about $z = 0$ of $\Psi(z)$ and $\Psi^{m,n}_{approx}(z)$.

Table C.1 give the coefficients for $m = n = 1$ and $m = n = 2$. Figure C.1 plots $\Psi(z)$ and $\Psi^{m,n}_{approx}(z)$ for the same values of m and n. The agreement of the higher-order ($m = n = 2$) approximation is excellent for a range of z, even to the extent of matching the location of the first pole on the negative axis. The lower-order ($m = n = 1$) approximation shows good agreement for a more restricted range of z, with notable departure at the location of the pole and at higher positive values of z.

Coefficient	$m = n = 1$	$m = n = 2$
a_0	5	5
a_1	2/9	4/13
a_2	-	3/1001
b_1	1/63	3/91
b_2	-	1/9009

Table C.1: Coefficients for rational function approximation of transfer function, $\Psi^{m,n}_{approx}(z)$, as defined by equation (C.2).

The coefficients in Table C.1 are real, so that equation (3.22) is satisfied for the approximations, which will result in real valued quantities when equation (3.20) or (3.19) are transformed back into the time domain. Equation (3.20) is transformed into time and the linearized temperature is rewritten in terms of the original temperature to yield

$$T_y + b_1 Pe_g \dot{T}_y + b_2 Pe_g^2 \ddot{T}_y + \ldots = a_0[\bar{T} - T_w] + a_1 Pe_g \dot{\bar{T}} + a_2 Pe_g^2 \ddot{\bar{T}} + \ldots, \tag{C.3}$$

where $T_y \equiv \partial T/\partial y|_{y=1}$ and an over-dot denotes a derivative with respect to time.

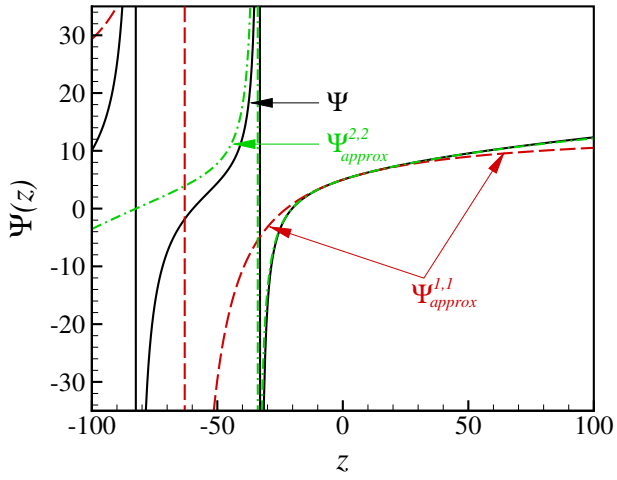

Figure C.1: Rational function approximations, $\Psi^{m,n}_{approx}(z)$, of the transfer function, $\Psi(z)$, for $m = n = 1$ and $m = n = 2$.

Recall that $\bar{T}$ is well approximated by equation (3.11), which for a pure gas bubble with no mass transfer becomes

$$\frac{\bar{T}}{T_0} \approx \frac{p}{p_0}\frac{R^3}{R_0^3}. \tag{C.4}$$

This can be directly differentiated to yield expressions for the time derivatives of $\bar{T}$, so that the right hand side of equation (C.3) is known. We therefore have an n^{th}-order ODE for the temperature gradient at the bubble wall, T_y. This is rewritten as n first-order ODEs and appended to the model equations.

C.2 Model results

The rational function approximation model was implemented for both $m = n = 1$ and $m = n = 2$. Although the higher-order approximation is a more accurate representation of the transfer function in frequency space (Figure C.1), the resulting model equations were found to give less accurate results than the model based upon the lower-order approximation. The higher-order model equations were also unstable

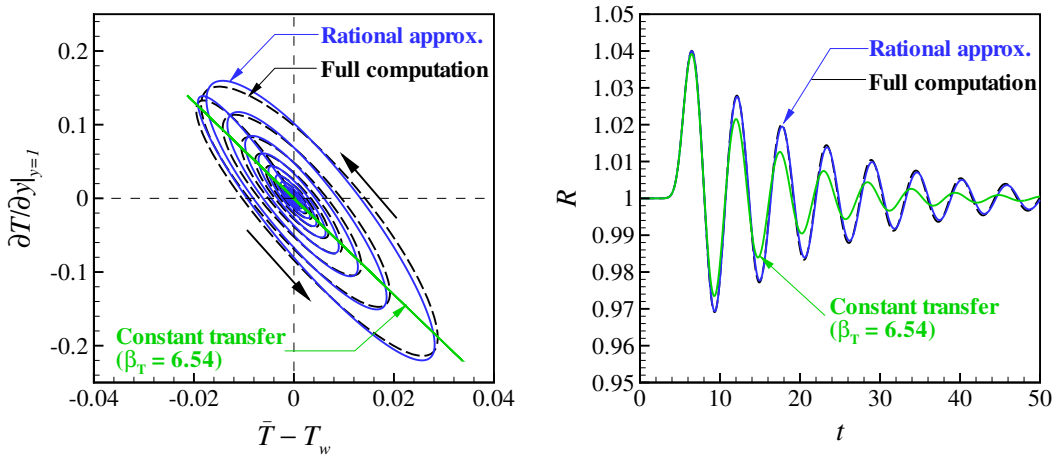

(a) Heat transfer (b) Radius

Figure C.2: Low amplitude (linear) results of model based upon rational function approximation of transfer function for a gas bubble ($Pe_g = 34.8$). [Run G40, $t_w = 1.0$, $A = 0.1$.]

in certain circumstances. Results are therefore only presented for the lower-order ($m = n = 1$) implementation.

Since the model is based upon an approximation of the transfer function resulting from the linear analysis of Section 3.2, it is first useful to gauge the model for a low amplitude (linear) bubble motion. Figure C.2 plots comparisons, for a low amplitude motion, of a full computation to the model based upon the rational function approximation and the constant transfer model of Chapter 3. In (a) it is apparent that the rational approximation model captures the phase lag between the temperature gradient and average temperature, with the cycle loops accurately matching those of the full computation. By contrast, the constant transfer model does not exhibit the phase lag behavior. The agreement in terms of the bubble dynamics in (b) is also excellent for the rational approximation model, with the curve being indistinguishable from that of the full computation. The constant transfer model on the other hand over damps the bubble motion.

The rational approximation model is now tested for a non-linear bubble motion with the comparisons being plotted in Figure C.3. In (a) it is apparent that the rational approximation model does not accurately match the loops of the full com-

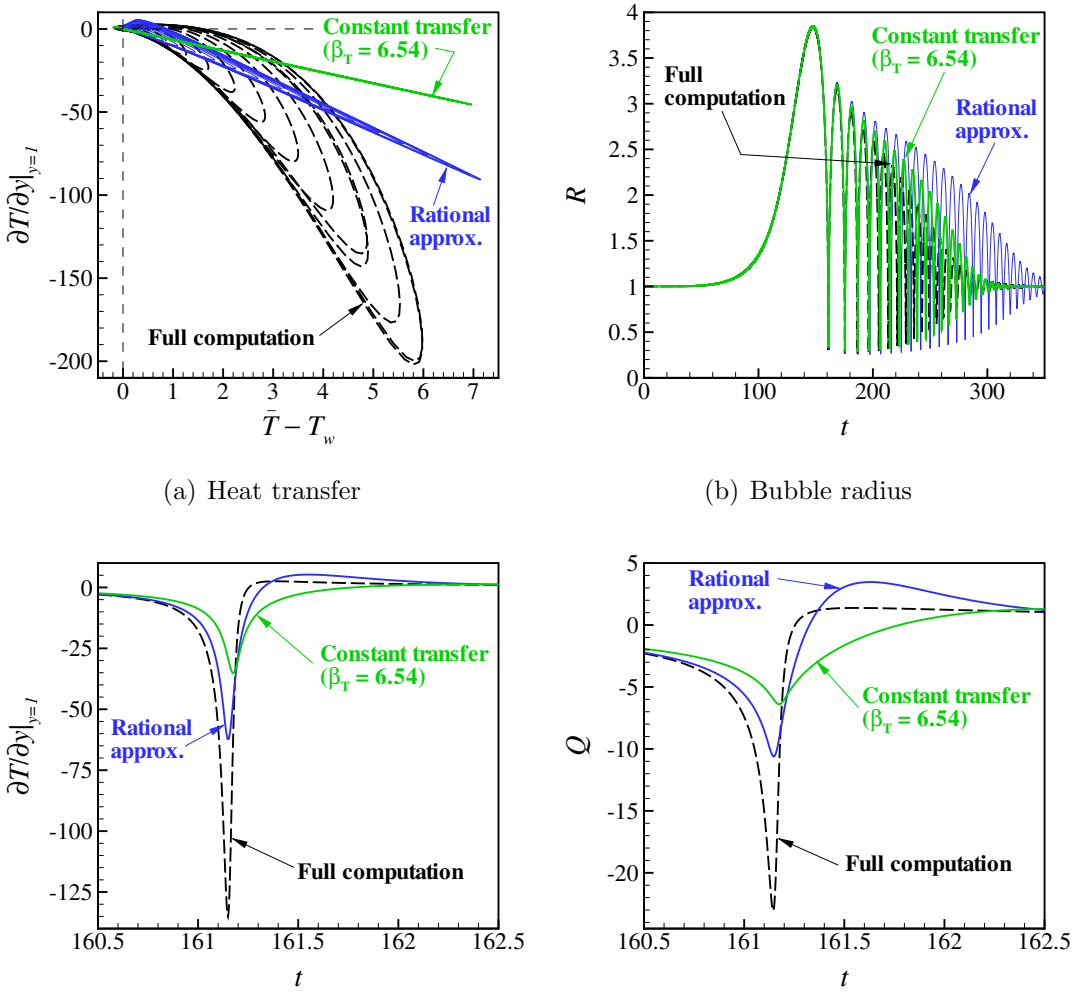

(a) Heat transfer

(b) Bubble radius

(c) Temperature gradient

(d) Heat flow

Figure C.3: Non-linear results of model based upon rational function approximation of transfer function for a gas bubble ($Pe_g = 34.8$). [Run G40, $t_w = 43.5$, $A = 1.0$.]

putation. It does however exhibit some slight phase lag behavior, in contrast to the constant transfer model. The bubble radius shown in (b) indicates that the rational approximation model under damps the bubble rebounds, and is in fact less accurate than the constant transfer model. This is in spite of the fact that the estimates of the temperature gradient by the rational approximation model follow the full computation more closely than that of the constant transfer model. This is shown in (c), where the temperature gradient through the first bubble collapse is plotted (similar behavior occurs in subsequent bubble collapses).

The reason for the under damping of bubble rebounds of the rational approximation model can be deduced by plotting the total heat flow into the bubble, Q, which is defined by

$$\begin{aligned} Q &\equiv -A.q & \text{(C.5)} \\ &= 4\pi R^2 k_a \frac{\partial T}{\partial r}\Big|_{r=R} & \text{(C.6)} \\ &= 4\pi R k_a \frac{\partial T}{\partial y}\Big|_{y=1}. & \text{(C.7)} \end{aligned}$$

This quantity is plotted for the models and full computation in Figure C.3(d) for the first bubble collapse and rebound. For the constant transfer model, the relatively poor estimate of Q during the collapse is balanced by a similarly poor estimate during rebound. That is, the two areas defined by the differences of the constant transfer and full computation curves are of similar size and of opposite sign, so that $\int Q dt$ over the collapse and rebound is approximately the same for the constant transfer model and the full computation. By contrast, the differences between the rational approximation and full computation curves define three areas. While each of these three areas are smaller than the two that are defined for the constant transfer model, the largest two are of the same sign. Therefore the net of the three areas does not cancel to near zero and $\int Q dt$ for the rational approximation model is not similar to that of the full computation.

The main fault of the rational approximation model is that it overestimates the positive temperature gradient that occurs in the latter stages of the rebound. While this does not appear to be too detrimental in Figure C.3(c), the overestimation occurs when the bubble radius is relatively large. This results in a significant overestimation of the total heat flow, Q, into the bubble as shown in (d). The accurate modeling of the temperature gradient during collapse, when the bubble radius is small, is not as important as the modeling during the expansion phases when the bubble radius is large. This explains why the constant transfer model achieves bubble dynamics that agree well with full computations. The rational approximation model may still be

useful in studies of linear (and slightly non-linear) bubble dynamics, since the phase lag behavior is easily captured by only two ODEs.

Appendix D

Parameters for diffusive nozzle computation

This appendix presents non-dimensional parameters used to compute Figure 7.6. Table D.1 gives the parameters that are non-dimensionalized as in Part I of the thesis. These parameters are used for the computation, and are then converted to the non-dimensionalization of Part II (Table D.2) by re-normalizing with the inlet velocity u_0.

Sub figure	u_0	σ	We	Re
(a)	0.76500	0.6507	167.7	779.5
(b)	0.77698	0.6507	167.7	779.5
(c)	0.77984	0.6507	167.7	779.5
(d)	0.78191	0.6507	167.7	779.5

Table D.1: Parameters used in the computation of Figure 7.6 using the non-dimensionalization of Part I.

Sub figure	u_0	σ	We	δ_D ($\nu = 1$)	δ_D ($\nu = 15$)
(a)	1	1.112	98.1	0.00671	0.101
(b)	1	1.078	101.2	0.00660	0.0991
(c)	1	1.070	102.0	0.00658	0.0987
(d)	1	1.064	102.5	0.00656	0.0984

Table D.2: Parameters used in the computation of Figure 7.6 using the non-dimensionalization of Part II.

Bibliography

Biesheuvel, A. & van Wijngaarden, L. (1984), Two phase flow equations for a dilute dispersion of gas bubbles in liquid, *J. Fluid Mech.* **148**, 301–318.

Bird, R., Stewart, W. & Lightfoot, E. (1960), *Transport Phenomena*, John Wiley & Sons.

Brennen, C. E. (1995), *Cavitation and Bubble Dynamics*, Oxford University Press.

Canuto, C., Hussaini, M., Quarteroni, A. & Zang, T. (1988), *Spectral Methods in Fluid Dynamics*, Springer-Verlag.

Chen, Y. & Heister, S. D. (1996), Modeling hydrodynamic nonequilbrium in cavitating flows, *Journal of Fluids Engineering-Transactions of the ASME* **118**, 172–178.

Colonius, T., Brennen, C. E. & d'Auria, F. (1998), Computation of shock waves in cavitating flows, *ASME/FED Third International Symposium on Numerical Methods for Multiphase Flow* .

Colonius, T., d'Auria, F. & Brennen, C. E. (2000), Acoustic saturation in bubbly cavitating flow adjacent to an oscillating wall, *Phys. Fluids* **12**(11), 2752–2761.

d'Agostino, L. & Brennen, C. E. (1988), Acoustical absorption and scattering cross sections of spherical bubble clouds, *J. Acoust. Soc. Am.* **84**(6), 2126–2134.

d'Agostino, L. & Brennen, C. E. (1989), Linearized dynamics of spherical bubble clouds, *J. Fluid Mech.* **199**, 155–176.

d'Agostino, L., Brennen, C. E. & Acosta, A. J. (1988), Linearized dynamics of two-dimensional bubbly and cavitating flows over slender surfaces, *J. Fluid Mech.* **192**, 485–509.

d'Agostino, L., d'Auria, F. & Brennen, C. E. (1997), On the inviscid stability of parallel bubbly flows, *J. Fluid Mech.* **339**, 261–274.

Delale, C. F. (2002), Thermal damping in cavitating nozzle flows, *J. Fluids Eng.* **124**, 969–976.

Delale, C. F., Schnerr, G. H. & Sauer, J. (2001), Quasi-one-dimensional steady-state cavitating nozzle flows, *J. Fluid Mech.* **247**, 167–204.

Ferziger, Joel, H. & Peric, M. (1999), *Computational Methods for Fluid Dynamics*, 2 edn, Springer, chapter 6, pp. 134–140.

Flynn, H. G. (1975), Cavitation dynamics. I. A mathematical formulation, *J. Acoust. Soc. Am.* **57**(6), 1379–1396.

Fujikawa, S. & Akamatsu, T. (1980), Effects of the non-equilibrium condensation of vapour on the pressure wave produced by the collapse of a bubble in a liquid, *J. Fluid Mech.* **97**, 481–512.

Fyrillas, M. M. & Szeri, A. J. (1994), Dissolution or growth of soluble spherical oscillating bubbles, *J. Fluid Mech.* **277**, 381–407.

Hairer, E. & Wanner, G. (1996), *Solving Ordinary Differential Equations II*, rev edn, Springer.

Hao, Y. & Prosperetti, A. (1999*a*), The dynamics of vapor bubbles in acoustic pressure fields, *Phys. Fluids* **11**(8), 2008–2019.

Hao, Y. & Prosperetti, A. (1999*b*), The effect of viscosity on the spherical stability of oscillating gas bubbles, *Phys. Fluids* **11**(6), 1309–1317.

Hickling, R. (1963), Effects of thermal conduction in sonoluminescence, *J. Acoust. Soc. Am.* **35**(7), 967–974.

Ichihara, M., Kawashima, H. & Kameda, M. (2000), Dynamics of a spherical gas/vapor bubble, *Proceedings of the Third Annual Meeting of the Institute for Multifluid Science and Technology (IMuST)* .

Ishii, R., Umeda, Y., Murata, S. & Shishido, N. (1993), Bubbly flows through a converging-diverging nozzle, *Phys. Fluids A* **5**(7), 1630–1643.

Kamath, V. & Prosperetti, A. (1989), Numerical integration methods in gas-bubble dynamics, *J. Acoust. Soc. Am* **85**(4), 1538–1548.

Kameda, M. & Matsumoto, Y. (1996), Shock waves in a liquid containing small gas bubbles, *Phys. Fluids* **8**(2), 322–355.

Kameda, M., Shimaura, N., Higashino, F. & Matsumoto, Y. (1998), Shock waves in a uniform bubbly flow, *Phys. Fluids* **10**(10), 2661–2668.

Kubota, A., Kato, H. & Yamaguchi, H. (1992), A new modelling of cavitating flows: a numerical study of unsteady cavitation on a hydrofoil section, *J. Fluid Mech.* **240**, 59–96.

Lauterborn, W. (1976), Numerical investigation of nonlinear oscillations of gas bubbles in liquids, *J. Acoust. Soc. Am.* **59**(2), 283–293.

Lide, D. R., ed. (2001-2002*a*), *CRC Handbook of Chemistry and Physics*, 82 edn, CRC Press, chapter 6.

Lide, D. R., ed. (2001-2002*b*), *CRC Handbook of Chemistry and Physics*, 82 edn, CRC Press, chapter 8.

Lin, H., Storey, B. D. & Szeri, A. J. (2002), Inertially driven inhomogeneities in violently collapsing bubble: the validity of the Rayleigh-Plesset equation, *J. Fluid Mech.* **452**, 145–162.

Loève, M. (1978), *Probability Theory II*, No. 46 in Graduate Texts in Mathematics. Springer-Verlag, fourth edn.

Lofstedt, R., Weninger, K., Putterman, S. & Barber, B. B. (1995), Sonoluminescing bubbles and mass diffusion, *Phys. Rev. E* **51**(5), 4400–4410.

Lumley, J. L. (1970), *Stochastic Tools in Turbulence*, Academic Press.

Matsumoto, Y. & Kameda, M. (1996), Propagation of shock waves in dilute bubbly liquids, *JSME International Journal Series B-Fluids and Thermal Engineering* **39**(2), 264–272.

Matsumoto, Y. & Takemura, F. (1994), Influence of internal phenomena on gas bubble motion, *JSME International Journal Series B-Fluids and Thermal Engineering* **37**(2), 288–296.

Matula, T. J., Hilmo, P. R., Storey, B. D. & Szeri, A. J. (2002), Radial response of individual bubbles subjected to shock wave lithotripsy pulses *in vitro*, *Phys. Fluids* **14**(3), 913–921.

Mohseni, K. & Colonius, T. (2000), Numerical treatment of polar coordinate singularities, *J. Comp. Phys.* **157**, 787–795.

Nigmatulin, R. I., Khabeev, N. S. & Nagiev, F. B. (1981), Dynamics, heat and mass transfer of vapour-gas bubbles in a liquid, *Int. J. Heat Mass Transfer* **24**(6), 1033–1044.

Plesset, M. S. & Prosperetti, A. (1977), Bubble dynamics and cavitation, *Ann. Rev. Fluid Mech.* **9**, 145–185.

Plesset, M. S. & Zwick, S. A. (1952), A nonsteady heat diffusion problem with spherical symmetry, *J. Appl. Physics* **23**(1), 95–98.

Press, W. H., Teukolsky, S. A., Vettering, W. T. & Flannery, B. P. (1994), *Numerical Recipes in FORTRAN: the art of scientific computing*, 2nd edn, Cambridge University Press.

Preston, A. T., Colonius, T. & Brennen, C. E. (2001), Toward efficient computation of heat and mass transfer effects in the continuum model for bubbly cavitating flows, *Presented at CAV2001:Fourth International Symposium on cavitation* .

Preston, A. T., Colonius, T. & Brennen, C. E. (2002), A numerical investigation of unsteady bubbly cavitating nozzle flows, *Phys. Fluids* **14**(1), 300–311.

Prosperetti, A. (1974), Nonlinear oscillations of gas bubbles in liquids: steady-state solutions, *J. Acoust. Am.* **56**(3), 878–885.

Prosperetti, A. (1991), The thermal behaviour of oscillating gas bubbles, *J. Fluid Mech.* **222**, 587–616.

Prosperetti, A., Crum, L. A. & Commander, K. W. (1988), Nonlinear bubble dynamics, *J. Acoust. Soc. Am.* **83**(2), 502–514.

Prosperetti, A. & Lezzi, A. (1986), Bubble dynamics in a compressible liquid. Part1. First-order theory, *J. Fluid Mech.* **168**, 457–478.

Rowley, C. W. (2002), Modeling, Simulation, and Control of Cavity Flow Oscillations, PhD thesis, California Institute of Technology.

Sandhu, N. & Jameson, G. J. (1979), An experimental study of choked foam flows in a convergent-divergent nozzle, *Int. J. Multiphase Flow* **5**, 39–58.

Sirovich, L. (1987), Turbulence and the dynamics of coherent structures, parts I-III, *Q. Appl. Math* **XLV**(3), 561–590.

Storey, B. D., Lin, H. & Szeri, A. J. (2001), Physically realistic models of catastrophic bubble collapses, *Presented at CAV2001:Fourth International Symposium on cavitation* .

Storey, B. D. & Szeri, A. J. (1999), Mixture segregation within sonoluminescence bubbles, *J. Fluid Mech.* **396**, 203–221.

Storey, B. D. & Szeri, A. J. (2000), Water vapour, sonoluminescence and sonochemistry, *Proc. R. Soc. Lond. A* **456**, 1685–1709.

Storey, B. D. & Szeri, A. J. (2001), A reduced model of cavitation physics for use in sonochemistry, *Proc. R. Soc. Lond. A* **457**, 1685–1700.

Takemura, F. & Matsumoto, Y. (1994), Influence of internal phenomena on gas bubble motion, *JSME International Journal Series B-Fluids and Thermal Engineering* **37**(4), 736–745.

Tangren, R. F., Dodge, C. H. & Seifert, H. (1949), Compressibility effects in two-phase flow, *J. Appl. Phys.* **20**(7), 637–645.

Tanguay, M. (2003), Computation of Bubbly Cavitating Flow in Shock Wave Lithotripsy, PhD thesis, California Institute of Technology.

Toegel, R., Gompf, B., Pecha, R. & Lohse, D. (2000), Does water vapor prevent upscaling sonoluminescence?, *Phys. Rev. Lett.* **85**(15), 3165–3168.

van Wijngaarden, L. (1968), On the equations of motion for mixtures of liquid and gas bubles, *J. Fluid Mech.* **33**, 465–474.

van Wijngaarden, L. (1972), One-dimensional flow of liquids containing small gas bubbles, *Ann. Rev. Fluid Mech.* **4**, 369–396.

Vuong, V. Q., Fyrillas, M. M. & Szeri, A. J. (1998), The influence of liquid temperature on the sonoluminescence hot spot, *J. Acoust. Soc. Am.* **104**(4), 2073–2076.

Vuong, V. Q. & Szeri, A. J. (1996), Sonoluminescence and diffusive transport, *Phys. Fluids* **8**(9), 2354–2364.

Wang, Y. & Brennen, C. (1999), Numerical computation of shock waves in a spherical cloud of cavitation bubbles, *Journal of Fluids Engineering-Transactions of the ASME* **121**(4), 872–880.

Wang, Y.-C. (1999), Stability analysis of one-dimensional steady cavitating nozzle flows with bubble size distribution, *ASME/JSME FED Summer Meeting* .

Wang, Y.-C. & Brennen, C. (1998), One-dimensional bubbly cavitating flows through a converging-diverging nozzle, *Journal of Fluids Engineering-Transactions of the ASME* **120**(1), 166–170.

Wang, Y.-C. & Chen, E. (2002), Effects of phase relative motion on critical bubbly flows through a converging-diverging nozzle, *Phys. Fluids* **14**(9), 3215–3223.

Watanabe, M. & Prosperetti, A. (1994), Shock waves in dilute bubbly liquids, *J. Fluid Mech.* **274**, 349–381.

Zhang, Y. (1996), Dynamics of CO2-driven lake eruptions, *Nature* **379**, 57–59.

Zhang, Y., Sturtevant, B. & Stolper, E. M. (1997), Dynamics of gas-driven eruptions: Experimental simulations using CO2-H2O polymer system, *J. Geophysical Research* **102**(B2), 3077–3096.